UNIVERSITY OF CALIFORNIA, MERCED

Connecting Microstructural Defects in Molybdenum Disulfide and Amorphous Silicon Systems to Macroscale Performance using Mixed Computational Methods

A dissertation submitted in partial satisfaction of the
requirements for the degree
Doctor of Philosophy

in

Physics

by

Enrique Guerrero

Committee in charge:

Professor Michael Scheibner, Chair
Professor David A. Strubbe, Advisor
Professor Christine Isborn

2022

The dissertation of Enrique Guerrero is approved, and it is acceptable in quality and form for publication on microfilm and electronically:

(Professor Christine Isborn)

(Professor David A. Strubbe, Advisor)

(Professor Michael Scheibner, Chair)

University of California, Merced

2022

DEDICATION

To my partner and our child, who filled me with determination

TABLE OF CONTENTS

LIST OF FIGURES

LIST OF TABLES

ACKNOWLEDGEMENTS

I would like to thank my advisor Prof. David A. Strubbe. We joined UC Merced at the same time and he has encouraged my growth as a physicist, scientist, and communicator. I am indebted to his diligence and am grateful for the amount of passion he shows for teaching and leading.

I thank my committee for challenging me and helping me grow year after year. Their words and advice has stayed with me throughout my graduate education. I thank you for the thoughtful feedback and for being an encouraging group of mentors.

I am grateful for the support of my fellow graduate students and post docs at the Strubbe Ab Initio Laboratory. Our team has rapidly multiplied in size, and every new addition strengthens the group and improves us all. I have learned from them and they have become my good friends who share the struggle that is graduate school.

I acknowledge all of the wonderful collaborations throughout the physics community. The Baykara and Martini groups on campus have been productive collaborations. The Hellman, Zimanyi, and Yacamán groups have provided new ideas and thoughtful discussions to further my research.

I would like to acknowledge other faculty mentors that helped me reach the heights of today, even if they mentored me long ago: Professors Jay Sharping and Carrie Menke at UC Merced, Professors Ryan Campbell, CD Hoyle, and Monty Mola at Humboldt State University (now Cal Poly Humboldt!), and Professor Ettore Vitali at Fresno State University.

This work received funding and computational resources from the Merced nAnomaterials Center for Energy and Sensing (MACES), a NASA-funded research and education center, under award NNX15AQ01. This work used computational resources from the Multi-Environment Computer for Exploration and Discovery (MERCED) cluster at UC Merced, funded by National Science Foundation Grant no. ACI-1429783, and the National Energy Research Scientific Computing Center (NERSC), a U.S. Department of Energy Office of Science User Facility operated under Contract No. DE-AC02-05CH11231.

CURRICULUM VITAE - ENRIQUE GUERRERO

Phone: (209) 386-2442
eguerrero23@ucmerced.edu

720 Ventura Ave
Chowchilla, CA 93610

EDUCATION

PhD University of California, Merced - Physics — Aug 2022
Committee: Drs. Michael Scheibner (chair),
David A. Strubbe (advisor), Christine Isborn

MS University of California, Merced - Physics — Dec 2019

BS Humboldt State University – Physics (Astronomy) — May 2015
Minor in Applied Mathematics

FELLOWSHIPS

Merced Nanomaterials Center for Energy and Sensing (MACES) Fellowship at UC Merced 2017-2022
NASA-funded materials research fellowship involves high school outreach, presentations, research in MoS_2 solid lubrication, and mentoring opportunities

CSU Chancellor's Doctoral Fellowship at Fresno State University 2020-2021
CSU pedagogy program with Fresno State faculty mentor, Dr. Ettore Vitali. Coordinated planning of syllabus, coursework, practice lectures, and held office hours

Computing Sciences Summer Student Program at Lawrence Berkeley NL 2018
LBNL computational research 5-wk internship with seminars and a poster session

Dan David Solar Fellowship at UC Merced 2018
UC Merced fellowship for computational photovoltaic research of amorphous silicon

Physics Graduate Student Summer Fellowship at UC Merced 2018
UC Merced fellowship for summer research (amorphous silicon photovoltaics and doped MoS_2 for solid lubrication)

TEACHING AND PEDAGOGY

Pedagogy Classes and Workshops 2016-2022

- Completed semester-long Principles of Pedagogy III (2022)
- Completed semester-long Principles of Pedagogy II (2021)
- Attended AAPT 2021 Virtual Winter Meeting (2021)
- Completed Teaching and Learning in the Sciences course (2016)

Teaching Assistant – UC Merced 2016-2018

- UC Merced undergraduate courses (~30 students): Math 12 (Calculus II) [2 sections], Phys 9 (Physics II) [2 sections], Phys 19 (Physics II for Biology students) [1 section]

RESEARCH

Research Rotation/Graduate Student Researcher 2016-2022
Advisor: David A. Strubbe
Studies of amorphous Si and MoS_2 classical and *ab initio* quantum computational methods.
Gained experience presenting, keeping consistent research schedules, using shared supercomputing resources, mentoring incoming graduate students, and publishing.

LBNL Computing Sciences Summer Student Program 2018
Advisors: Drs. Andrew Canning and David A. Strubbe
Computing research modeling excitons in alkali halides using BerkeleyGW

PUBLICATIONS

Publications (published)

E. Guerrero, R. Karkee, and D. A. Strubbe, "Phase Stability and Raman/IR Signatures of Ni-Doped MoS_2 from Density Functional Theory Studies," *J. Phys. Chem. C,* **125**, 24, 13401-13412 (2021)

R. Karkee, E. Guerrero, and D. A. Strubbe, "Enhanced interlayer interactions in Ni-doped MoS_2, and structural and electronic signatures of doping site," *Phys. Rev. Materials,* **5**, 074006 (2021)

E. Guerrero and D. A. Strubbe, "Computational generation of voids in *a*-Si and *a*-Si:H by cavitation at low density," *Phys. Rev. Material*s, **4**, 025601 (2020)

Publications (unpublished)

E. Guerrero, "Connecting Microstructural Defects in Molybdenum Disulfide and Amorphous Silicon Systems to Macroscale Performance using Mixed Computational Methods," PhD thesis, University of California, Merced (2022)

O. Acikgoz, E. Guerrero, A. Yanilmaz, O. E. Dagdeviren, C. Çelebi, D. A. Strubbe, and M. Z. Baykara, "Inverse Layer Dependence of Friction on Chemically Doped MoS_2," arXiv: 2007.05805 (2022)

E. Guerrero and D. A. Strubbe, "Structure, Thermodynamics, and Raman Spectroscopy of Rhenium-Doped Bulk MoS_2 from First Principles," arXiv:2202.12889 (2022)

K. Mohammadtabar, E. Guerrero, Y. K. Shin, A. C. T. van Duin, D. A. Strubbe, and A. Martini, "Development and validation of ReaxFF reactive force field for Ni-Doped MoS_2" in preparation

E. Guerrero and D. A. Strubbe, "Atomistic Mechanisms of Sliding in Few-layer and Bulk Doped MoS_2," in preparation

FIRST-AUTHOR PRESENTATIONS (2019-2022)

APS March Meeting 2022, “Mechanisms of sliding in bulk and bilayer transition-metal-doped MoS_2”

APS March Meeting 2021, “Phase stability and Raman/IR signatures of Bulk Ni-doped MoS_2 from DFT”

Electronic Structure Workshop 2021, “Computational generation of voids in *a*-Si and *a*-Si:H by cavitation at low density”

APS March Meeting 2020, “Computational generation of voids in *a*-Si and *a*-Si:H by cavitation at low density”

SACNAS 2020 STEM Diversity Conference, “Computational Study of the 2D Material MoS_2 for Application in Space Lubrication”

APS March Meeting 2019, “DFT Study of Ni-doped MoS_2 as a Solid lubricant for Space Applications”

SERVICE

Peer-Reviewed Article for *Tribology Letters* (2022)

Developer on a nanoHUB Tool to Aid in Teaching Materials Physics (2021-2022)
MIT Atomic-Scale Modeling Toolkit (https://nanohub.org/tools/ucb_compnano)

Graduate Student Mentor (MACES) (2017-2022)
Mentored 1 graduate student and 3 undergraduate students throughout MACES

Graduate Student Peer Mentor (3 students) (GRAD-EXCEL) (2019-2020)

High School outreach through MACES (2018-2019)
MACES fellows co-lead physics experiments during local high school classes

UC Merced Recruiting via Tabling at APS March Meeting (2018-2019)

Invited Lecture and UC Merced Recruiting at Humboldt State University (2018)

High School Tutor for Jakara Movement at Paaras Youth Center (2016)
Multi-subject tutor for primarily Punjabi Sikh high school students, developed curriculum for SAT summer course

OTHER SKILLS

Fluent in English and Spanish

Used Canvas in pedagogy classes and Teaching Assistantship

Strong coding and programming background:
Proficient User: Python, Mathematica, Bash, C++
Independent User: Excel, JavaScript, Fortran, R

ABSTRACT OF THE DISSERTATION

Connecting Microstructural Defects in Molybdenum Disulfide and Amorphous Silicon Systems to Macroscale Performance using Mixed Computational Methods

by

Enrique Guerrero
Doctor of Philosophy in Physics

University of California Merced, 2022

Professor Michael Scheibner, Chair

Microstructure defects are the source of many interesting physical phenomena in materials. The influence of microscopic imperfections are visible among a background of a crystalline material and can noticeably change macroscopic material properties. *Ab initio* computations are a wide range of computational methods used to study materials at such microscopic levels. Classical and quantum-level computations are often viewed as competing methods, but we instead take a complementary approach. We combine strengths of both methods to study two classes of materials—silicon and the two-dimensional (2D) transition metal dichalcogenide (TMD) molybdenum disulfide (MoS_2). In MoS_2, we interrogate the effects of the presence of dopants. Conversely in Si, we take amorphization as a disruption to the base crystalline structure. In both, we are interested in how these changes to microstructure affect energetic efficiencies. In *a*-Si, the photovoltaic efficiency is hampered by the presence of dangling bonds, while in MoS_2, mechanical efficiencies of lubrication are enhanced when doped.

Both systems pose their unique challenges and deviations from standard workflows. We will review the overarching strategies used to study them in Ch. 2. Throughout our studies, we have developed several techniques to overcome specific challenges which are detailed in their respective sections. With *a*-Si, a clas-

sical potential Monte Carlo code is used to generate realistic, non-biased, fully amorphous coordinates faster than what could be achieved by currently available quantum-mechanical methods. Then, density functional theory is used to relax the structures. With MoS_2, higher-accuracy DFT energy computations are used to parametrize a classical force-field for the computation of larger systems which would otherwise be difficult with DFT alone.

We cover a wide range of analyses between both materials. We have developed methodologies for analyzing the amorphous and 2D material systems using classical methods and density functional theory. We have computed a range of material properties for MoS_2 and amorphous Si and hydrogenated a-Si:H. With Si, we modified the Wooten-Winer-Weaire algorithm to produce amorphous networks with included voids by application of initial strain. The size of the voids is somewhat controlled by the strain value. These voids emerge naturally as a part of the amorphization process.

We find that the amorphous networks generated by simple Keating springs when applied in the WWW method is retained when relaxed by DFT. Structure-scale approximations of the Keating potential yields the result that $\Delta\theta$ explains a large portion of the structure's energy, and this holds even in density functional theory.

With 2D materials, we outline a specific multi-step method to quantify the sliding of defected materials in Ch. 6. Successive increases in the degrees of freedom while sliding allow us to access different components of sliding—namely the potential barrier differences, low-energy sliding pathways, and slip planes. The sliding potential in MoS_2, even while intercalated, is composed of pairwise interactions of the MoS_2 interfaces. This means that computing arbitrarily sized systems can be theoretically computed by only considering interactions of their interfaces.

We find tetrahedrally intercalated Ni-doped MoS_2 to be stable and thus more important than is considered in the literature. When intercalated, we find Ni can bind layers together, explaining the material's increased resistance to wear, or material loss during sliding.

Re-doped MoS_2 has shown an increase in friction with an increasing layer count as measured with atomic force microscopy. This is counter to typical 2D materials. We find that intercalated Re can explain this relationship as an alteration to out-of-plane stiffness. For this material, in computing the vibrational spectroscopy we overcame a difficulty in computing its Raman spectra. It has a metallic character, thereby limiting our Raman intensity computation due to an infinite dielectric constant. We developed a method to circumvent this computation and approximate the spectra by substitution of the atomic Raman tensor.

Chapter 1

Introduction

Since the invention of computers, they have been a staple tool for studying realistic physical systems [114]. A core negotiation in computational physics is the balance between accuracy and computing time. As the density of transistors has increased exponentially over time, accurate computation of high resolution physical systems have become standard. In classical atomistic simulations of materials, we can use empirical information to study how large numbers of atoms affect material properties. With quantum-mechanical level simulations, we are able to take the wave-like behavior of a system's electrons into account to more accurately predict macroscopic behavior.

The classical methods we use are interatomic potentials, where a function based on the atomic coordinates and material-specific parameter constants (such as interatomic force constants) are used to compute material properties. The constants are typically decided empirically with good fits to experimental data or higher-level computations. Notably, we keep track of the atomic coordinates but do have no explicit treatment of the electrons. Electronic effects on the material properties are hidden in the constants we use. This is in contrast to quantum mechanical methods used in our work which are rooted in approximating applications of the Schrödinger's equation to the system's electrons.

The quantum mechanical tool we use is density functional theory (DFT), where the electronic density is computed explicitly and system properties are computed from it. In Kohn-Sham (KS-) DFT [87], the density is approximated by treating the system's many-body wavefunction as many one-electron wavefunctions. This formulation is said to be *ab initio*, "from first principles", because results are not based on *ad hoc* approximations such as atomic species-dependent force constants. There are approximations made, notably exchange-correlation potentials V_{xc} discussed in Ch. 2 [133], but the schemes used to create them are based in physical principles. This results in transferrable approximations–they apply to many atomic types under many material conditions, unlike parameters in our classical potentials. Explicit treatment of the electrons allows computation of complex phenomena inaccessible by classical methods alone, such as the electronic density of states or electron-phonon coupling.

The disparity in computational effort can be understood by the quantities the potentials are acting upon in both classical and quantum methodologies. The classical potentials we use are functions of static parameters and the atomic coordinates which can lead to $\mathcal{O}(N^2)$ scaling. KS-DFT acts on the atomic density which is constructed from KS electronic wavefunctions. To diagonalize the Hamiltonian requires $\mathcal{O}(N^3)$ scaling. In practice, the classical method can be reduced to $\mathcal{O}(N)$ by limiting the spacial extent of interatomic potentials and the disparity widens.

Rather than treat these methods as competing against one another, we take an approach that uses the advantages of both to study material properties. In the work presented, we show that this combined approach aids us in studying amorphous Si (a-Si) in Chs. 3-4 and molybdenum disulfide ($\mathrm{MoS_2}$) in Chs. 7-8.

1.1 Amorphous Silicon Systems

Crystalline silicon (c-Si) is an exemplary model semiconductor in computation. The stability of its bonds, small unit-cell size, and predictability of its band structure lead to it being a standard material to test the robustness of new computational methods. Changing the phase of the structure from crystalline to amorphous silicon (a-Si) alters properties and makes it immediately less predictable. Despite the random nature of the material, we can study it using ensembles of

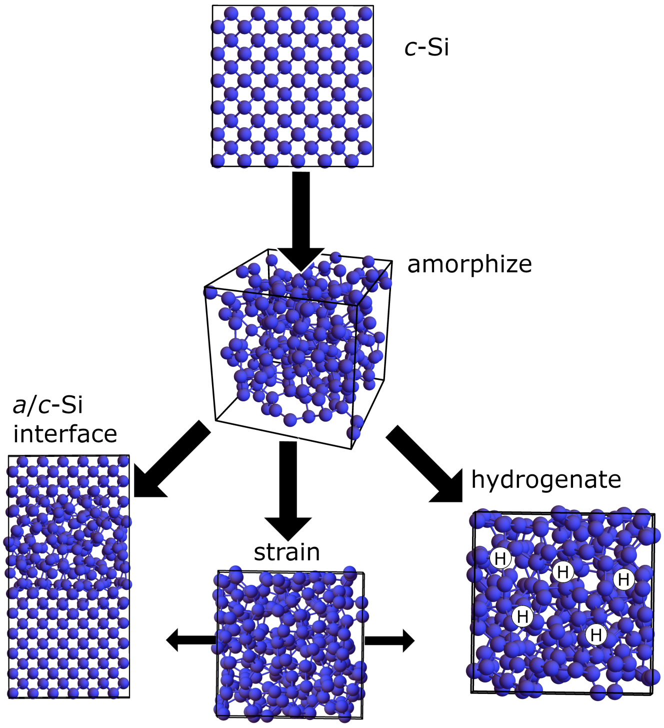

Figure 1.1: Graphical summary of Si structures presented in this thesis.

computations. *a*-Si's application as one of the earliest photovoltaic technologies has been thoroughly explored for half a century [163], and its photovoltaic efficiency has stagnated in half that time. However, interest in the material has seen a resurgence in interest in the last decade as a component of a highly efficient solar cell [21]. Other interest in the material involve its ultra-reflective properties [164]. Both these properties can be studied using our computations.

As a photovoltaic, a main challenge with amorphous silicon is the Staebler-Wronski Effect (SWE), light-induced degradation [163]. As light enters the material, its solar efficiency drops permanently over longer time scales. Degradation has thus far been attributed to dangling bonds, or unpaired electrons, and the presence of microvoids [40] discussed in Ch. 2. This concept and the heterojunction with intrinsic thin-layer (HIT) solar cell in general [21, 78, 69] have guided our computations revolving around amorphous Si.

a-Si poses a few challenges when modeling accurately, namely accurate atomic coordinates and dangling bonds. While atoms are randomly dispersed throughout the material, they are not uniformly random because their positions are intercorrelated. They show strong short-range order (SRO) when averaged, despite a lack of long-range order (LRO). Our method of generating atomic coordinates is based on the well-tested [194, 75, 76, 77] Wooten-Winer-Weaire [207] classical Monte Carlo method as implemented in the code CHASSM, the Computationally Hydrogenated Amorphous Semiconductor Structure Maker [169]. We can generate perfect amorphous structures free of defects.

In reality, amorphous Si is difficult to fabricate without the presence of dangling bonds. In semiconducting applications, the unpaired electron acts as a trap for holes which encourage premature recombination [76]. To combat this, a-Si is typically treated under H-rich conditions. This allows H to diffuse into the material and attach itself to these dangling bonds, thereby passivating them. CHASSM allows us to simulate hydrogenation, as detailed in Ch. 2. In the literature, typically only either hydrogenated or non-hydrogenated a-Si is studied—we are well equipped to study both. Throughout this work, we have developed new methodology to control the amount of dangling bonds created in a structure in an unbiased manner, more closely related to realistic material formation. We have accomplished this by developing a method to generate voids on an amorphous structure by straining the initial generating structure. This is counter to the typical process of atomic removal and is described in Ch. 3. The method used here is applicable to any material that can use the WWW method, i.e. continuous random networks.

CHASSM is a useful tool to generate a-Si, but its accuracy is only as accurate as the relatively basic Keating potential [82] which we have used. The simplicity of the potential leaves a desirably small number of empirical variables, but lacks sophistication to study more complex material properties, especially those involving dynamic electronic behavior. For this reason, we further process structures generated by the classical code CHASSM with DFT using Quantum ESPRESSO [50]. The potentials used in ESPRESSO yield more accurate potential energy surfaces. We explore the result of processing CHASSM structures of variable densities through DFT in Ch. 4. We take a systematic approach to studying strain-energy relationships and unique amorphous parameters to the system's energy. These

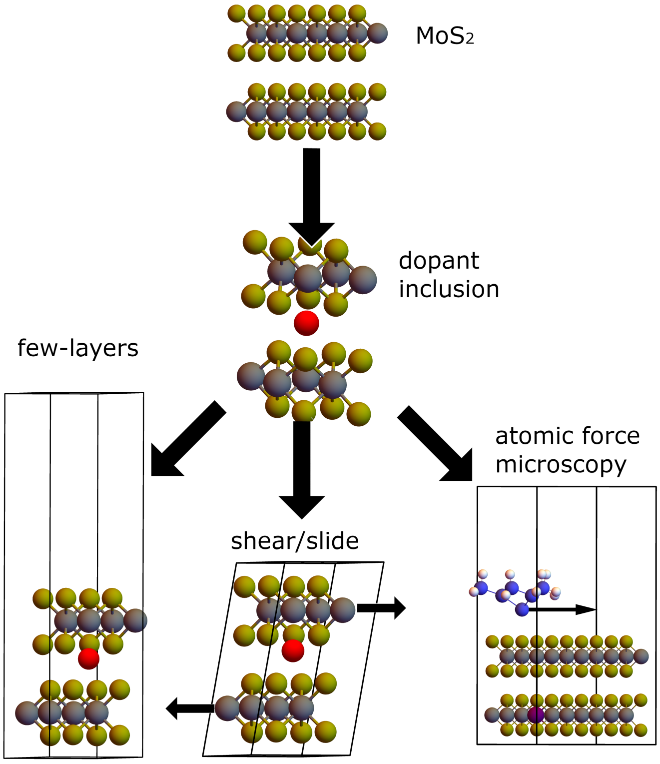

Figure 1.2: A sample of the MoS_2-type structures presented in this thesis. Among all computations, doped structures are compared against pristine simulations.

findings may quantitatively express the a configurational energy gap [37] between amorphous and crystalline MoS_2 which has thus far only been qualitatively described.

1.2 MoS_2 Systems

Like amorphous silicon, MoS_2 has a unique structure when compared to typical solid. It is a two-dimensional (2D) lamellar material where van der Waals (vdW) forces dominate the interlayer interactions. Unlike graphite or graphene systems, MoS_2 has strong covalent intralayer bonds that extend out of plane in the Mo-S bonds. This relatively uncommon shape and its status as a semiconductor lead to a host of applications ranging from electronic [11], catalytic [111, 196], photovoltaic [118, 183, 10], and tribological [191] properties. Doping, the intentional introduction of atomic defects, is a tool used to control the materials' properties.

Throughout our studies, we have subjected computational samples of MoS_2 to a host of conditions: Ni-doping [58], Re-doping [57], C-doping, atomic force microscopy [1], interlayer sliding [56], strain [116], layer count variation, and various micro-studies to reach our larger conclusions. Our searches are originally motivated by studying the frictional properties of doped MoS_2, however we developed methodology that is generic and applicable in other contexts.

Re and Ni are two transition metal dopants which are important to MoS_2, especially in tribological applications. For Ni, it has been found to reduce the frictional forces and increase its resistance to wear, or layer dissociation [170]. To study this process, we collaborated with the Martini group and relied on their experience with classical potentials to parametrize a reactive force field [127, 186] using DFT computations. This process is described in Ch. 7. This classical potential allows them to study larger systems in a dynamic capacity. Our static computations, however, are useful in learning about the structural stability and allow us to compute accurately the experimentally comparable vibrational spectra.

We found thermodynamically stable configurations of Ni and Re as they dope MoS_2 for variable concentrations. Since Ni and Re are transition metals like Mo, the prevailing hypothesis for the dopants' location is substitution of Mo. In both, we found that intercalation, where the dopant is between MoS_2 layers, is a valid and overlooked at least meta-stable dopant location. Having the dopant in this location significantly alters elastic parameters we computed. Vibrational spectra and electronic densities are also altered by dopant inclusion.

We computed sliding structures of Ni-doped MoS_2 and found explicit evidence that the sliding potential can be expressed as pairwise interactions between interlayer interfaces. This intuitive result leads to useful computational and explanatory physical results. It provides credence in reducing the sliding potential computation of an N-layered system as $N-1$ bilayers, which will always be cheaper. The fact that the sliding potential does not extend into the MoS_2, even when strong interlayer bonds exist, means that t-intercalated MoS_2 is compatible with lower friction, despite it binding the layers together.

Re is a naturally occurring dopant that has been found to significantly alter the sliding behavior of MoS_2 as it pertains to layer dependence. In 2D materials, more layers usually means less friction, but this trend is reversed for Re doping. This is discussed in chapters 8 and 9.

Like Ni, we found thermodynamically stable structures and the vibrational spectral fingerprints. In finding the spectra of this material, we developed a method of approximating the Raman spectra of a previous incalculable structure by standard DFPT methods. Under the computational scheme, the structure is metallic and thus its polarizability and Raman intensities were infinite and incalculable. In practice, however, a Raman intensity is measurable. This points to a disconnect between physical reality and computational approximations. We overcame this by inserting a best approximate guess of the polarizability based on the undoped MoS_2. In effect, we are able to capture changes in the vibrational spectra due to the geometric distortions introduced by the dopant.

We also modeled an atomic force microscope and developed an analysis route for N-layered doped MoS_2, where the dopants location is somewhat obscured. This model connects to the macroscopic experiments by the Baykara group and are used to reason that changes in the elastic parameters due to intercalation causes the inverse layer dependence observed in Re-doped MoS_2 [1].

Chapter 2

Methodology

2.1 Strategy to Model Amorphous Si Systems

Given the inherent statistical nature of amorphous systems, an approach to adequately capture the behavior of a macroscopic sample of *a*-Si is to compute an ensemble of amorphous structures [168, 77]. These individual structures behave as local regions of a macroscopic samples and by taking statistics on the ensemble we learn about the *a*-Si at large. To quantify the randomness of samples, $\Delta\theta$, the standard deviation of bond angles, can be taken as a order parameter. Other statistical parameters of interest are the structures' energies, mean bond angles, mean bond lengths, and bond length deviations. Of these, as we will find in Ch. 4, $\Delta\theta$ is the most energetically important parameter.

To balance accuracy and speed for structure generation, we take a multi-step approach to modeling *a*-Si systems. First, we use the classical Monte Carlo WWW method as implemented in the code CHASSM (Computationally Hydrogenated Amorphous Semiconductor Structure Maker) [169]. This method is fast and generates reasonable atomic coordinates which can then be relaxed with DFT. Within CHASSM, we use the Keating potential described in the following section. We then include quantum electronic interactions using density functional theory, described in the further section.

2.1.1 WWW Method as implemented in CHASSM

The WWW method [207], developed by Wooten, Winer, and Weaire in 1985, is designed to generate ensembles of realistic a-Si atomic coordinates when paired with the classical Keating potential [82]. The leading alternative method in a-Si generation is "melt-and-quench", where Si atoms undergo high temperature (T) molecular dynamics and is slowly annealed, but this method can be expensive and can lead to uncontrolled amounts of bonding defects [5]. Older coordinate generation methods involved using hand-crafted cluster models which tend to suffer effects of the free surface. The WWW method is specialized to continuous random networks and accelerates the amorphization process. The boundaries are periodic, so there are no undue surface effects, and image effects can be avoided by increasing the cell size to include at least about 60 atoms. The WWW method employs the following Monte Carlo steps:

0. Start with crystal with known network and calculate the energy.
1. Consider a "move": a bond switch of nearby bonds that changes the network.
2. Compare the change in energy to the Boltzmann factor and accept if $X \leq e^{-\frac{E_2-E_1}{k_B T}}$.
3. Return to step 1.

$X \in (0, 1)$ is a randomly generated real number, E_1 and E_2 are the energies of system before and after the move, k_B is the Boltzmann constant, and T is an imposed temperature. The Boltzmann factor, $e^{-\frac{E_2-E_1}{k_B T}}$, is always greater than X when $E_2 < E_1$, so moves that lower the energy are always accepted.

In CHASSM, this process is repeated for about 10^6 moves per atom at varying temperatures. We use a temperature profile consisting of two main phases: "randomize" and "anneal" phases. The first 10^3 moves per atom are at a high T to force the system away from the deep crystal well in phase space and the energy of the system is dramatically increased. In the annealing phase, we make moves while slowly lowering T—this assures that our system is in a local minimum of the potential energy landscape. The last "quench" step is a series of $T = 0$ K that certify the structure is at a local minimum. After quenching, amorphous structures are always higher in energy than crystalline structures by about 0.07 eV/atom, *i.e.* there is a discontinuous increase in energy between amorphous and crystalline phases, as is discussed in Ch. 4.

The WWW prescription requires a potential energy description that considers bonded atoms only. CHASSM implements the Keating potential as the Boltzmann factor energy. The Keating potential, U_K, consists of only two- and three-body terms describing springs along bond lengths and bond angles and was originally created for *c*-Si but has since been applied to *a*-Si. It relies on a predetermined bond table, not a set of distance-based nearest neighbors, to decide which atoms interact. It is described as follows:

$$U_K = \frac{3\alpha}{16\delta^2}\sum_{i}^{N_{at}}\sum_{j=1}^{N_{b,i}}(|\vec{r}_{ij}|^2 - \delta^2)^2 + \frac{3\beta}{8\delta^2}\sum_{i}^{N_{at}}\sum_{j=1}^{N_{b,i}}\sum_{k>j}^{N_{b,i}}(\vec{r}_{ij}\cdot\vec{r}_{ik} - \delta^2 cos(\theta_t))^2 \qquad (2.1)$$

α and β are force constants parametrized to match experimental amorphous data—we use 2.965 and 0.845 eV/Å^2 respectively [5]. δ is the equilibrium bond length of *c*-Si and is set to 2.35 Å. N_{at} is the number of atoms per cell. $N_{b,i}$ is the number of atoms bonded to i (typically four in *a*-Si, though this can be changed to study *a*-Si:H). $\vec{r}_{ij}$ is a displacement vector from atom i to j and $\theta_t = 109.5°$ is the tetrahedral bond angle such that its cosine is $-\frac{1}{3}$. Qualitatively, this potential energy increases as local bonding order less resembles the ideal tetrahedral *c*-Si structure. Keating interactions only exist between predetermined bonded atoms.

CHASSM introduces a few critical alterations to the WWW algorithm. As the name implies, CHASSM computes hydrogenated *a*-Si:H. The *c*-Si in step (0.) is treated as hydrogenated by removing pairs of Si-Si bonds, meaning some atoms have only 3 bonds, thus simulating an Si-H bond [194]. The system evolves normally, but H atoms are added to atoms which initially only had 3 bonds. This method avoids an *a priori* idea where H atoms should go, as involved in schemes of identifying and passivating dangling bonds [16]. Structures generated by this method as implemented in CHASSM have been used to study barriers to bond-switching in the SWE [194], strain-induced shifts in Raman peaks [168], optical

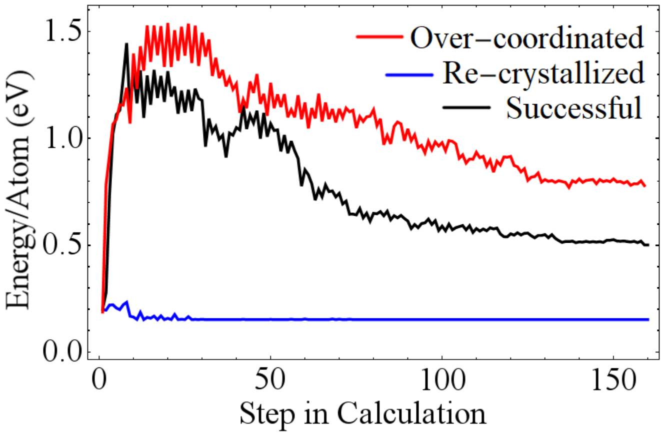

Figure 2.1: Keating energy throughout a calculation. The first 8-10 steps are high T randomization. If the structure fails to obtain enough energy to escape the c-Si barrier, it re-crystallizes (blue). If the structure randomizes at too high a T, it does not relax to a reasonable energy (red) or bonding network. A run producing a desired realistic amorphous structure has an intermediate behavior (black).

absorption [142], and nanocrystalline sites in a-Si, validated with a variety of properties [122].

Throughout my explorations, we developed a further critical alteration to step (0.)—we strain the initial structure, then evolve the system. This simple change leads to emergent differences in the final structures. As we explore in Ch. 3, we show that this method of controlling the density leads to changes to porosity and bond angle deviation $\Delta\theta$, an order parameter or measure of randomness.

Finally, it is also possible to generate c-Si regions, as would be done to generate the a-Si/c-Si interface, by freezing atoms in place and disallowing their participation in the WWW process.

CHASSM generates 4-bonded networks of a-Si that are able to explore reasonable regions of the potential energy surface. The only empirical information present in the potential are spring constants for bond angles and bond lengths. These can be replaced with fully *ab initio* methods by further relaxing the structure with DFT.

2.2 Density Functional Theory as Implemented in Quantum ESPRESSO

We use DFT in both the Si systems and the $\mathrm{MoS_2}$ systems. For our purposes, it balances computational complexity with the accuracy required to model the electronic contributions.

The basics of plane-wave Density functional theory (DFT) are outlined here based on works by Cohen and Louie [31] and Payne *et al.* [133]. DFT is an *ab initio* quantum mechanical method used to provide an approximate solution to the full Schrödinger equation:

$$\mathcal{H}|\Psi\rangle = (T+V)|\Psi\rangle = E|\Psi\rangle \tag{2.2}$$

where $\Psi = \Psi(\{\mathbf{r}\},\{\mathbf{R}\})$ is the many-body wavefunction which is a function of sets of electronic $\{\mathbf{r}\}$ and atomic coordinates $\{\mathbf{R}\}$. T and V are kinetic and potential terms of $\mathcal{H}$, the Hamiltonian, and solve for E, the energy. Unlike the classical EQ 2.1, DFT does not require empirical inputs such as α and β. In the Keating picture, only springs exist and there is no concept of electrons—thus it cannot accurately model the nature of dangling bonds. DFT *can* correctly place electrons and their resultant effects on nearby atomic structure; but to do so we need a way to solve the Schrödinger equation, which in principle requires a 10^{23}-dimensional wavefunction to describe all of the atoms in a macroscopic solid.

The first step in approximating EQ 2.2 is the Born-Oppenheimer approximation. Under this approximation, $\Psi(\{\mathbf{r}\},\{\mathbf{R}\}) \approx \psi(\{\mathbf{r}\},\mathbf{R})P(\{\mathbf{R}\})$, i.e. the electronic ($\psi$) and atomic ($P$) contributions to the total wavefunction are separable. The basis for this approximation is that the large difference in mass between atomic nuclei and electrons means they react to each other at different time scales. The electronic wave function responds as if the atoms are frozen in space and the atoms respond as if electrons have had enough time to settle to their ground state.

DFT is rooted in the Hohenberg-Kohn theorem and we use the Kohn-Sham (KS) [87] formulation. Hohenberg and Kohn find that V_{ext}, the external potential on the electrons due to the atoms, has a one-to-one relationship with the electronic density, $\rho(\mathbf{r})$. This means that rather than directly solve the $3N_e$-dimensional (where N_e is the number of electrons), many-body wavefunction Ψ, we need only a way to solve for the 3-dimensional electronic density $\rho(\mathbf{r})$.

Kohn and Sham do just that by creating an auxiliary system of wavefunctions. Rather than attempting to solve the many-body wavefunction, the KS system solves for a system of N_e non-interacting electrons which gives the same $\rho(\mathbf{r})$. Regardless of how we found ρ, if ρ corresponds to V_{ext} then our job is complete. The Kohn-Sham equations can be expressed as:

$$(T_S + V_{ion} + V_H + V_{xc})|\psi_n\rangle = \epsilon_n|\psi_n\rangle \tag{2.3}$$

T_S is now the non-interacting kinetic energy. $\{\psi_n(\mathbf{r})\}$ are the set of auxiliary wavefunctions such that $\rho(\mathbf{r}) = \sum_i^{N_e} |\psi_n(\mathbf{r})|^2$. V_H and V_{xc} are themselves a function of $\rho(\mathbf{r})$, and since $\rho(\mathbf{r})$ is a function of $\{\psi_n(\mathbf{r})\}$, EQ 2.3 must be solved self-consistently.

The potential terms in EQ 2.3 are split into three terms. V_{ion} is the external potential from the atomic nuclei. V_H, the Hartree potential, describes how the electrons react to the electrostatic field due to all other electrons. Finally, the V_{xc} term contains information about exchange and interaction; this contains the effects of Pauli exclusion. V_{ion} and V_H have exact forms. V_{xc} does not and is approximated by sophisticated means [133].

The total energy, E, is a function of the eigenvalues $\{\epsilon_n\}$ and ρ. We can use E to construct potential energy surfaces. We can solve for when local minima of E with respect to $\{\mathbf{R}\}$. Minimal energy coordinates correspond to a stable arrangement of atoms.

Quantum ESPRESSO [50] is a DFT package that uses a reciprocal-space plane-wave basis set such that any periodic wave function can be written as:

$$\psi_n(\mathbf{r}) = \sum_{\mathbf{G}} c_n e^{i(\mathbf{k}+\mathbf{G})\cdot\mathbf{r}} \tag{2.4}$$

where $c_{n,\mathbf{k}+\mathbf{G}}$ are wavefunction coefficients and $\mathbf{G}$ vectors are reciprocal lattice vectors. $\mathbf{k}$ is a point in reciprocal space within the Brillouin zone (BZ). The BZ is the finite region in reciprocal space that contains all of the unique $\mathbf{k}$-vectors needed to describe the infinite periodic crystal. Calculations within the plane-wave DFT architecture often involve integrals of the form $\int_{BZ} f(\mathbf{k})d\mathbf{k}$. To solve

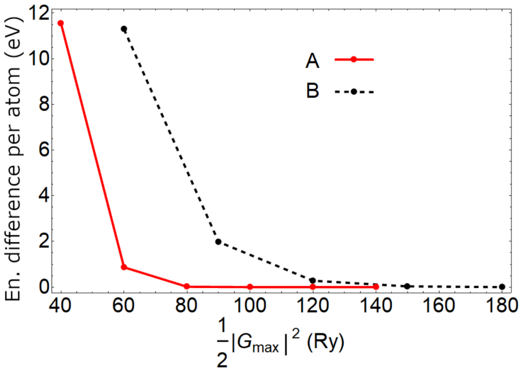

Figure 2.2: Comparison of energy convergence of number of **G** vectors between pseudopotentials A and B. Energies are with respect to the largest calculation (140 Ry for A, 180 Ry for B). In this case, A converges faster and would calculate faster for a given accuracy. Energies below 0.1 eV/atom are considered acceptable amounts of error.

these numerically, we need to sample k-points, but we must do so carefully as computation time and accuracy is tied to the number of k-points. Since the number of **G** vectors is infinite, we must also truncate the number of **G** vectors used in our calculations. These values are decided by convergence tests such as in Fig. 2.2. In this figure, ideal values for the G vector cutoffs should be between 80 and 100 Ry for the red curve as these values show little energy difference when compared to the energy at a 140 Ry cutoff.

Usually, only the valence electrons participate in bonding and low-energy optical phenomena. To limit the amount of electrons in our calculations, we can eliminate the need of calculating core electrons via pseudopotentials. Since the core electrons screen the Coulomb interaction between valence electrons and the atom, we can replace the entire atomic core with an approximate potential. These pseudopotentials are generated externally for each element type. Like **k**-points and **G** vectors, pseudopotentials come with their own set of convergence criteria that must be satisfied.

2.2.1 Density functional perturbation theory

The main role of density functional perturbation theory (DFPT) is to solve for phonon eigenmodes and eigenvalues. The following brief is based on a review by Baroni *et al.* [6] These modes are the vibrational states in the crystal and the eigenvalues are their frequencies. These vibrational modes are related to a range of phenomena from heat transfer to IR and Raman spectroscopy. To calculate vibrations, DFPT applies perturbation theory where E or ρ can be treated as sums of responses to a perturbing parameter λ:

$$E(\lambda) = E^{(0)} + \lambda E^{(1)} + \lambda^2 E^{(2)} + ... \tag{2.5}$$

$$E^{(n)} = \frac{1}{n!}\frac{d^n E}{d\lambda^n}|_{\lambda=0}. \tag{2.6}$$

We can apply the harmonic approximation on the total energy with perturbing displacements of atom α in direction μ, $\mathbf{u}_{\alpha\mu}$:

$$E = E^{(0)} + \frac{1}{2}\sum_{\alpha,\beta,\mu,\nu} \frac{\partial^2 E}{\partial \mathbf{u}_{\alpha\mu}\partial \mathbf{u}_{\beta\nu}} \mathbf{u}_{\alpha\mu}\mathbf{u}_{\beta\nu} \tag{2.7}$$

The linear term $E^{(1)} = 0$ because we calculate phonons at equilibrium coordinates. Terms higher than $E^{(2)}$ are ignored under this approximation.

In principle, to solve this equation we would need to calculate $(3N)^2$ derivatives, at least that many DFT self-consistent calculations of the total energy. In practice, it is more efficient to expand E in the second term of EQ 2.7 into its components. This is due to the fact that second-order derivatives of the total Hamiltonian eigenenergy can be found using only first-order derivatives of the eigenfunctions.

Terms of the dynamical matrix ($D_{\alpha\mu\beta\nu}$), which can be thought of as a mass-reduced spring constant, are proportional to $\frac{\partial^2 E}{\partial \mathbf{u}_{\alpha\mu}\partial \mathbf{u}_{\beta\nu}}$. Diagonalizing this matrix yields the eigenmodes and eigenvalues which represent phonon modes and frequencies in the structure. Raman and IR intensities are calculated in the same way, but introducing $\mathcal{E}_\sigma$, a small electric field in the σ direction, as a perturbation. IR intensity computations are proportional to $\frac{\partial^2 E}{\partial \mathbf{u}_{\alpha\mu}\partial \mathcal{E}_\sigma}$ and require little extra work to the phonon calculation. Raman mode intensities require one higher perturbation step, where elements of the Raman tensor are proportional to $\frac{\partial^3 E}{\partial \mathbf{u}_{\alpha\mu}\partial \mathcal{E}_\nu \partial \mathcal{E}_\sigma}$.

Chapter 3

a-Si and a-Si:H: Generation of Voids by Cavitation at Low Density

This chapter has been reprinted with permission from Physical Review Materials 4, 025601 (2020). Copyright 2020 American Physical Society [55]. The publication, titled "Computational generation of voids in a-Si and a-Si:H by cavitation at low density," pursues our goal is to model realistic amorphous silicon (a-Si) with a focus on generating samples with voids. This was accomplished by modifying the previously established Wooten-Winer-Weaire (WWW) [207] method slightly—we lower the initializing crystal's density and allow the Monte Carlo process to advance. The result is an ensemble of structures with the emergent appearance of voids at low densities.

3.1 Abstract

We study the microstructure of computationally generated amorphous silicon (a-Si) and hydrogenated amorphous silicon (a-Si:H) as a function of density. The details of the atomic structure in these materials underlie the causes of optoelectronic losses—specifically light-induced degradation and suppressed hole mobilities. Accurately modeling the microstructure is critical to quantifying these

effects; we focus on generating populations of *a*-Si and *a*-Si:H structures with and without voids. We use a modified WWW Monte Carlo method with the Keating potential, using a range of fixed densities rather than the usual atomic removal. We find a smooth evolution in bond lengths, bond angles, and bond angle deviations $\Delta\theta$ as the density is changed around the equilibrium value of 4.9×10^{22} atoms/cm^3 to higher and lower values. A significant change occurs at densities below 4.3×10^{22} atoms/cm^3 with an onset of void formation, which is associated with a drop in negative pressure, akin to a cavitation process in liquids. We find both small voids (radius ~ 3 Å) and larger ones (up to 7 Å), as in previous computational studies, which compare well with available experimental data. The voids have an influence on atomic structure up to 4 Å beyond the void surface, and are associated with decreasing structural order, measured by $\Delta\theta$. We also observe an increasing medium-range dihedral order with increasing density. The method used to generate structures with voids does not rely on expensive density functional theory molecular dynamics, and allows voids to form naturally by a physical process, without needing any scheme for adding or removing atoms or an *a priori* idea of void structure. This work provides a set of void structures for further studies of properties such as the Staebler-Wronski effect.

3.2 Introduction

Amorphous silicon (*a*-Si) is a cheap and flexible semiconductor used as ultra-reflective mirror coatings [164], thin-film transistors [125], and solar cells. A resurgence in interest in the material comes from the designs of heterojunction with intrinsic thin-layer (HIT) cells, a *c*-Si/*a*-Si tandem solar cell with high efficiency comparable to traditional crystalline silicon (*c*-Si) solar cells [21]. Unfortunately, fielded HIT cells suffer from twice the degradation rate of single-crystal Si cells [78, 69]. This increased rate has been attributed to the light-induced Staebler-Wronski degradation [163] of *a*-Si:H which has been attributed to changing Si-H bonds at small voids [40].

It is known that deposition conditions affect resultant density, intrinsic stress, and void content [75, 190]. The existence of microvoids has been observed using small-angle electron spectroscopy [121] and small-angle x-ray spectroscopy [109]. These methods find density-deficient regions in *a*-Si:H and attribute them to voids. Nuclear magnetic resonance [7] and infrared absorption [128, 161] techniques suggest that H like to cluster, perhaps even in the form of molecular H_2 [51]. Increasing H concentrations can increase the amount of H clustering [161] and decrease the Young's modulus [74]. H effusion has been used to indirectly measure voids, but may not distinguish between microvoids or interconnected low-density regions; instead He implantation and temperature-mediated effusion can study voids with divacancy-level resolution [12]. Experimental void research in non-hydrogenated *a*-Si is sparse, *a*-Si may in fact contain fewer voids than *a*-Si:H [202, 147]. Recent experiments involving density variation and void response in *a*-Si using electron spin resonance have undergone with the intent of shedding light on the origins of two-level systems [71, 117]. This zoo of experimental measurements yields void sizes to be anywhere from the size of divacancies, about 3 Å [12], to 40 nm [51]. Void number density ranges from $10^{18} - 10^{20}$ cm^{-3} [12, 110]. Experimental results can be contradictory: infrared measurements suggest that divacancies dominate the void content [161] while He effusion shows larger voids are more prevalent [12]. Due to the omnipresence of voids in amorphous systems, their study is crucial to understanding the macroscopic properties of *a*-Si and *a*-Si:H.

The common method for void generation in computational *a*-Si:H is atomic removal [24, 135, 124, 83, 14, 132]; *a*-Si coordinates are generated, a choice of Si atoms are removed, and dangling bonds may be passivated by H-insertion. This method has been used to model void-related specific heat dependencies [124], effects on small-angle x-ray spectroscopy [132], hydrogen evolution [24], and to compare to paracrystalline structures [14]. Si removal can generate voids of controllable shape and size, but it may leave an inherent bias: there will be 4 dangling bonds left behind by a monovacancy, 6 for a divacancy, etc. Small voids are intrinsic to *a*-Si, Pedersen *et al.* [135] have used this idea to generate realistic, low-energy *a*-Si structures by a grand-canonical Monte Carlo method in which atoms can be removed to find lowest-energy densities and bond topology. Biswas *et al.* in

2017 [16] used a metadynamics approach [15] as an alternative to atomic removal. This method finds voids as a product of biasing structures to fit bonding defect constraints. This method has been used to study microvoids of about 5 Å in large cells (7000 Si atoms), carefully constructing a description of the complex-shaped void network [13].

We take a complementary approach to these studies. We explore voids up to 7 Å at low generation density instead. Our approach of annealing at constant volume and number of atoms potentially is more closely connected to the physical processes of chemical vapor deposition growth [77], in which initially deposited Si (and H) atoms on a surface at elevated temperature undergo an annealing process to form the final structure [161]. The melt-quench approach [86] could potentially be used to prepare voids, but voids may be controlled more by bubble formation in the liquid than the properties of the solid network.

Many works choose either *a*-Si or *a*-Si:H as the material of interest, we have studied voids present in both materials due to the transferrability in our methods. Our aim is to generate structures with voids for use in studying the effects on light-induced degradation [231] and other optoelectronic properties of *a*-Si:H. We use the Wooten-Winer-Weaire [207] method to generate ensembles of *a*-Si and *a*-Si:H at 10% hydrogen content, as is commonly used for electronic devices [167]. We modify the WWW algorithm and observe the formation of voids in the equilibrium structures at a given density, rather than explicitly removing atoms. Typical *a*-Si simulations only consider experimental densities; we instead systematically vary our density and find that the stochastic evolution of our structures favors void formation at low densities. Densities as low as 3.4×10^{22} at/cm^3 are studied, we take these structures to model the behavior of low-density regions of *a*-Si while 4.8-5.0×10^{22} at/cm^3 model typical density regions. Our method is computationally simple and efficient, and it does include expensive density functional theory (DFT) or melt-quench molecular dynamics during structure generation.

In this chapter, we describe modifications to the WWW algorithm used to generate structures as well as overcoming difficulties produced by varying density. We cover the details of DFT calculations using Quantum Espresso. We also discuss how to characterize voids using Zeo++ [201] and how we correlate those voids to structural effects. We finally comment on overall structural changes and then the localized changes near to voids and conclude.

3.3 Methodology

3.3.1 CHASSM

We allow the structure to evolve using a step-dependent temperature (T) profile to ensure escape of the crystal phase and local minimization in the amorphous regime of the energy landscape. Introducing tensile strain alters the landscape, thus requiring higher initial T to amorphize. The temperature profile consists of three phases. An initial 'randomization' phase of 800 swap attempts/atom at high T (about 0.8 eV) is used to escape the crystal barrier while highly distorting the bonding network. The next 'anneal' phase consists of 100 swap attempts/atom at decreasing T (0.8 to 0.4 eV in $0.002-0.05$ sized intervals); this slow cooling allows improvement of the bonding network while the system traverses small barriers in the rough landscape [25, 165] to reach local minima. Finally, we 'quench' (100 swap attempts/atom at $T = 0$) to relax and ensure the system is at a local minimum.

Note that given the significant energetic and entropic barriers between different amorphous structures, straining structures to a different density and simply relaxing (as for studying effects of small strain [168]) would not produce as much structural variation as we find here, and would not correspond to the experimental growth to different densities which we are targeting.

If the randomization T is too low, the network will not be sufficiently perturbed from a perfect lattice and reverts to a crystal [207] and drop to a low energy as shown in Fig. 2.1. We encountered an opposing problem: if the randomization T is too high, the bonding network distorts too far from a physical one to be annealed. Since the Keating potential does not rely on nearest neighbors, atoms may be within coordination shells but have no interaction if they are not "bonded" according to the bond table [193]. Structures with too large a randomization temperature may be artificially over-coordinated: they may have 9+ atoms within the first coordination shell but only four Keating bonds. Structures of this kind will have very high energies shown in Fig. 2.1. To remedy this, we find ideal randomization T empirically: we randomize structures at variable temperatures for 1000 steps for each density, the smallest temperatures that escape the crystal phase are chosen. Ideal temperatures minimize the number of failed structures due re-crystallization or artificial coordination. We find the ideal temperature to be $T = 0.82$ eV$-(\rho - \rho_0)$ 0.18 eV/10^{22} at/cm^3, where $\rho - \rho_0$ is the difference between the density ρ and the relaxed crystal density, $\rho_0 = 5.0\times10^{22}$ at/cm^3. At densities below 3.4×10^{22} at/cm^3, T required to overcome the initial barrier will always over-distort the bonding network. Densities above 5.8×10^{22} at/cm^3 will always be over-coordinated; we discard structures with any atoms with 5+ atoms within the first coordination shell, since the Keating potential does not describe them well. Our densities are thus limited by those two values. Hydrogenated structures have a larger range of usable T than pure a-Si structures but follow the same ideal T trend, which we attribute to the more flexible bonding network when Si-Si bonds are replaced with Si-H bonds.

The algorithm can be disrupted by identical bonding: two atoms may be bonded to the same set of four atoms but not to each other. Atoms will inevitably rest on top of each other after relaxation yet feel no mutual interaction. The likelihood of this event increases with the system size and is particularly important to address for structures of 1000+ atoms. We solved this by rejecting swap attempts that would cause two atoms to have the same set of bonds. It could also be remedied by including distance-based repulsive terms to the potential [193, 166].

We use CHASSM to generate ensembles of structures at variable densities of both a-Si (Si_{216}) and a-Si:H ($Si_{216}H_{20}$) from 3.4 to 5.6×10^{22} at/cm^3 in intervals of 0.16×10^{22}. 10 structures per density are sampled to be further relaxed using plane-wave DFT. Stresses of ±1 GPa are common in a-Si:H [77], and in this work we reach 5 GPa. Cells are fixed as simple cubic, with lattice constant ranging from 15.6 Å to 18.5 Å at the highest and lowest densities respectively. Structural parameters of DFT-relaxed structures are calculated and error bars displayed are the standard errors of the population of 10 structures. The structural parameters of the original

CHASSM structures in the full data set (bond lengths, bond angles, bond angle deviations) are found to be very similar to the results of DFT relaxation, and are not shown. Pressure results are from a stress calculation in CHASSM implemented in the approach for classical potentials in periodic systems detailed in an article by Thompson *et al.* [178], using their equations (28) and (29).

3.3.2 DFT

We use Quantum Espresso [50] to perform fixed-cell relaxations at the Γ point using the PBE exchange-correlation potential [139] and ultrasoft pseudopotentials (USPP) [189]. We set the wavefunction kinetic energy cutoff to 38 Ry and 46 Ry for *a*-Si and *a*-Si:H respectively. Charge density cutoffs (requiring special care for USPP) were set to 151 Ry and 221 Ry for *a*-Si and *a*-Si:H. WWW structures were relaxed until forces and energies were converged to 10^{-4} Ry/Bohr^2 and 10^{-4} Ry respectively. These values were chosen because lowering thresholds only affected the atomic positions by less than 10^{-6} Å. Structures at very low and high densities, required smearing to converge the self-consistent cycle, possibly due to unpaired electrons at floating or dangling bonds. For relaxed-density calculations, we perform variable-cell relaxations until the stress tensor elements are below ±0.01 kbar. *a*-Si structures below 3.6×10^{22} at/cm^3 did not reliably converge self-consistent field cycles. After DFT relaxation, we consider atoms within 2.8 Å of each other bonded; bond lengths, angles, and dihedrals are computed from this bonding network.

3.3.3 Void characterization

We delegate our void characterization to Zeo++ [201], an open-source code developed to study the structure of void channels in zeolites. The code's pore-size distribution [140] function samples "test points" in the material and records the radii of the largest sphere encapsulating each point without touching any atoms. Note that this method interprets what could be considered a complex-shaped void (as in Biswas *et al.* [16]) as several spherical voids. We find our characterization to be appropriate if we are not concerned with details of the voids' surface structure.

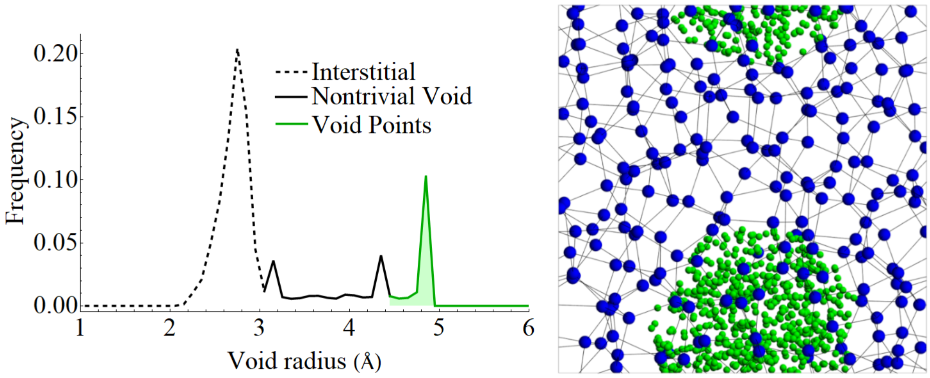

Figure 3.1: (top) An example low-density (4.3×10^{22} at/cm^3) a-Si structure with a large void. The green void points fill in the largest voids. (bottom) The pore size histogram of a low-density (4.05×10^{22} at/cm^3) post-DFT structure. Large voids (4.9 Å) and voids of a common size (2.5 Å) appear as strong signals in this histogram. Interstitial voids (dashed) are ignored in void analysis. Area underneath the solid region constitutes the void volume. Only void points belonging to the largest voids (green) are considered for the void proximity (r_v) analysis.

We have set the atomic radii and probe size to zero, and we have only considered Si atoms for void analysis to be able to directly compare a-Si to a-Si:H. All structures show a strong peak of interstitial-like voids (Fig. 3.1), a broadened version of the single crystal peak which appears at 2.4 Å. Low-density voids will appear as one or more peaks beyond the interstitial peak. To quantify the total void volume, we ignore the interstitial peak from the distribution. Void concentration in our low-density calculations is 2 orders of magnitude larger than that found by Biswas *et al.* around the equilibrium density [16], a sign that our small supercell may not be suitable to obtain this measure. Void sizes are also limited by our supercell. To find the atomic densities of the non-void parts of the structure, we set the radii of Si atoms to 2.21 Å, the Si Van der Waals radius. Renormalized densities are calculated $\rho_{norm} = \rho / N_{atomic}$, where N_{atomic} is the proportion of test points that fall within 2.21 Å of any Si atoms. Mono- and divacancies, which are important to many experiments and computations [161, 12, 83], have signals at 2.5 and 3.0 Å; since we are not generating vacancies through atomic removal, we do not see any such signals.

We locate large voids by considering test points corresponding to the largest

10% of spheres in a given structure to be that structure's "void points" (pictured in Fig. 3.1). We assign a void proximity measure to every atom, r_v, the shortest distance from that atom's center to a void point. We associate this distance with structural parameters to study how far voids' influence extends into the material.

3.4 Results and Discussion

3.4.1 Dependence of structure and bonding on strain initialization

We can probe the differences between pre- and post-DFT bond topologies to assess the validity of CHASSM structures. Any atoms whose local bonding has been readjusted (whether by a broken or new bond) is counted as a bond correction. Away from relaxed densities, these events are more common, at worst 3% compared to the 0% near relaxed densities. Atomic positions are corrected by DFT on average by 0.04 Å. We take these as evidence that DFT preserves the topology created by the Keating potential reasonably well, except at the most extreme densities we have studied.

Network ring analysis (calculated using King's method [85] with the open-source code R.I.N.G.S. [98]) are consistent with previous works [34]. There is little density-dependence in the ring statistics of *a*-Si:H. An increase in *a*-Si six-membered rings at the lowest densities is present—consistent with the observed hexagonal sheets.

Our calculated pair distributions $g(r)$ are shown in Fig. 3.2. We find they have little dependence on density, and are very similar for *a*-Si and *a*-Si:H. A 2.2 Å peak in the H-H pair distribution function is consistent with SiH_2 bonding networks found in divacancies created with molecular dynamics [24] and experiment [9]. This peak is a sign that H atoms preferentially cluster near the interior of voids.

We benchmark the density, elastic properties, and structural parameters at the relaxed density in Table 3.1. The densities of both *c*-Si and *a*-Si are underestimated by PBE by 0.1×10^{22} at/cm^3. The relaxed *c*-Si CHASSM density (by choice of the

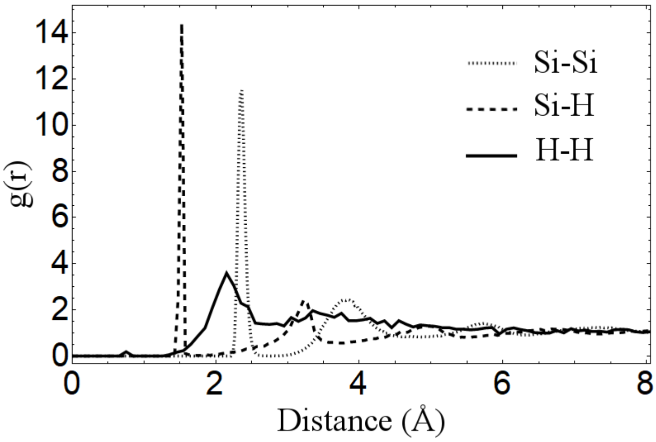

Figure 3.2: Averaged partial pair distribution functions, $g(r)$, for a-Si:H at all densities. $g(r)$ for a-Si is identical to the Si-Si distribution in a-Si:H. Decreasing density increases the height of the H-H 2.2 Å peak, but has little effect on the other curves.

Keating parameters α, β, and δ) matches experiment, but a-Si is incorrectly denser than c-Si, as noted in the original WWW work [207]. This does not affect results for a fixed density though. Elastic constants are described well by CHASSM only for c-Si near relaxed densities (Fig. 3.3), due to the lack of any dependence beyond harmonic in the Keating potential, but the DFT elastic constants agree well with experiment. Structural parameters agree well with experiment, and we find similar levels of agreement for a-Si and a-Si:H.

Pressures (trace of the stress tensor) calculated using the Keating potential are significantly lower than those obtained from DFT, but they have a similar trend with a constant offset in Fig. 3.3. Pressures vary linearly with density above 4.5×10^{22} at/cm^3. A sudden drop in absolute pressure occurs at the critical density between 4.3 and $4.5{\times}10^{22}$ at/cm^3. These densities are consistent with the onset of voids in Fig. 3.4. This behavior shows the same physical mechanism as cavitation and bubble formation at low pressures in liquids [17]. A sharp drop in pressure at low densities is similarly observed in classical molecular dynamics simulations of water [199]. At low densities, small voids are non-existent, they have instead coalesced into one large void or even channel. Once voids approach the size of our supercell, they are likely to meet their periodic neighbors and form

Table 3.1: Relaxed density parameters of CHASSM, CHASSM+DFT, and experiment of *c*-Si, *a*-Si, and *a*-Si:H

		ρ_0 ($10^{22}\ \frac{\text{at}}{\text{cm}^3}$)	Y (GPa)	B (GPa)	$\langle r_0 \rangle$ (Å)	$\langle \theta \rangle$ (°)	$\Delta\theta$ (°)
CHASSM	*c*-Si	5.01	162	97	2.35	109.5	0
	a-Si	5.12	180	77	2.33	109.3	9.6
	a-Si:H	5.07	166	64	2.34	109.3	9.9
CHASSM +DFT	*c*-Si	4.87	153	82	2.37	109.5	0
	a-Si	4.78	138	59	2.36	109.2	10.3
	a-Si:H	4.67	129	60	2.38	109.1	11.0
Exp't	*c*-Si	5.01	165	98	2.35	109.5	0
	a-Si	4.9	140	140	2.38	108.5	8-11
	a-Si:H	4.9	126	59	2.36	108.4	8-11

Relaxed density parameters of CHASSM, CHASSM+DFT, and experimental *c*-Si [64], *a*-Si [205, 141, 45, 157, 150], and *a*-Si:H [93, 174, 154, 45, 150, 149]. Density values are in 10^{22} at/cm^3, Young's moduli (Y) and bulk moduli (B) are in GPa, mean bond lengths ($\langle r \rangle$) are in Å, and mean bond angles ($\langle \theta \rangle$) and angle deviations ($\Delta\theta$) are in degrees.

connected channels. This could be related to the observation in water that at low enough densities, spherical cavitation evolves to cylindrical cavitation [199]. We conclude that voids have been created to relieve the global pressure caused by a highly strained bonding network. The pressure stabilizes to a constant value at the lowest densities for all data sets.

This picture of cavitation is reinforced by examination of bond lengths and angles (Fig. 3.5), which have a transition around the critical density 4.3×10^{22} at/cm^3. Bond lengths in *a*-Si increase as density is decreased, but then decrease again back to the relaxed value after stress relief with void formation. The small magnitude of bond length changes seem consistent with the results of Jacks and Molina-Ruiz *et al.* [71], from electron-energy loss spectroscopy (EELS). Overall, *a*-Si:H structures react more smoothly to strain because of the degrees of freedom discussed in section 3.3.1. The increase in $\Delta\theta$ at low density, the typical measurement of amorphous order as inferred from the TO peak width in a Raman spectrum [8], is also consistent with Jacks and Molina-Ruiz *et al.* [71], although we see a larger

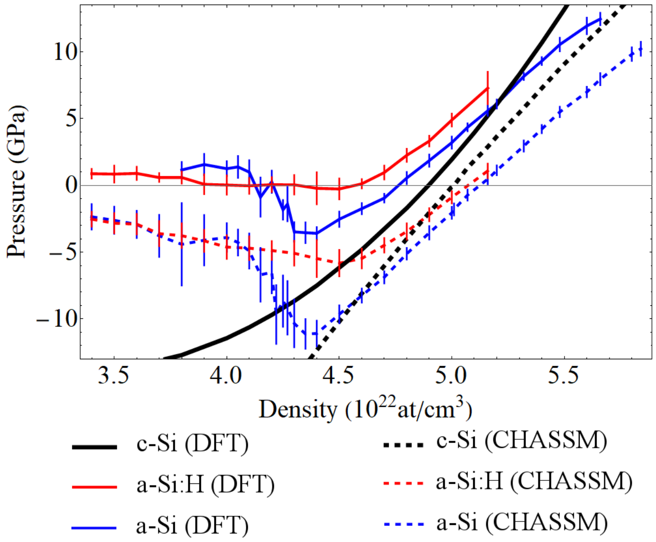

Figure 3.3: CHASSM (solid) and CHASSM + DFT (dashed) calculated pressures *vs.* densities. As density is decreased in *a*-Si and *a*-Si:H, negative pressure is induced, but then relieved near the void onset density of 4.3–4.5$\times10^{22}$ at/cm^3, like the cavitation process of bubble formation. CHASSM pressures are systematically too low compared to DFT, but have the correct trend. *a*-Si has a more abrupt transition than *a*-Si:H.

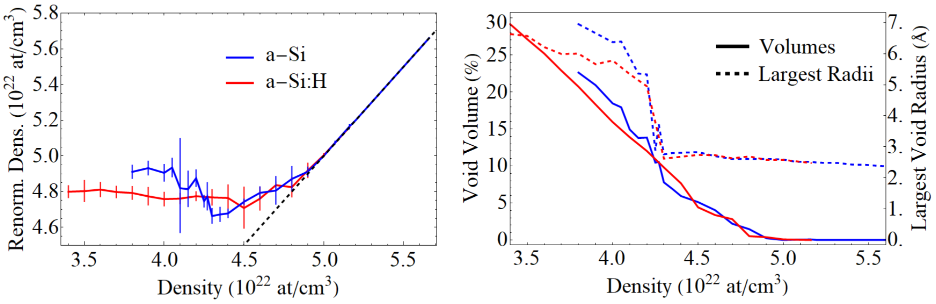

Figure 3.4: Renormalized atomic densities (top) indicate the density of the non-void regions, showing that void formation allows the rest of the sample to retain a constant density. (bottom) The encapsulating sphere method directly confirms that voids start forming at 4.3–4.5$\times10^{22}$ at/cm^3. Above the critical density, largest void radii are of about the size of the interstitial and total void volume is nearly 0% of the total volume.

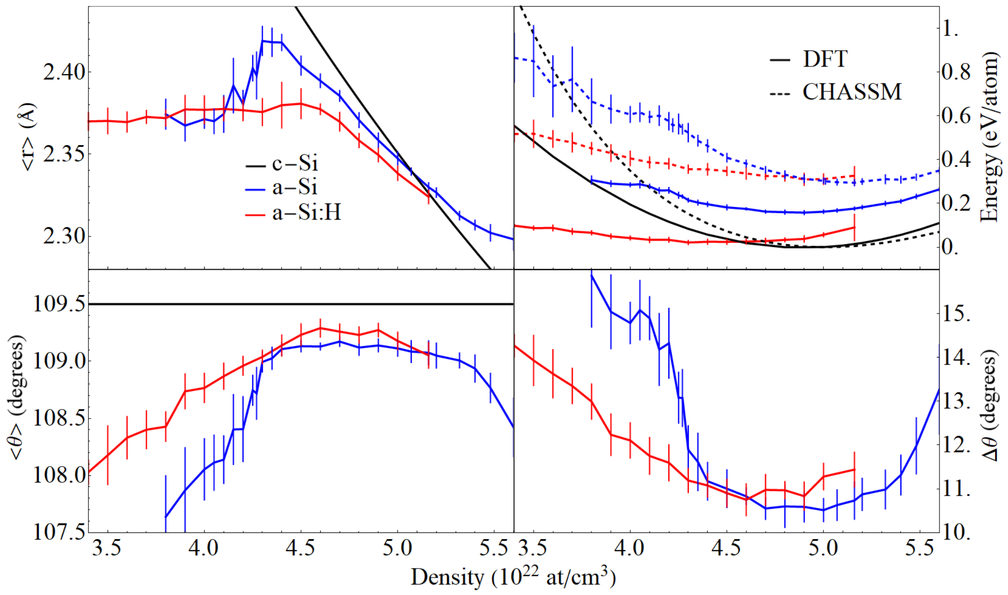

Figure 3.5: Response of structural parameters to density variation. Bond lengths and angles change trends around 4.3×10^{22} at/cm^3, the density of void onset shown in Fig. 3.4. Relaxed *c*-Si has a CHASSM energy of 0 eV and $\Delta\theta = 0$. *a*-Si DFT energies are relative to *c*-Si, *a*-Si:H energies are relative to the lowest *a*-Si:H energy in our data set.

increase, perhaps due to finite-size effects of our supercell or limitations in the experimental extraction of $\Delta\theta$ and density in the films. We find that $\Delta\theta$ increases at high densities also. The average bond angle decreases away from the relaxed density too, more dramatically for *a*-Si, which we will interpret in terms of effects near voids. The energies in CHASSM and DFT show increases away from the relaxed density, of course, but also a clear bump at the critical density for *a*-Si; no obvious feature occurs for *a*-Si:H. A constant trend of $\langle r \rangle$ at low densities is consistent with the stabilized renormalized density in Fig. 3.4. These plots combined imply that Si-Si bonds have stopped stretching and begin to relax as a result of cavitation. Flattening of this atomic network density at low global densities is consistent with Rutherford backscattering spectroscopy and atomic force microscopy data [71].

Dihedral distributions show an unexpected density-induced variation. It is often considered that there is a uniform distribution of dihedrals in *a*-Si, inferred from the third nearest-neighbor peak in $g(r)$ as measured by X-ray diffraction [154]. However, our results show instead sinusoidal variation, with distinct peaks at 60° and 180° similar to what has been found in other computational studies [135, 130]. For comparison, *c*-Si has 2/3 of the dihedrals as 60° and 1/3 as 180°. To describe the density dependence, we restrict ourselves to Si atoms only and fit the dihedral distributions to the form $A\cos(2\pi/120°) + D$. D is density-invariant, but A, which we term the dihedral amplitude, is a measure of the strength of dihedral order. Increasing the density increases the magnitude of A (Fig. 3.6), indicating a stronger medium range order at high densities. Lowest density structures seem to show a complete flattening such that $A \to 0$. Below 4.3×10^{22} at/cm^3, the relationship reverses and angles at 0° and 120° are more likely to be found than 60° or 180°. Curiously, the lowest density *a*-Si structures with strong 0° peaks are found to contain hexagonal bilayer sheets (like a graphene bilayer with AA stacking). We presume that these structures are unphysical artifacts of the Keating potential, and indeed the change of structure with DFT relaxation is increasingly large around these densities. Hexagonal bilayer sheets are compatible with large free surfaces while tetrahedrally coordinated structures necessarily suffer large deformations to their bond angles near a void. In *a*-Si:H, A does not go above 0 and we have not

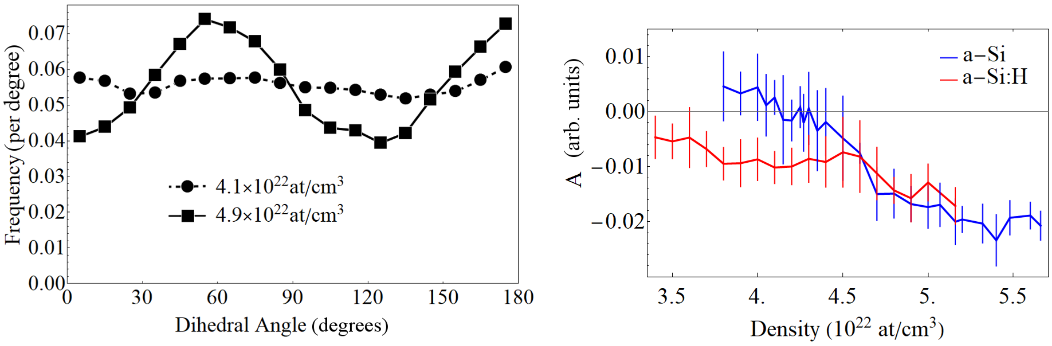

Figure 3.6: (top) The relationship between density and the dihedral amplitude, A, in low and high density *a*-Si structures. A is a direct measure of the dihedral order, it increases as the density increases. (bottom) Dihedral distributions for a low (4.1×10^{22} at/cm^3) and relaxed (4.9×10^{22} at/cm^3). Dihedral order vanishes at the lowest densities.

found evidence of hexagonal sheet structures.

3.4.2 Structural differences near voids

In low-density structures with large voids, structural deformations are associated with void proximity, r_v. To isolate local structural parameters from, we group atoms based on their r_v and collect bond lengths and angles associated with those atoms. $\Delta\theta$, $\langle\theta\rangle$, $\langle r\rangle$, and $\langle C\rangle$ are now computed on those sub-populations. Accurate description is limited by half the cell size minus the void diameter, to a distance of about 7 Å away from a void surface. In a given low-density structure, the increased bond angle deviation resides entirely around the surface of voids as shown in Fig. 3.7. Bond lengths and angles near the void surface do not resemble the *c*-Si (100) reconstruction considered by Carlson in a light-induced degradation model [23] and invoked in the literature [40]. Results of 1-2% increase in bond lengths and increasing local $\Delta\theta$ are consistent with atomic removal methods [83]. We have pictured the motif for increase in local bond angles in Fig. 3.7. Away from voids, the deviation returns to relaxed-like values of 10°. These results show conclusively that the structural changes below the 4.3×10^{22} at/cm^3 critical density are driven voids.

Our low-density *a*-Si ensembles include structures that contain voids while

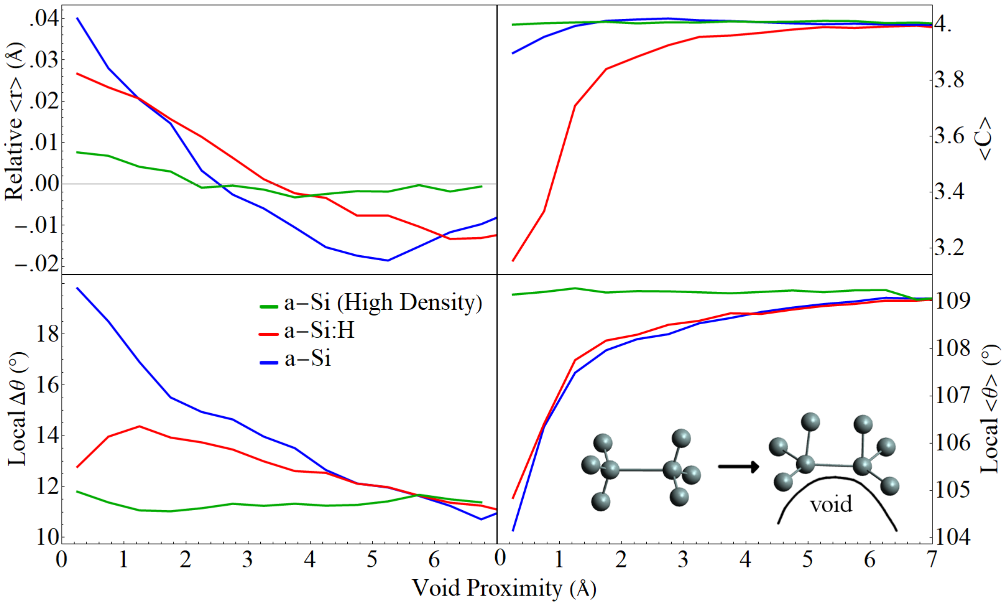

Figure 3.7: Locally resolved structural response of low density structures as a function of void proximity. *a*-Si and *a*-Si:H lines are structures below 4.3×10^{22} at/cm^3. High density structures (green) are plotted to contrast, since the largest voids in these structures are not distinguishable from interstitials there is little correlation between structural deformation and void proximity. $\langle r \rangle$ are calculated with respect to average bond lengths for each given density. $\langle C \rangle$ is the average Si-Si coordination number. The results are consistent with a local rearrangement of bonds to accommodate a void as shown in the bottom-right sketch.

maintaining perfect 4-coordination without H insertion, albeit at a cost of high local strains. This feature is not obtained by Si removal methods, since 3-coordinated atoms are generated by design and void surfaces must reconstruct [132]. This may have implications in experiments, such as H effusion, which rely on the presence of H to measure voids, or electron spin resonance, which rely on coordination defects at the void surface. It may be possible that macroscopic structures with both H-filled or entirely empty voids exist.

Fig. 3.2 and the $\langle C \rangle$ plot in Fig. 3.7 provide evidence that H clustering in *a*-Si:H. H atoms are highly concentrated within voids, especially at low densities. This is significant since we did not explicitly place H atoms at the void surfaces, as in some previous work, but the H atoms naturally ended up there from the Monte Carlo process and annealing. This result is consistent with previous studies [24, 208, 128].

3.5 Conclusion

Using a pure WWW method with different fixed densities, we are able to generate realistic *a*-Si and *a*-Si:H structures with voids that can be used to study degradation, two-level system phenomena, or H-mediated changes to elastic parameters. The method is simple and scales well with system size [5], and requires no atomic addition or removal, or any *a priori* idea of the targeted structures. *a*-Si coordinates obtained from this method are unique for their near-perfect coordination in the presence of voids without H passivation. Since 4-coordinated void structures are obtainable, it may be possible that experimental *a*-Si:H contains *a*-Si voids with no H involved that have thus far been ignored by some experimental measurements.

Studies by Nakhmanson and Drabold [124] suggest strong locality of some low-energy phonon modes near void surfaces. These may be a product of low coordination near voids produced by atomic removal and may be worth revisiting with fully 4-coordinated pure *a*-Si void structures. These phonon modes may have strong implications on two-level systems [117].

Structural analysis of *a*-Si and *a*-Si:H at low density indicate less tetrahedral bond angle distributions and nonlinear bond lengths stretching. *a*-Si:H responds more smoothly to strain than *a*-Si due to a less constrained network. The increase in negative pressure and then reduction below the critical density indicates the bonding network undergoes a bubble-like cavitation process—the formation of large voids to relieve internal stresses. By resolving structures at an atomic level, we conclude that the structural changes at low density reside near void surfaces. The locality of this structural disorder may be related to two-level systems [117]–structures generated here can be used to study such phenomena. We find in *a*-Si:H that H atoms tend to be concentrated near voids. We verified the validity of the WWW and Keating potential description across a range of densities near the relaxed one, except for the most extreme densities studied.

Chapter 4

a-Si Potential Energy Surface: Analysis of the Amorphous Configurational Energy Gap

This chapter is based on unpublished work and is assembled based on work that was generated for the previous chapter, but did not fit that chapter's theme. Instead, the works here are related to the high-dimensional, fractal [25] potential energy surface of *a*-Si systems with respect to changing atomic coordinates and bonding network. Motivations originally stemmed from the observation that the energy and bond angle deviations, $\Delta\theta$, of all 700 structures were statistically associated. This chapter begins to lay the foundation for expressing the complicated energy in an amorphous system in terms of mostly just one parameter—$\Delta\theta$.

The potential energy landscape of amorphous Si shows a striking feature with no direct explanation—an energy gap between the crystalline and amorphous phases [37]. Amorphous silicon (*a*-Si) is not found between 0 and about 0.07 eV/atom above crystalline Si (*c*-Si). This configurational energy gap is surprising when the potential energy surface's local minima are considered, i.e. a large number of atoms lead to an exponential number of unique configurations [165], and yet there is not a gradient of configurations that reaches between the crystalline and amorphous phases. The fractal nature [25] of the energy landscape means that relaxation schemes must consider overcoming barriers of arbitrary size while

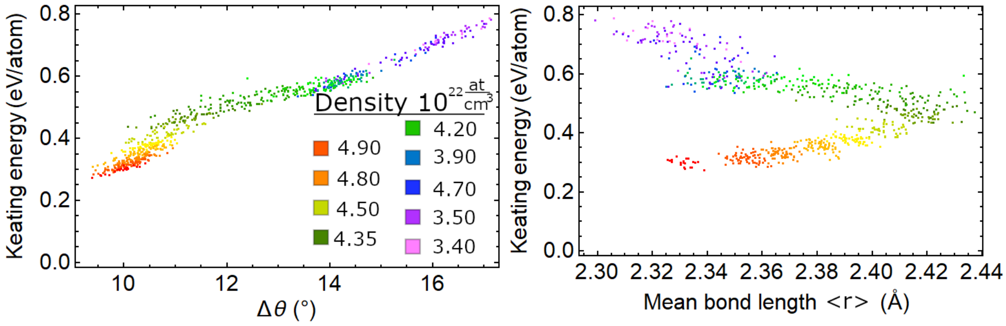

Figure 4.1: The Keating energy as a function of the average bond angle deviation and mean bond length for the 700 structures generated by CHASSM. The upper tail in the bond length plot is due to the phase changes discussed in Ch. 3.

relaxing.

The Wooten-Winer-Weaire (WWW) [207] and Keating potential [82] combination described in Chs. 2 and 3 has a built-in feature: a bond-switch move followed by structural optimization that constitutes a change in configuration that amounts to moving from one minimum in the energy landscape to a nearby one. Each of the initial successful moves as applied to *c*-Si forces the system up the steep crystalline well as in Fig. 2.1. Once sufficiently randomized, barriers to changing between two amorphous states are significantly smaller and the system has changed phases. As noted in Ch.3, the bonding network is preserved relatively well when sending Keating-relaxed structures through DFT. We will use those structures generated and further interrogate them to gain insight as to the configurational energy gap.

Absent from Drabold's description of the configurational energy gap [37] is mention of the bond angle deviation, $\Delta\theta$. This order parameter also shows a gap. The $\Delta\theta = 0^\circ$ for a crystal, but the smallest $\Delta\theta$ for the 700 CHASSM [169]-generated structures was 9.38°. Smaller values were only observed in structures that were mostly crystalline, but these were tossed out as failed attempts at amorphization. We find near linear relationships between small changes in structure bond angle deviations and quadratic relationships to bond length averages in Fig. 4.1.

A strong relationship between E and $\Delta\theta$ is not surprising if we rewrite the Keating potential as a statistical average over a large number of structures. The form of the raw potential is as follows [82]:

$$U = \frac{3\alpha}{16\delta^2}\sum_{i=1}^{N_{\text{atoms}}}\sum_{j=1}^{N_{BL,i}}(|\vec{r}_{ij}|^2-\delta^2)^2+\frac{3\beta}{8\delta^2}\sum_{i=1}^{N_{BL,i-1}}\sum_{k>j}^{N_{BL,i}}(\vec{r}_{ij}\cdot\vec{r}_{ik}+\frac{1}{3}\delta^2)^2 \tag{4.1}$$

where α and β are bond length and angle force constants, δ is the rest Si-Si bond length, $N_{BL,i}$ is the number of atom i's bond lengths (set to 4 for non-hydrogenated a-Si), r_{ij} is the bond length vector from atom i to it's jth bonded atom. We have set α, β, and δ as 2.965 eV/(Å^2), 0.845 eV/(Å^2) , 2.35 Å respectively, to match previous, successful values for c-Si [5].

We have compared the Keating energy of structures at varying densities against their geometries. We can rewrite the Keating potential, which was built for crystals, to tell us about ensemble averages of amorphous structures through the average bond lengths and bond angle deviations. Here, we rewrite U as being a function of $\langle r\rangle$ and $\Delta\theta$, properties of an entire structure:

$$\langle U\rangle = \frac{3\alpha}{8\delta^2}\langle N_{\text{bonds}}\rangle(\langle r\rangle^2-\delta^2)^2+\frac{3\beta}{8\delta^2}\langle N_{\text{angles}}\rangle\langle(\vec{r}_i\cdot\vec{r}_j+\frac{1}{3}\delta^2)^2\rangle$$

$$\langle\frac{U}{N}\rangle = \frac{3\alpha}{8\delta^2}\times 2(\langle r\rangle^2-\delta^2)^2\rangle+\frac{3\beta}{8\delta^2}\times 6(\langle r\rangle^4\langle\cos^2\theta\rangle+\frac{2}{3}\delta^2\langle r\rangle^2\langle\cos\theta\rangle+\frac{1}{9}\delta^4)$$

$$\langle\frac{U}{N}\rangle = \frac{3\alpha}{4\delta^2}(\langle r\rangle^2-\delta^2)^2+\frac{\beta}{4\delta^2}(\langle r\rangle^4(1+7(\Delta\theta)^2)-2\delta^2\langle r\rangle^2(1+\frac{1}{2}(\Delta\theta)^2)+\delta^4). \tag{4.2}$$

We force $N_{\text{bonds}} = 2N$ and $N_{\text{angles}} = 6N$ for a-Si. We have assumed $\Delta r = \theta$ and thus $\langle r^2\rangle = \langle r\rangle^2$, where $\langle r\rangle$ is a given structure's average bond length. $\langle r^2\rangle$ is roughly .06% larger than $\langle r\rangle^2$. We assume $\langle\theta\rangle = \theta_t \approx 109.5^\circ$, this value does show a density-dependent drop of about 2° [55], but we have taken this as insignificant. If we recall that $(\Delta\theta)^2 = \langle\theta^2\rangle - \langle\theta\rangle^2$, then $\langle\cos\theta\rangle = \frac{-1}{3}(1+\frac{1}{2}(\Delta\theta)^2)$ and $\langle\cos^2\theta\rangle = \frac{1}{9}(1+7(\Delta\theta)^2)$ through Taylor expansion about θ_t. The weakest assumption made is that bond lengths r and angle projections $\cos\theta$ are uncorrelated: $\langle r^2\cos\theta\rangle = \langle r^2\rangle\langle\cos\theta\rangle$.

These assumptions allow us to write the Keating potential as a function of only $\langle r\rangle$ and $\Delta\theta$. We can plot these equations of state against the actual $\langle r\rangle$ and U/N in a structure while fixing $\Delta\theta$ and vice-versa as in Fig. 4.2. By setting $\langle r\rangle = \delta$ in

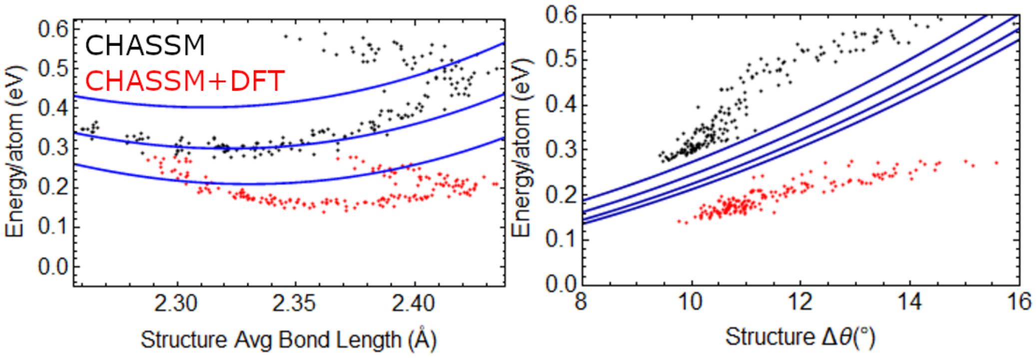

Figure 4.2: Keating energy/atom of CHASSM structures (Black) versus those structures' average geometry parameters r and $\Delta\theta$. Total DFT Energy/atom (red) show similar structure when varied by density. Theoretical (blue) lines for constant values of $\Delta\theta$ (from bottom to top: 10, 12, 14 °) and r (from bottom to top: 2.35, 2.37, 2.39, 2.41 Å).

Eq. 4.2 we reach Eq. 4.3:

$$\langle\frac{U}{N}\rangle = \frac{3\beta\delta^2}{2}(\Delta\theta)^2. \tag{4.3}$$

According to Eq. 4.3, the energy U does not show a continuous evolution from crystal to amorphous because $\Delta\theta$ does not. $\Delta\theta$ does not fall below 9° in a given structure, so the Keating energy will not fall below 0.18 eV/atom above *c*-Si. We find the DFT-relaxed energies are lower than their classical Keating counterpart and the spreads have also been reduced. In both cases, however, the shapes are distinguishable. There is a quadratic relationship in the $\langle r\rangle$-dependent form until there is large tensile strain. This tensile strain leads to void formation causing non-linearities at qualities related to low-densities, as discussed in the previous chapter. Fits to the $\Delta\theta$-dependent form shows a slightly reversed parabola when compared to the data in Fig. 4.2. There is an overall underestimation of the CHASSM energy, but an overestimation of the DFT-energy.

Ch. 3 shows that there is predictability in the structural parameters as a function of generation density. These give variable r and $\Delta\theta$ suitable to test equations 4.2 and 4.3. Focusing on the Keating energy, we can combine the models and compare the full Keating energy to the structure-average models in Eqs. 4.2 and 4.3. We see the inverted-parabola shape disappear, as it is explained as bond

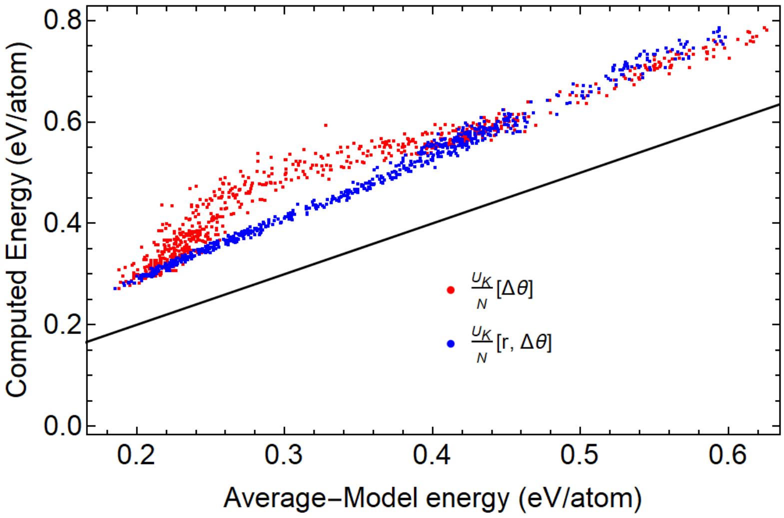

Figure 4.3: The Keating energy in two forms—as Eq. 4.2 (blue) and Eq. 4.3 (red). The bond length correction is significant away from equilibrium. Even with the correction, fully computed energies are about 0.05 eV/atom above the average models.

length strains. Still, there remains a small gap between the averaged model and the computed energy. We thus far hypothesize that the gap is related to the $\langle r^2 \cos\theta\rangle$ correlation terms.

Further processing of the structure may definitively reveal the source of the average-model gap. In turn, the formulation with structure-averaged dependencies may simplify the crystalline/amorphous energy gap. The strong linearity of the form based on 4.2 in Fig. 4.3 leads to a model that can predict the DFT energy when ensembles of structures are considered.

4.1 Supplementary Material

The following derivation applies a Taylor expansion about the tetrahedral angle. This is used in finding Eqs. 4.2 and 4.3.

Assumptions:

$$\begin{aligned} \langle\theta\rangle &= \theta_t \\ \langle r^2\rangle &= r^2 \\ \langle f(r)g(\theta)\rangle &= \langle f(r)\rangle\langle g(\theta)\rangle \\ (\theta-\theta_t) \text{ is small} \cos\theta_t &= -\frac{1}{3}, \sin\theta_t = \frac{2\sqrt{2}}{3} \end{aligned}$$

Expectation value of Taylor expansion of $\cos\theta$ and $\cos^2\theta$ about θ_t

$$\begin{aligned} \cos\theta &= \cos\theta_t - \sin\theta_t(\theta-\theta_t) - \frac{1}{2}\cos\theta_t(\theta-\theta_t)^2 + \mathcal{O}(\theta-\theta_t)^3 \\ \langle cos\theta\rangle &\approx \cos\theta_t - \sin\theta_t(\langle\theta\rangle-\theta_t) - \frac{1}{2}\cos\theta_t(\langle\theta^2\rangle - 2\theta_t\langle\theta\rangle + \theta_t^2) \\ &= \cos\theta_t - 0 - \frac{1}{2}\cos\theta_t(\langle\theta^2\rangle - \theta_t^2) \\ &= -\frac{1}{3} + \frac{1}{6}(\Delta\theta)^2 \\ \cos^2\theta &= \cos^2\theta_t - 2\cos\theta_t\sin\theta_t(\theta-\theta_t) - \cos^2\theta_t(\theta-\theta_t)^2 + \\ &\sin^2\theta_t(\theta-\theta_t)^2 + \mathcal{O}(\theta-\theta_t)^3 \\ \langle\cos^2\rangle &\approx \cos^2\theta_t - 2\sin\theta_t\cos\theta_t(\langle\theta\rangle-\theta_t) - (\cos^2\theta_t - \sin^2\theta_t)(\Delta\theta)^2 \end{aligned}$$

$$= \frac{1}{9} + \frac{7}{9}(\Delta\theta)^2 \tag{4.4}$$

Chapter 5

Ni-doped MoS_2: Structure, Vibrational spectroscopy

This chapter has been reprinted with permission from the Journal Physical Chemistry C 2021, 125, 13401-13412. Copyright 2021 American Chemical Society [58]. Here, we cover our analytical methods to study the thermodynamic stability, electronic structure, and vibrational spectroscopy of Ni-doped MoS_2 using density functional theory and density functional perturbation theory. Generation of these structures was inspired by the parametrization of a force field discussed in Ch. 7 for use in studying friction between layers. This chapter lays the foundation for that work and interrogates the doped structure and its properties at the microscale.

5.1 Abstract

Ni-doped MoS_2 is a layered material with useful tribological, optoelectronic, and catalytic properties. Experiment and theory on doped MoS_2 has focused mostly on monolayers or finite particles, theoretical studies of bulk Ni-doped MoS_2 are lacking and the mechanisms by which Ni alters bulk properties are largely unsettled. We use density functional theory calculations to determine the structure, mechanical properties, electronic properties, and formation energies of bulk Ni-doped 2H-MoS_2 as a function of doping concentration. We find four meta-stable structures of Ni-doped MoS_2: Mo or S substitution, and tetrahedral (t-) or oc-

tahedral (o-) intercalation. We compute phase diagrams as a function of chemical potential to guide experimental synthesis. A convex hull analysis shows that t-intercalation (favored over o-intercalation) is quite stable against phase segregation and in comparison with other compounds containing Ni, Mo, and S; the doping formation energy is around 0.1 meV/atom. Intercalation forms strong interlayer covalent bonds and does not increase the *c*-parameter. Ni doping creates new states in the electronic density of states in MoS_2 and shifts the Fermi level, which are of interest for tuning the electronic and optical properties. We calculate the infrared and Raman spectra and find new peaks and shifts in existing peaks that are unique to each dopant site, and therefore may be used to identify the site experimentally, which has been a challenge to do conclusively.

5.2 Introduction

Transition metal dichalcogenides (TMDs) are lamellar materials with strong covalent intralayer bonds and weak Van der Waals interlayer bonds. MoS_2 is a semiconducting TMD with interesting optical [11, 119], electronic [11], spintronic [151, 95], lubrication [191], and catalysis [111, 196, 120] properties which are often controlled using dopants. Doping MoS_2, especially with Ni, can increase catalytic activity and reduce friction [170, 192]. However, the mechanisms for these doping effects, and even the basic question of the sites occupied by Ni atoms, remain unclear. This work focuses on exploring Ni doping in bulk 2H-MoS_2 and the effects on materials properties as computed by density functional theory (DFT).

Much previous work about doped MoS_2 has been motivated by catalysis. MoS_2 has properties that are desirable in photo-, electro-, and thermocatalysis [111]. Though MoS_2 has poor intrinsic catalytic activity, it can be enhanced by dopants [176] to create defects (especially at edge sites [172, 143, 96, 195]) as active sites. Co- and Ni-doping have been studied theoretically [172, 60] and experimentally [90, 120, 96] showing enhancement of the hydrogen evolution reaction. Intercalation by Na, Co, Ni, and Ca has also been shown to increase catalytic activity in 1T-MoS_2 [4].

More recently, monolayer MoS_2 has shown promise for optoelectronic applications such as photovoltaics [183] or light-emitting-diodes [102]. Large exciton binding energies and long lifetimes of excitons in MoS_2 mean that the high absorption rate can be used to generate useful excitons at room temperature [183, 10, 229, 152]. Dopants can alter the Fermi energy by donating or accepting electrons and can tune these optoelectronic properties [11]. Monolayer and bulk 3R MoS_2 lack inversion symmetry, unlike the bulk 2H phase, giving rise to spin-orbit effects which can further be exploited for spintronic and valleytronic applications [151, 152]. Transition metal doping by Mn, Fe, Co, and Zn has been used to induce magnetism which could be used for spintronics [29, 176].

Bulk MoS_2 also has useful properties for the older application of lubrication: superior resistance to wear (the gradual loss of material caused by sliding [192]) and a low coefficient of friction (high lubricity) due to the ease of shearing along the basal plane [113]. As a solid lubricant, MoS_2 holds some advantage over liquid lubricants—notably it lubricates at temperatures and pressures low enough even for space applications [191]. Tribological properties can be enhanced via doping [176]. Re (in MoS_2 fullerene-like nanoparticles [144]) and Ta [170] have been observed to increase lubricity, and Cr and Ti have been found to strengthen the resistance to humidity while retaining MoS_2's high lubricity [35]. Ni is an exceptional dopant for increased wear protection, decreased coefficient of friction, and long-term stability [170]. Despite how long studied these materials are, correlation of macroscopic tribological properties and microscopic atomic structure has remained elusive, especially for 2D materials [65, 43, 191].

Previous studies suggest that Ni substitutes Mo at edge sites in small flakes [172, 143, 96, 195], but there has been little investigation of Ni doping in bulk. Some possibilities are suggested by studies of other dopants. Co [131] (chemically similar to Ni) and Ta [230] are thought to increase catalytic activity by insertion into S vacancies near the usually inert basal plane. In bulk, other ions [79, 232, 224, 223, 158] can intercalate between the layers (typically in the octahedral site) and increase interlayer spacing or even form ordered alloys [26]. A phase change from 2H to 1T with Li intercalation has been found via Raman spectra indicating a symmetry change from D_{6h} to D_{3d} [79]. Ni doping, presumably through surface energies, can control MoS_2 crystal size and growth rates [90, 120]. A study of Ni-doped MoS_2 nanostructures found signs of Ni substitution for Mo and a change to the 3R phase; shifts in diffraction peaks indicated contraction of the MoS_2 cell [120].

Vibrational spectroscopy has been a main tool for the characterization of 2D materials and their defects. n-type doping of MoS_2 is correlated with redshifts of the $A_{1\mathrm{g}}$ Raman-active peak and p-type with blueshifts while the $E^1_{2\mathrm{g}}$ Raman frequency remains unchanged. This behavior is found in field-effect doping as well [24]. With other transition metals, Nb-doping was found to cause an $A_{1\mathrm{g}}$ redshift [171] while Au caused a blueshift [159]. An $A_{1\mathrm{g}}$ redshift around 1 cm^{-1} for Ni-doped MoS_2 nanostructures was attributed to changes in number of layers [120]. A new 280 cm^{-1} peak was found in Ni-doped MoS_2 that was not related to either pure MoS_2 or nickel sulfides [90], but its origins have not been further characterized. Vibrational properties are also important for tribology as energy dissipation via vibrational states [175, 67] and electron-phonon coupling [43] (EPC) are thought to play a crucial role in increasing friction in 2D materials. Sheremetyeva *et al.* have studied Ag-doped MoS_2 using experiment and DFT and find shifts in low-frequency modes, demonstrating that peaks aside from the prominent $A_{1\mathrm{g}}$ and $E^1_{2\mathrm{g}}$ can be effective identification markers [158]. We have found few computational studies of doped bulk 2H-MoS_2 and experimental reports have rarely had sufficient resolution to identify dopant-related peaks. There is a clear need for more detailed Raman and IR studies since vibrational spectroscopy can be a powerful tool for characterizing defects. In this paper, we use first principles DFT calculations to systematically survey different structures and concentrations of bulk Ni-doped MoS_2 to definitively resolve the structure of this material. We determine phase stability to guide synthesis and show unusual stability of intercalated structures. We compute Raman and IR spectra to aid in experimental identification of defect structures (which may not be lowest energetically due to non-equilibrium growth), and study elastic and vibrational properties to understand how Ni improves performance in lubrication. By studying elasticity, bonding, and vibrations, we elucidate how Ni decreases friction and increases resistance to wear.

5.3 Methods

5.3.1 DFT Calculations

We use plane-wave density functional theory (DFT) and density functional perturbation theory (DFPT) [6] implemented in `QUANTUM ESPRESSO` [50] v6.4. Calculations were performed using the Perdew-Burke-Ernzerhof [139] (PBE) generalized gradient approximation and Perdew-Wang [138] local density approximation (LDA) exchange-correlation functionals with Optimized Norm-Conserving Vanderbilt pseudopotentials [62] parametrized by Schlipf and Gygi [153] (for PBE) and by PseudoDojo [187] (for LDA) obtained from their respective websites [187, 153]. Raman calculations were done only for LDA since PBE is not compatible with Raman intensity calculations in this code [97].

Relaxations and electronic structure of the primitive, 6-atom MoS_2 cells used a k-point grid of $6 \times 6 \times 4$ with a half-shifted k-grid. Increasing the supercell size to reach lower Ni concentrations allows decreasing k-points per axis in the in-plane a- and b-directions inversely proportional to the supercell size: $4 \times 4 \times 4$, $3 \times 3 \times 4$, and $2 \times 2 \times 4$ k-points per axis were used for $2 \times 2 \times 1$, $3 \times 3 \times 1$, and $4 \times 4 \times 1$ supercells, respectively. Atomic coordinates were relaxed using force thresholds of 10^{-4} Ry/Bohr and the stresses were relaxed to 0.1 kbar. Calculations were spin-unpolarized, except for ferromagnetic bulk Ni. Spin-polarization for other cases was found to affect the total energy by less than 0.001 meV per atom, thus having no significance for the properties considered here. The change is only non-negligible in bulk Ni, where the energy difference is 0.2 eV/atom.

A wavefunction cutoff of 60 Ry was used for PBE and 80 Ry for LDA. The self-consistency thresholds were set to 10^{-18} for the ground state and 10^{-15} for phonons. Strict thresholds were required for accurate calculations of modes with low frequencies. Low frequencies of vibrational calculations of 3×3 t-intercalation and Mo substitution were initially calculated to be imaginary and required special care to properly converge: k-points were increased to $4 \times 4 \times 4$ and the phonon self-consistent threshold was lowered to 10^{-16}. DOS calculations were carried out on fine k-grid meshes of $12 \times 12 \times 12$, $10 \times 10 \times 10$, $6 \times 6 \times 6$, and $6 \times 6 \times 6$ for $1 \times 1 \times 1$, $2 \times 2 \times 1$, $3 \times 3 \times 1$, and $4 \times 4 \times 1$ supercell sizes respectively.

5.3.2 Elasticity

Elastic parameters were calculated using the stress-strain relationship (using Voigt notation) $\sigma_i = C_{ij}\epsilon_j$. We applied uniaxial strains in the 1- and 3-directions and 5-direction shear strains to calculate C_{11}, C_{33}, and C_{55}. Strains were applied from -0.01 to 0.01 in intervals of 0.002, with each structure's atoms relaxed while holding the lattice vectors constant. C_{ij} was determined by linear regression on the stress *vs.* strain. Elastic parameters for pristine structures using different functionals are listed in Table 5.1, demonstrating good agreement for LDA and PBE+GD2 with experiment.

Strain directions 3 and 5 were chosen for their relevance to sliding and wear. Shearing strains in the 4- and 5-directions are the motions involved in basal plane sliding. Uniaxial 3-strain is involved in layer separation, leading to wear. By symmetry, $C_{11} = C_{22}$ and $C_{44} = C_{55}$ in pristine MoS_2, and these relations still approximately hold in our doped structures.

5.3.3 Formation Energy

Formation energies, E_{form}, can be used to gauge the relative stability of a structure versus a reference [83, 70], and are defined as:

$$E_{\text{form}} = E_{\text{mixed}} - \sum_i N_i \mu_i \tag{5.1}$$

E_{mixed} is the energy of the material of interest, μ_i is the chemical potential of the bulk element i, and N_i is the number of atoms of element i in the mixed system. μ_i must be less than the bulk element's energy per atom for the formation of the material of interest to be thermodynamically favored compared to its bulk elements, E_i. For this reason, it is useful to write Eqn. 5.1 instead using $\Delta\mu \equiv$

$\mu_i - E_i$, so

$$E_{\text{form}} = E_{\text{mixed}} - \sum_i N_i(\Delta\mu_i + E_i). \tag{5.2}$$

Formation energies were all referenced against the most stable bulk elemental compounds: Fm$\bar{3}$m (fcc) Ni, Im$\bar{3}$m (bcc) Mo, and P2_1 S. S is a particularly difficult element to handle, given its natural state is 8-membered rings. This S structure was chosen as it has been used in other literature [145, 36] and had the lowest calculated energy per atom among an isolated S atom, S_2 molecule, an isolated 8-membered ring, and an arrangement of 4 8-membered rings per cell. The reference elemental structures are metals in the case of Ni and Mo while the structures of interest are mostly semiconducting. This leads to the required use of smearing on the electronic states of some of the structures. Furthermore, some structures have significant Van der Waals interactions while others do not. These differences motivate LDA for direct comparison of formation energies rather than PBE or PBE + GD2. Formation energies are shown in Table 5.8.

Using Eqn. 5.2, we can compare the formation energies of doped structures to construct zones of chemical potentials that favor the formation of one structure over another at a given supercell size as in Fig. 5.3. To find these regions, we need to solve for when $E_{\text{form}}(\Delta\mu_{\text{Ni}}, \Delta\mu_{\text{Mo}}, \Delta\mu_{\text{S}})$ of one structure is smaller than another. Since each computation only contains one Ni atom per supercell, we can remove the dependence of $\Delta\mu_{\text{Ni}}$, leaving us with zones as a function of only $\Delta\mu_{\text{Mo}}$ and $\Delta\mu_{\text{S}}$.

We represent phase stability using the concept of the convex hull [126] which we compute using `Mathematica` [206]. Considering the closed system ($\Delta\mu = 0$) at zero temperature and pressure, we can use the formation energies to construct the convex hull as the smallest convex set containing the points (x_{Ni}, x_{Mo}, x_{S}, $E_{\text{form}}/N_{\text{atoms}}$), where $x_i = N_i/(N_{\text{atoms}})$ [126]. Since $\Sigma_i x_i = 1$, we can represent the three x_i dimensions as three legs of the two-dimensional triangle, as in Fig. 5.4. The $E_{\text{form}}/N_{\text{atoms}}$ axis is out of the page, but we can further simplify this representation by owing only the lines connecting points on the convex hull. Stable structures will be on the convex hull's boundary. Any structure whose computed

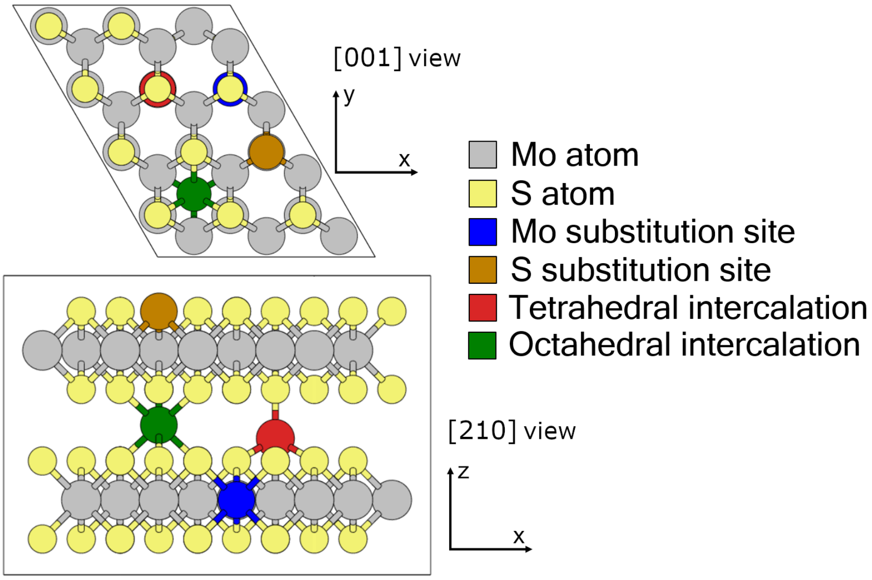

Figure 5.1: Possible sites for Ni dopants in 2H-MoS_2: Mo or S substitution, or intercalation at tetrahedral (t) and octahedral (o) interlayer sites. Other highly symmetric sites (bridge and intralayer interstitials) were found to be unstable.

energy is above the convex hull is favored to phase-segregate to the structures at the nearest nodes. The energies above hull are listed in Table 5.2 for LDA and PBE+GD2 in Table 5.7. One-dimensional convex hull diagrams with reference structures that are not bulk elemental phases are shown in Fig. 5.9.

5.4 Results and Discussion

5.4.1 Dopant sites

We consider a set of possible dopant sites shown in Fig. 5.1: Mo substitution, S substitution, octahedral (o-) intercalation, and tetrahedral (t-) intercalation, as studied for Nb-doped MoS_2 [70]. Other possible sites included the bridge site above an Mo-S bond and in between two layers, and the hollow-site interstitial directly between three S atoms on the S plane. These were ruled out as possibilities because they were found to be unstable under relaxations—they both relaxed to o-intercalation.

We consider doping of the most common MoS_2 structure: 2H, belonging to the

Table 5.1: Comparison of lattice parameters, vibrational frequencies at $q = 0$, and elastic parameters of pristine MoS_2.

	This Work			Literature		
	LDA	**PBE**	**PBE + GD2**	**Exp't**	**LDA**	**PBE + vdW**†
a (Å)	3.12	3.18	3.19	3.16 [203]	3.13 [118]	3.16 [215]
c/a	3.87	4.64	3.89	3.89 [203]	3.89 [118]	3.89 [215]
$E^1_{2\mathrm{g}}$ (cm^{-1})	389	373	371	383 [108]	388 [118]	372 [32]
$A_{1\mathrm{g}}$ (cm^{-1})	413	402	403	409 [108]	412 [118]	397 [32]
$E_{1\mathrm{u}}$ (cm^{-1})	390	373	372	384 [108]	391 [118]	372 [32]
$A_{2\mathrm{u}}$ (cm^{-1})	471	458	457	470 [108]	469 [118]	454 [32]
C_{11} (GPa)	242	181	212	238 [42]	240 [182]	223 [215]
C_{33} (GPa)	53	1.70*	51	52 [42]	53 [182]	49 [215]
C_{55} (GPa)	20	0.76*	15	19 [42]	32 [182]	15 [215]

a is in Å, mode frequencies are in cm^{-1}. *PBE without Van der Waals underestimates the elasticity in the z-direction. †Ref. [32] seems to use Tkatchenko-Scheffler [181] dispersion corrections while Ref. [215] uses Grimme-D3 [54].

D_{6h} point group with 6 atoms per unit cell, which is very close in energy to the 3R bulk phase [28]. Introducing Ni lowers symmetry: Mo substitution, S substitution, o-, and t-intercalation structures belong to the D_{3h}, C_{3v}, D_{3d}, and C_{3v} point groups respectively. We considered doped structures of increasing MoS_2 supercell size in-plane from 1×1 to 4×4, each with 1 Ni atom per cell, with Ni concentrations of 16.7 at%, 4.2 at%, 1.9 at%, and 1.0 at%. Decreasing Ni concentration allows us to extrapolate quantities to the low-doping limit.

Van der Waals interactions are important between MoS_2 layers, but they are a challenge for DFT calculations. Since such interactions are almost absent in PBE, we considered PBE with and without Grimme-D2 (GD2) [53] Van der Waals corrections. We found Grimme-D3 [54] to give very similar structures to GD2. However, GD2 and related approaches are particularly poor for metals [3]. This is not an issue for MoS_2, but it is problematic for computing formation energies with reference to pure Ni and Mo. By contrast, LDA is quite accurate for metals, and also successful for Van der Waals-bonded quasi-2D systems: empirically, it is seen that LDA's overestimation of interatomic interactions balances the lack of explicit non-local Van der Waals interactions [217]. Therefore we focus on LDA for formation energies such as in Table 5.2.

We also find that LDA provides better agreement with experimental vibrational frequencies than PBE or PBE+GD2. (Table 5.1)

With these considerations, we have chosen to use LDA calculations for energies in the phase diagrams, convex hull, and vibrational calculations. As shown by Peelaers and Van de Walle, adding dispersion corrections to PBE can give reasonable structures and elastic properties; [136, 137] we confirm this in Table 5.1. PBE+GD2 was thus used for structural parameters, elastic parameters, and electronic densities. PBE with no correction was found to be quantitatively worse than LDA and is not used except as a point of comparison: the energy landscape is very flat with respect to changes in layer separation, leading to large errors in the lattice parameter c and the C_{33} and C_{55} parameters.

We calculated formation energy for pristine and doped MoS_2, as well as other crystals containing Mo, S, and/or Ni. We used the Materials Project [73] to find materials with relatively stable computed energies (less than 0.1 eV/atom above hull): Ni_2Mo, Ni_3Mo, Ni_4Mo, NiS_2, Ni_3S_4, NiS, Ni_9S_8, Ni_3S_2, MoS_2, and Mo_3S_4, and the Chevrel phase $NiMo_3S_4$. $NiMo_3S_4$ [59] appears to be the only known stochiometric crystal that contains all three species. It could be a competing material during the synthesis of Ni-doped MoS_2, and has been studied for catalysis of the hydrogen evolution reaction [196].

5.4.2 Bonding

The electron density can be a useful tool to study bonding. The pristine unit cell and doped 2×2 supercell electron densities are shown in Fig. 5.2. The maximum electron density in the Ni-S or Ni-Mo bonding regions is similar to that of the pristine Mo-S bonds, signifying the Ni bonds are strong and covalent in all cases. The maxima are slightly less than for Mo-S bonds in each case, except they are

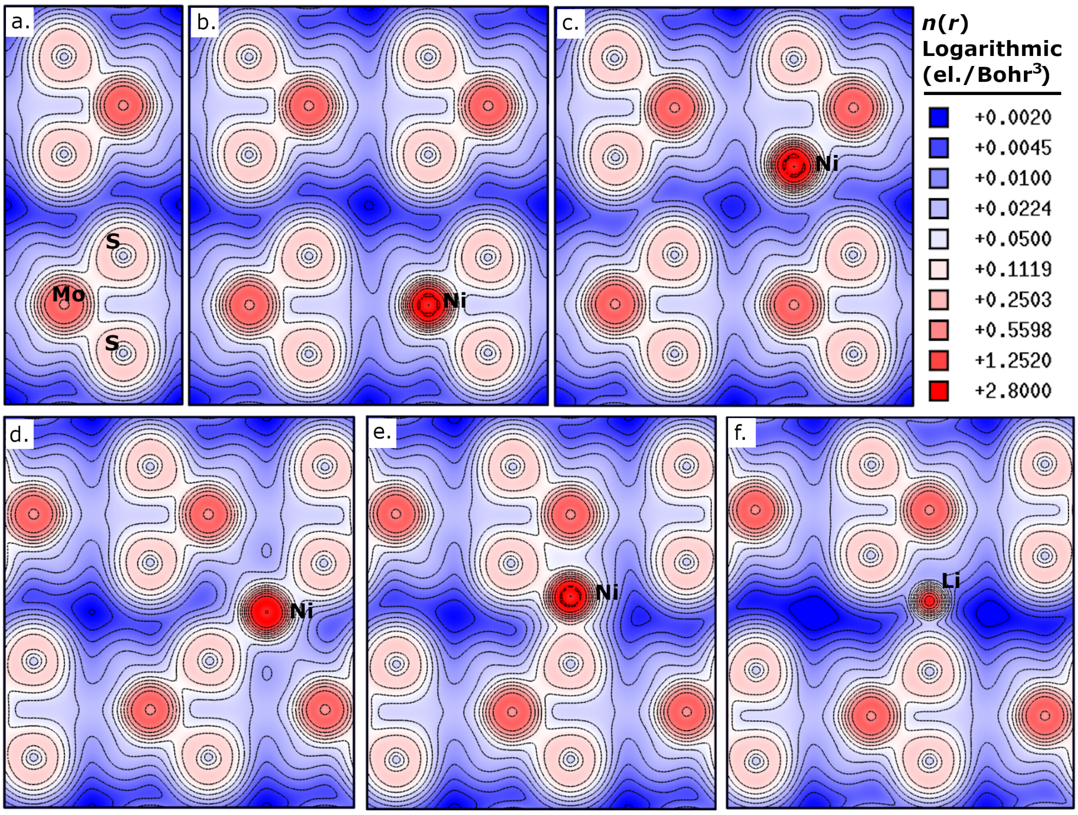

Figure 5.2: Cross sections of the electron densities of a) pristine MoS_2, b) Ni substituting Mo, c) Ni substituting S, d) Ni o-intercalation, e) Ni t-intercalation, and f) Li t-intercalation within 2×2 supercells. The data is displayed in a logarithmic color scale in the xz-plane which includes Mo-S and Ni bonds. In intercalated structures, the electron density has strongly increased in the interatomic region between layers. This suggests formation of covalent bonds for intercalated Ni, unlike in the well-known case of Li [38]. Densities were plotted using XCrysDen [88].

higher for the Ni-S interlayer bonds of t-intercalation. The surprising result that Ni can readily substitute S with the bonding network intact indicates that Ni, like Co [131], could potentially be used to fill S vacancies in a stable structure. Results from formation energies with respect to vacancies, however, show that filling an S vacancy with Ni requires energy while filling a Mo vacancy with Ni releases energy (Table 5.10).

The o- and t-intercalated structures show clear layer-to-layer bonds with the Ni atom as a bridge. Li is a known MoS_2 intercalant that widens the separation between layers [38] and is stripped of its outer electron, leaving a closed-shell ion that does not form covalent bonds, as shown in Fig. 5.2f. Comparing the Li case to Ni shows a stark contrast in the electron density, indicating that Ni forms strong covalent interlayer bonds as opposed to Van der Waals or ionic interactions for Li. The interlayer density is unchanged from the pristine in the Mo-substituted case but has increased significantly in the case of S substitution, indicating increased interlayer interactions.

We find a small reduction in the c-parameter for Mo substitution, as well as for S substitution and o-intercalation, especially at high concentration, which is consistent with Mosconi *et al.*'s report that Ni doping results in reduction of the c-parameter and is attributed to Mo substitution and Ni's smaller covalent radius [120]. The basal lattice parameter a/b is essentially unchanged, however, regardless of concentration. 3×3 and 4×4 supercells of Mo-substituted and o-intercalation structures show a pseudo-Jahn-Teller symmetry-breaking in their Ni-S bond lengths. When Ni substitutes Mo, four Ni-S bonds are 2.2 Å long (2 bonds to each of the S planes), an additional bond is slightly longer by 0.2 Å and the final S atom has been pushed away significantly to a distance of 3.3 Å. A similar symmetry-breaking has been calculated for Mo substitution on the basal plane [60]. A fully symmetric o-intercalation structure is possible, unlike the t-intercalation which automatically breaks symmetry between layers. Despite this, o-intercalation breaks symmetry: Ni-S bonding distances in the closer layer are 0.2 Å shorter than those in the further layer. A full concentration dependent set of atomic distances and cell parameters can be found in Table 5.6.

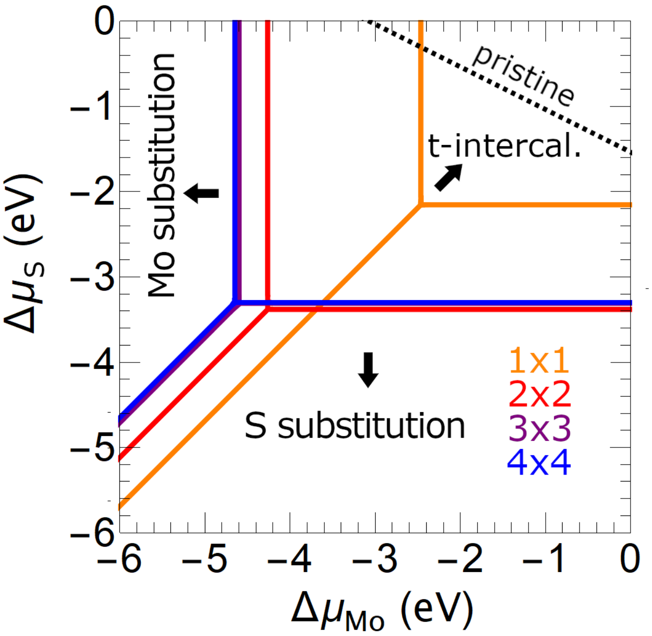

Figure 5.3: Thermodynamically favored doped structures at different chemical potentials relative to bulk phases, as calculated by LDA. The equilibrium lines change depending on the concentration, but do not change much between LDA, PBE, and PBE+GD2. The dashed line indicates the boundary above which MoS_2 is stable. Phase diagrams for PBE and PBE+GD2 can be found in Fig. 5.8.

5.4.3 Phase Stability

Since the different doped structures have different stoichiometries, we compare their thermodynamic favorability using not only formation energies but also the chemical potentials of the elements with respect to their bulk phases. The favored structures as a function of chemical potentials are shown in Fig. 5.3. We focus on the region with $\Delta\mu_{\mathrm{S}} le0$ and $\Delta\mu_{\mathrm{Mo}} le0$, where the bulk Mo and S would not be formed, as in stability triangle analysis [225]. With different supercell sizes, and thus concentrations, the favorable chemical potential regions shift slightly. Except for the very highly-doped 1×1 structure, the triple point rests around $\Delta\mu_{\mathrm{Mo}} = -4.0$ eV and $\Delta\mu_{\mathrm{S}} = -3.7$ eV. These values can be used to select the relative concentrations of reactants used in the synthesis process to achieve a particular target structure. The proximity of the 3×3 and 4×4 lines show that the 3×3 supercell is converged to the low-doping limit. O-intercalation structures do not

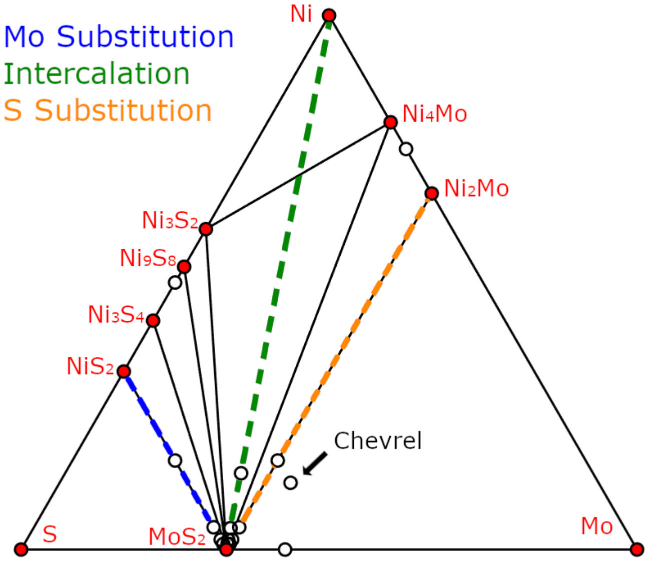

Figure 5.4: Phase diagram for materials containing Ni, Mo, and S, based on LDA energies. Materials' position along the plane edges indicate their stoichiometry. Materials on the convex hull are shown in red. Structures with energies above hull are represented as open circles; all the doped structures fall within this category and are mostly clustered around the MoS_2 point. The t-intercalation is above but very close to the convex hull.

Table 5.2: Energies per atom above hull in eV, according to LDA, for computed solids containing Mo, S, and/or Ni.

Mo	0	Ni_3Mo	0.024	NiS	0.018	MoS_2	0
Ni	0	Ni_4Mo	0	Ni_3S_4	0	Mo_3S_4	0.065
S	0	NiS_2	0	Ni_9S_8	0		
Ni_2Mo	0	$NiMo_3S_4$	0.050	Ni_3S_2	0		

	Mo subst.	S subst.	t-intercal.	o-intercal.
1×1	0.149	0.173	0.025	0.116
2×2	0.107	0.090	0.002	0.044
3×3	0.054	0.039	0.001	0.021
4×4	0.031	0.022	0.001	0.012

appear on this plot because they have the same stoichiometry as t-intercalation, but always have a larger formation energy by about 0.07 eV per Ni atom. For comparison, calculations indicate o-intercalation is preferred over t-intercalation for Nb [70], Li [38], Ag [158], and Mo [227]. The stability line [225] for pristine MoS_2 is also shown in Fig. 5.3, below which any kind of MoS_2 structure is not expected. Since only the t-intercalation region (for supercells greater than 1×1) exists above this line, we conclude that equilibrium growth will yield t-intercalation, and the substituted sites can only be reached out of equilibrium. Phase diagrams for PBE and PBE+GD2 are shown in Fig. 5.8 and show a similar trend to LDA with respect to increasing supercell sizes. Formation energies *vs.* bulk Mo and S (Table 5.8) are -0.6 to -1.0 eV, but to judge favorability of doping, we must compare to MoS_2. Previous studies [36] have focused on the end-points of this pristine stability line: where $\Delta\mu_{\mathrm{S}} = 0$ ("S-rich") or $\Delta\mu_{\mathrm{Mo}} = 0$ ("Mo-rich"). We consider in both cases that $\Delta\mu_{\mathrm{Ni}} = 0$, *i.e.* "Ni-rich" as well. We find that t-intercalation is the favored structure for both ends at all supercell sizes, except for 1×1 where S-rich conditions favor Mo-substitution. The positive formation energies *vs.* MoS_2 (0.01-0.4 eV) in Table 5.9 show that doping is unfavorable generally, though t-intercalation is essentially stable with an extremely small formation energy of 0.1 meV/atom.

The convex hull is used to identify structures that are stable against phase segregation [72, 94]. Our calculation (Fig. 5.4) shows that neither the Chevrel nor the doped compounds are the most stable structures at their concentrations. Therefore, these structures will phase-segregate into nickel sulfides, Ni-Mo alloys, and pure elements given enough time and temperature. Table 5.2, however, shows that the low-concentration doped structures have small energies above hull. The t-intercalation energies above hull, in fact, are below $k_B T$ at room temperature for all concentrations, and have magnitude within the margin of error for DFT energies. Therefore we may regard these structures as stable: synthesizable and unlikely to phase-segregate. Despite being observed at the edges of small flakes [96], Mo substitution has high energies above hull which are generally higher than for S substitution. The Chevrel phase ($NiMo_3S_4$) has an energy above hull on the order of the 3×3 Mo- and S-substituted phases—since this phase is known to be experimentally synthesizable [59], the results suggest the doped phases will also be accessible. Consideration of 1D convex hull plots along the colored lines of Fig. 5.4 shows very small energy differences above hull for t-intercalation *vs.* MoS_2 and bulk Ni, but much larger differences for Mo substitution *vs.* MoS_2 and NiS_2, or S substitution *vs.* MoS_2 and $MoNi_2$ (Fig. 5.10). Several Ni_xS_y phases are seen to be stable, consistent with observation of their forming during synthesis by Kondekar *et al.* [90] Phase diagrams for PBE and PBE+GD2 and energies above hull are given in Fig. 5.9 and Table 5.7.

5.4.4 Elasticity

We found the elastic parameters, important for tribology as the material is under stress, are altered by Ni doping as shown in Table 5.3. The in-plane C_{11} parameter is notably weakened in the case of Mo substitution. This may be related to the lower charge density between Ni and S as seen in Fig. 5.2b. At lower Ni concentrations, the reduced number of bonds leads to a lower C_{11}. S substitution also weakened C_{11} slightly, but the intercalated cases saw little change at any supercell sizes beyond 1×1. Out-of-plane C_{33} stiffness increased in the case of intercalated and S-substituted structures due to interlayer bonding with intercalated Ni, and increased interlayer interactions for S substitution. The increased out-of-plane

Table 5.3: Elastic parameters for Ni-doped structures at different supercell sizes.

(GPa)		**undoped**	**Mo subst.**	**S subst.**	**t-intercal.**	**o-intercal.**
C_{11}	1×1	211.8	159.2	168.9	201.4	208.2
	2×2	''	177.2	204.8	211.5	210.6
	3×3	''	196.5	207.7	211.1	208.7
	4×4	''	190.8	210.0	212.0	210.2
C_{33}	1×1	51.3	50.0	91.7	99.4	94.1
	2×2	''	51.3	57.7	76.1	72.9
	3×3	''	49.0	55.8	63.4	63.3
	4×4	''	50.0	54.3	57.9	58.7
C_{55}	1×1	15.1	7.5	24.3	24.0	25.3
	2×2	''	13.1	10.9	19.1	20.6
	3×3	''	13.8	14.0	16.7	12.4
	4×4	''	14.2	14.6	15.9	13.2

1×1 through 4×4 supercells correspond to Ni concentrations of 17 at%, 4 at%, 2 at%, and 1 at% respectively. Most structures did not change appreciably in C_{11} besides the 20-30 GPa drop for Mo substitution. C_{33} values were appreciably raised by 20 GPa in intercalated cases. C_{55} did not show large changes, giving evidence against the idea that Ni doping lowers the frictional coefficient by lowering the shear stiffness.

stiffness will contribute to the increased resistance to wear (layers flaking off), as seen in experiments [170, 192].

Since Ni-doping is known to reduce the coefficient of friction of MoS_2, we might expect C_{55} would be lowered, reducing the shear stiffness. However, there is not much difference between doped and undoped C_{55} values at low concentrations. Further, at high concentrations (5-15 at%) C_{55} of intercalated structures is significantly higher than the pristine case (except for Mo substitution, where it is halved). This indicates that a reduction in shear stiffness is not the explanation for the observed reduction in frictional coefficient due to Ni doping.

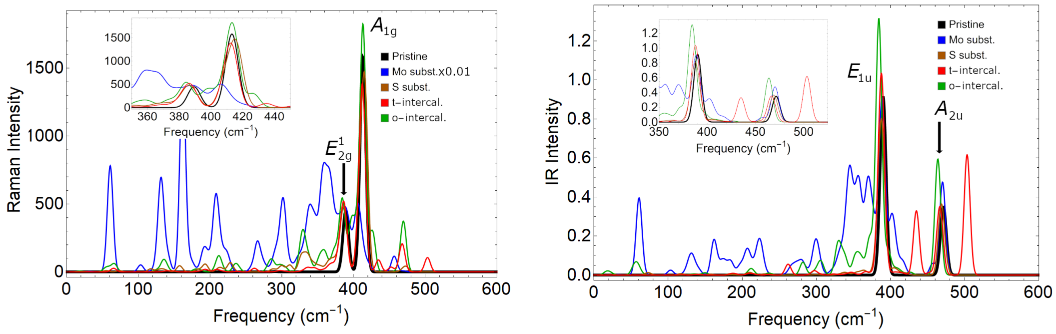

Figure 5.5: Raman and IR spectra, in A^4/amu per MoS$_2$ unit and (D/A)^2/amu per MoS$_2$ unit respectively, for 3×3 doped structures. A Gaussian broadening of 4 cm^{-1} is used. Mo-substituted Raman intensities are large, so they are scaled by a factor of 0.01. Low frequency modes (< 100 cm^{-1}) correspond to layer breathing and shearing modes. Insets more closely show the pristine Raman-active A_{1g} and E^1_{2g} modes and IR active E_{1u} and A_{2u} modes. The strong IR and Raman peaks of the pristine MoS$_2$ remain with doping but new peaks appear at different frequencies which can be used for experimental identification of the doping site.

5.4.5 Vibrational Spectroscopy

To aid in experimentally identifying Ni-doped MoS$_2$, we have computed the Raman and IR intensities for MoS$_2$ with the different doped sites. Previous experimental work [115, 171, 120, 155] of doped MoS$_2$ has focused on shifts in the A_{1g} and E^1_{2g} Raman peaks relative to the pristine positions [68], but have not investigated the formation of new peaks due to symmetry breaking and the presence of a new atom of a different mass, or symmetry breaking due to the dopant, as seen in other doped 2D materials [220, 222]. Raman and IR spectra are compared in Fig. 5.5 and key distinguishing features are listed in Table 5.4. Mode characters are detailed in Tables 5.11-5.4. We have computed the spectra for 1×1, 2×2, and 3×3 supercells to see the concentration-dependence of the strong Raman and IR active peaks and find that 3×3 is converging to a low-doping limit (Figs. 5.13 and 5.12), though significant Raman intensity variations with concentration remain for Mo substitution and o-intercalation.

As in previous studies [90, 171, 188], the doped spectra show peaks corresponding to the pristine ones, with changes in frequency. Shifts in the pristine Raman/IR peaks can be caused by a number of factors: the mass difference of Ni compared

Table 5.4: Changes to the pristine vibrational spectra for doped 3×3 structures.

Frequency ($\mathbf{cm^{-1}}$)		**Mo subst.**	**S subst.**	**t-intercal.**	**o-intercal.**
Raman	New peak	61, 131, 132, 162, 266, 301, 364	327, 333, 337	366, 372, 435, 452, 503	212, 235, 330, 361, 427
	Activation	209, 457	473	336, 465, 468	67, 135, 287, 287, 470
	$E^1_{2\mathrm{g}}$ shift	-3.2	-3.2	-3.1	-5.4
	$A_{1\mathrm{g}}$ shift	-7.1	+2.0	-0.2	-0.5
IR	New peak	61, 131, 132, 162, 301, 345, 356, 370	-	262, 435, 503	330
	Activation	209, 224, 388, 389, 470	473	465, 468	54, 59, 282, 282
	$E_{1\mathrm{u}}$ shift	-0.6	-0.8	-1.9	-6.1
	$A_{2\mathrm{u}}$ shift	-14.5	-3.0	-6.2	-7.5

to substituted Mo or S, an alteration of bond strengths by *n*- or *p*-type doping, or induced strain [84]. Ni has two more electrons than Mo and results in *n*-type doping (as discussed below), which would generally be expected to result in a redshift of the $A_{1\mathrm{g}}$ peak [68]. In Li-intercalated $\mathrm{MoS_2}$, Sekine *et al.* [155] experimentally found redshifts of the $E^1_{2\mathrm{g}}$ and $A_{1\mathrm{g}}$ Raman frequencies due to changes in the *c*-axis interactions. Table 5.4 shows that in Ni-doped $\mathrm{MoS_2}$ $A_{1\mathrm{g}}$ has small redshifts for intercalation, like Li-intercalated $\mathrm{MoS_2}$, but $A_{1\mathrm{g}}$ has a blueshift for S substitution. Dopants have generally been found to shift mostly the $A_{1\mathrm{g}}$ frequency [68], including the measurement of a shift around -1 $\mathrm{cm^{-1}}$ for $E^1_{2\mathrm{g}}$ and +3 $\mathrm{cm^{-1}}$ for $A_{1\mathrm{g}}$ in Ni-doped $\mathrm{MoS_2}$; [90] however, in our calculation we find Ni induces also strong

Table 5.5: Calculated $q = 0$ low-frequency vibrational modes in pristine and doped $\mathrm{MoS_2}$.

(cm^{-1})	**undoped**	**Mo subst.**	**S subst.**	**t-intercal.**	**o-intercal.**
Shearing-like mode frequency (pristine $E^2_{2\mathrm{g}}$)					
1×1	35	38, 43	88, 89	57, 57	48, 49
2×2	''	26, 30	24, 27	42, 43	41, 41
3×3	''	32, 34	22, 25	30, 30	17, 22
Layer breathing-like mode frequency (pristine $B^2_{2\mathrm{g}}$)					
1×1	56	88	132	127	108
2×2	''	63	58	78	71
3×3	''	59	55	66	67

shifts in the $E^1_{2\mathrm{g}}$ peak and the IR-active peaks. The different behavior observed in the experiment may be due to different (and unclear) Ni concentration and the effects of a limited number of layers, in-plane crystallite size, and/or strain [90].

Peaks unique to the doped spectra were classified as either "new" or "activations." New peaks are those that do not have counterparts in the pristine 3×3 q-grid vibrational density of states (VDOS) (Fig. 5.6) and have mode characters that cannot be easily described by pristine mode eigenvectors: they are mostly related to motions of the Ni atom and its neighbors. Activations are modes that have a counterpart in the pristine case whose IR and/or Raman activity is forbidden by symmetry. Ni doping breaks symmetries and mixes modes, which can induce IR and/or Raman activity. Raman intensities were particularly large in the case of Mo substitution owing to its metallic character, and so they are scaled down in Fig. 5.5; we expect this intensity enhancement compared to pristine can serve as a feature to identify this kind of doping. There is Raman and IR activity present in all doped structures at low frequencies (below 350 cm^{-1}), but it is most prominent in Mo-substituted and o-intercalation structures.

The modes of the doped systems show several interesting patterns in comparison to the pristine modes (Fig. 5.6). Many new modes are breathing modes of Mo and S around Ni (Fig. 5.6a), or involve Ni-S stretches (Fig. 5.6b), or feature new combinations of S motions, as in S substitution or Mo substitution. The activation

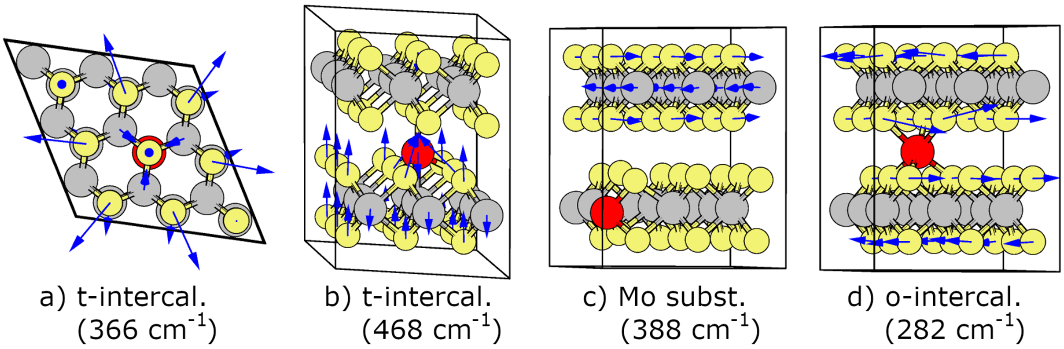

Figure 5.6: Example vibrational modes of Ni-doped MoS_2, showing four typical patterns: a) a new peak for t-intercalation consisting of an in-plane breathing mode around Ni, in only one layer; b) t-intercalation breaks symmetry between the layers, mixing the A_{2u} and B^1_{2g} modes with Ni-S stretches; c) Mo substitution breaks symmetry between layers, and mixes E^1_{2g} and E_{1u} modes, but does not involve Ni; d) o-intercalation only slightly breaks symmetry, and leaves E_{2u} modes almost unaffected.

peaks are strongly influenced by symmetry breaking between the two layers. In Mo and S substitution, only one layer has a dopant, strongly breaking symmetry; pristine modes are mixed to give modes localized on only layer (Fig. 5.6c). In t-intercalation, the layer symmetry is broken because Ni has 3 bonds to one layer and 1 to the other, and so the activations involve Mo/S motion in only one layer. For o-intercalation, a perfectly symmetrical structure is possible, but in fact Ni moves slightly closer to one layer, making only a small symmetry breaking: most activated modes (Fig. 5.6d) are still on both layers, look identical to pristine, and are shifted typically less than 10 cm^{-1} from the pristine frequencies. Most of the new peaks also show these same layer localization patterns.

Kondekar *et al.* [90] find a Raman peak related to Ni-doping at 290 cm^{-1}. This peak seems a sign of Mo-substitution, corresponding to our calculated new peak at 300 cm^{-1}, which is related to S vibration in the doped layer, out-of-phase between the two S planes. This peak appears for both 2×2 and 3×3 supercells and should be detectable given the high Raman intensity. A less likely possibility (due to lower intensity, and unfavorable energetics) is the o-intercalation, which has a peak at 287 cm^{-1} related to the pristine E_{1g} (low Raman activity) and E_{2u} (Raman-inactive) modes. With higher-resolution Raman spectroscopy, we expect that additional peaks could be discerned and solidify the identification.

A few low frequency modes are particularly relevant to tribology: the shearing mode (E^2_{2g} in pristine), relating to frictional sliding, and the layer breathing mode (B^2_{2g} in pristine), relating to layer dissociation and wear. Our calculated values for the doped structures are listed in Table 5.5. The increase in the layer breathing frequency in intercalated structures correlates with the stiffening of C_{33} in those structures. This increase is contrary to the decreased frequencies observed in Ag-doped MoS_2 [158]. Substituted breathing mode frequencies are largely unaffected. The doubly degenerate shearing mode was split in the doped structures, and reduced in frequency for low doping concentration similar to Ag-doped MoS_2 [158], particularly in S substitution and o-intercalation. At high doping concentrations, both shearing and breathing frequencies are increased.

Raman intensities are related to EPC and have been suggested as a probe of EPC in 2D materials [106]. In our systems, only Mo substitution shows substantial changes in intensities, whereas other sites stay within 10% of the pristine peak intensity. If the argument by Lin *et al.* [106] applies, Mo substitution's large Raman intensity would mean increased EPC and thus increased friction. This means that the observed reduction in friction [170, 192] of Ni-doped MoS_2 is either not attributable to changes in EPC or samples were not dominated by substitution of the Mo site.

5.4.6 Electronic density of states

To assess n-type or p-type doping and other changes in electronic structure, we calculate the electronic density of states (DOS), shown in Fig. 5.7. Low concentrations of S-substituted structures show defect states near the conduction band maximum (CBM) while o-intercalation creates defect states above the valence band maximum (VBM). All doped structures show some degree of bandgap closing. Mo-substituted structures have metallic character, with the Fermi level situated in the new in-gap states meaning it is slightly p-type. S substitution shows new states near both band edges, while o-intercalation has new states near the valence band and an extended conduction band tail. The t-intercalation shows the least modifi-

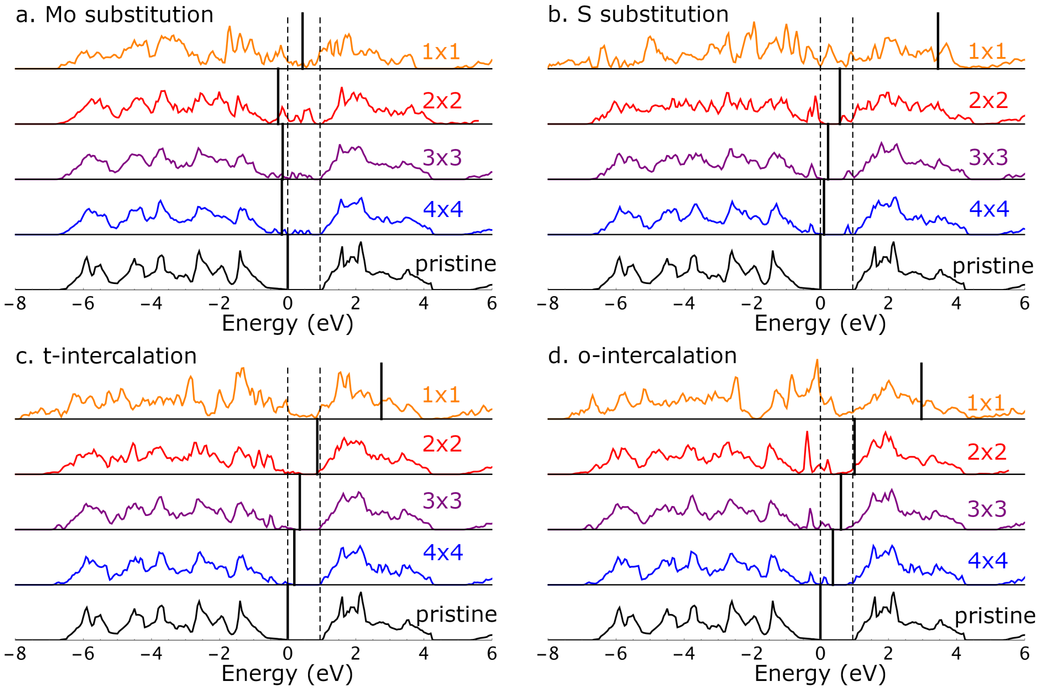

Figure 5.7: Electronic density of states (DOS) for doped structures (color) and pristine DOS (black). The CBM and VBM of pristine MoS_2 are shown as vertical dashed lines. Doped DOS were aligned with the low-lying Mo 4*s* state (36 eV below VBM) of the pristine plot. Calculated Fermi energies or VBM are shown as solid-black vertical lines.

cation from the pristine DOS, with only a slight narrowing of the gap due to new states in the valence band.

The Fermi level for low doping concentration is near the pristine VBM. Alterations are more dramatic at high concentrations where the Fermi level is pushed well within the pristine conduction band in all cases except Mo substitution. This can be understood as n-type doping at high concentration. Naturally occurring MoS_2 is typically n-type due to Re impurities [89]. Provided nickel sulfides do not form [90], high Mo-substitution doping concentrations could create p-doped MoS_2, which has been challenging to achieve [188].

In general, our calculations indicate an increased conductivity of Ni-doped MoS_2, either through in-gap states, a narrowed bandgap, or n- or p-type electronic doping, depending on the doping site. These results are consistent with enhanced catalytic activity of Ni-doped MoS_2, and early calculations attributing enhancement in Mo-substituted MoS_2 to electron donation from Ni to Mo [52].

5.5 Conclusion

Through *ab initio* methods, we have computed the structure, stability, and vibrational spectra of bulk Ni-doped 2H-MoS_2, which has not been previously explored. We found four metastable dopant sites: Mo substitution, S substitution, octahedral intercalation, and tetrahedral intercalation (always favored energetically over octahedral). Ni in the Mo-substituted structure has only five bonds just as in a basal plane surface [60], and thus is elastically weaker in-plane. The C_{55} shear-stiffness parameter is strengthened by doping, suggesting this is not the explanation for the reduced friction observed [170] in Ni-doped MoS_2. Ni-S bonding is comparable to pristine Mo-S bonding, and the fact that Ni-Mo bonds are comparable to Mo-S bonds in S substitution are particularly surprising—this suggests that Ni, like Co [131], can fill existing S vacancies as a way to synthesize S-substituted MoS_2.

We find that all doped structures are above the convex hull, but t-intercalation is very close to it. It therefore can be considered thermodynamically stable, with essentially zero formation energy from Ni and MoS_2, and is not likely to phase-segregate, unlike the other doped structures. The other sites' energies above hull are lower than that of the known Chevrel phase $NiMo_3S_4$, suggesting these are synthesizable as well. Phase diagrams show how the chemical potentials of Mo and S can be tuned in synthesis to favor Mo substitution, S substitution, or t-intercalation, though only t-intercalation can co-exist with pristine MoS_2. Intercalated Ni forms strong covalent bonds between layers, unlike intercalated Li. This increases elastic parameters out of plane, and results in little change to the c-parameter, contrary to what is sometimes assumed. Strong interlayer bonding poses a possible explanation for the observed resistance to wear [170, 192].

n-type doping is prominent at high Ni concentration. Mo-substituted structures become metallic due to in-gap states, which leads to a large enhancement of Raman intensities. New peaks in the Raman spectra appear due to vibrations of Ni and its neighbors, while activations and shifts in existing modes are caused by breaking symmetry and altering bond strengths. While generally doping has been found primarily to affect the A_{1g} mode, we find shifts of all four IR- and Raman-active peaks. The distinctive effects on the Raman and IR spectra can be used experimentally to identify the doping sites in Ni-doped samples. We propose a new paradigm for identification of MoS_2 dopant locations by vibrational spectroscopy, as these structures have remained unclear experimentally.

The structures found in this work are being used to probe macroscopic tribological properties related to wear and friction through parametrization of ReaxFF reactive force fields in Ch. 7 for classical molecular dynamics and calculations of sliding potentials [105]. We are additionally extending this work to study Ni-doping in 3R bulk and 1H and 1T monolayer polytypes of MoS_2 [81, 80] to determine the impact of the phase on doping effects.

5.6 Supplementary Material

Convex hull plots used the function `ConvexHullMesh` in `Mathematica v12.1` [206]. In some cases, the computed convex hull was incorrectly computed by

`Mathematica` to not encompass points that are very close to the convex hull faces. We found that including extra arbitrary points far above the hull in energy resolved this issue.

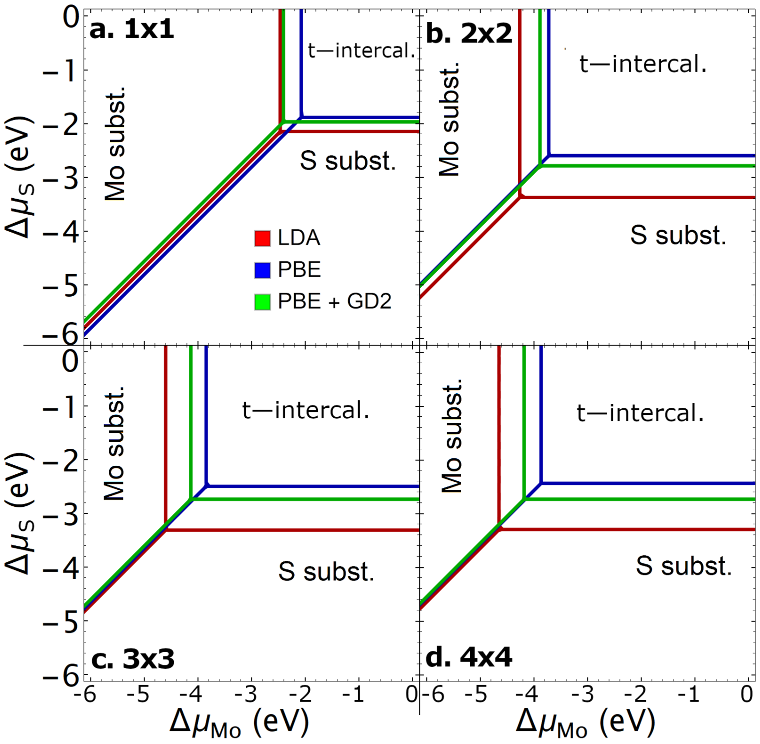

Figure 5.8: Phase diagrams for LDA, PBE, and PBE + GD2 are computed. The difference between functionals is similar across sizes, with LDA triple points residing at further negative $\Delta\mu_{\mathrm{S}}$ and $\Delta\mu_{\mathrm{Mo}}$ than PBE. There is little difference between the 3×3 and 4×4 diagrams, indicating the plot is converged with respect to Ni concentration.

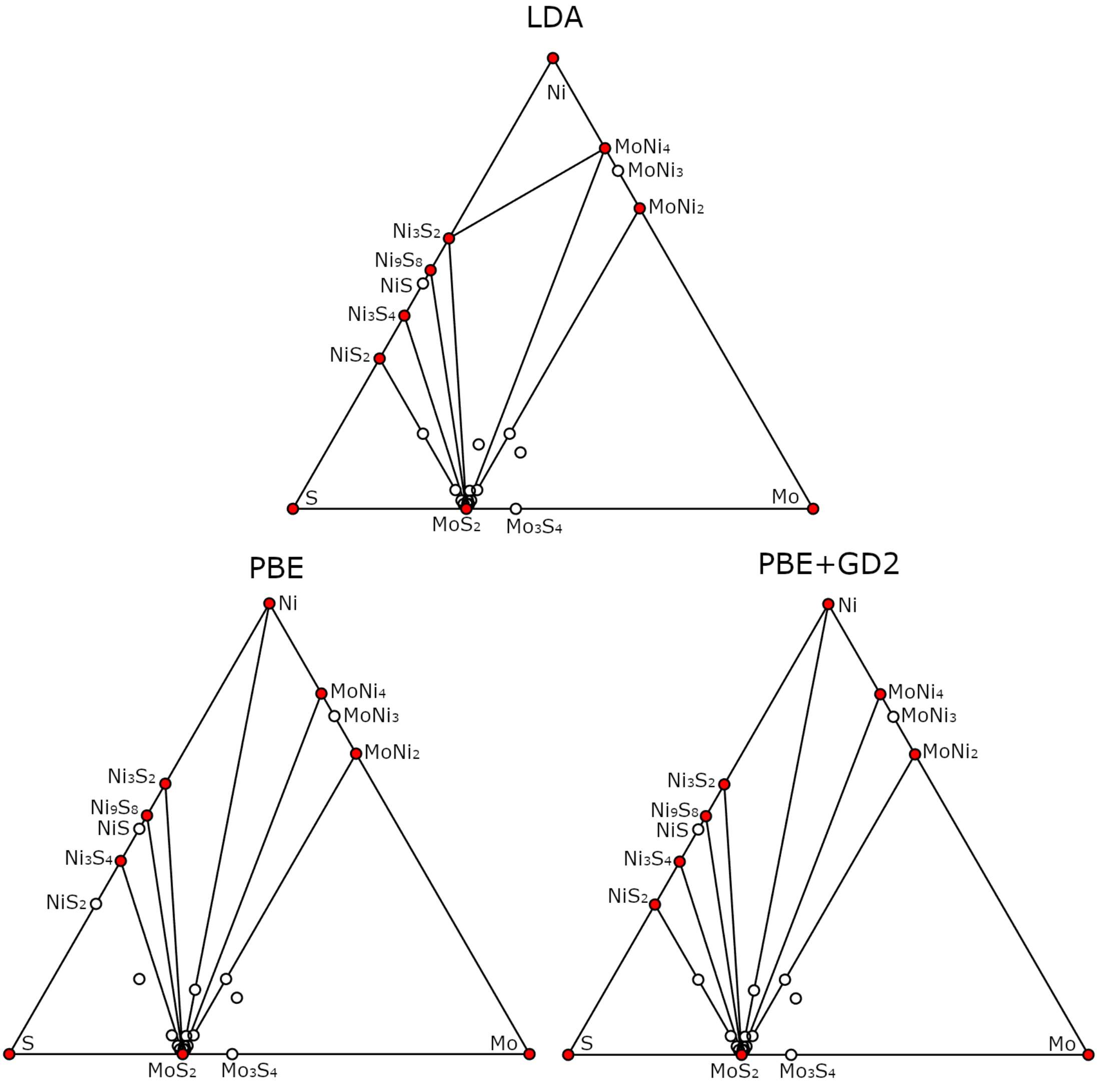

Figure 5.9: Convex hull diagrams for LDA, PBE, and PBE + GD2. Although the relative energy differences between these three comparisons are small, qualitative changes to the convex hull are substantial. Red filled-in circles represent structures which are on the convex hull line and are thus the most stable structures at $T = 0$ K. The line between MoS_2 and NiS_2 (which contains the Mo-substituted structures) is on the convex hull when using LDA and PBE+GD2, but not for PBE alone. The line between MoS_2 and Ni is not on the convex hull in LDA. Intercalated structures are above the convex hull edge in energy.

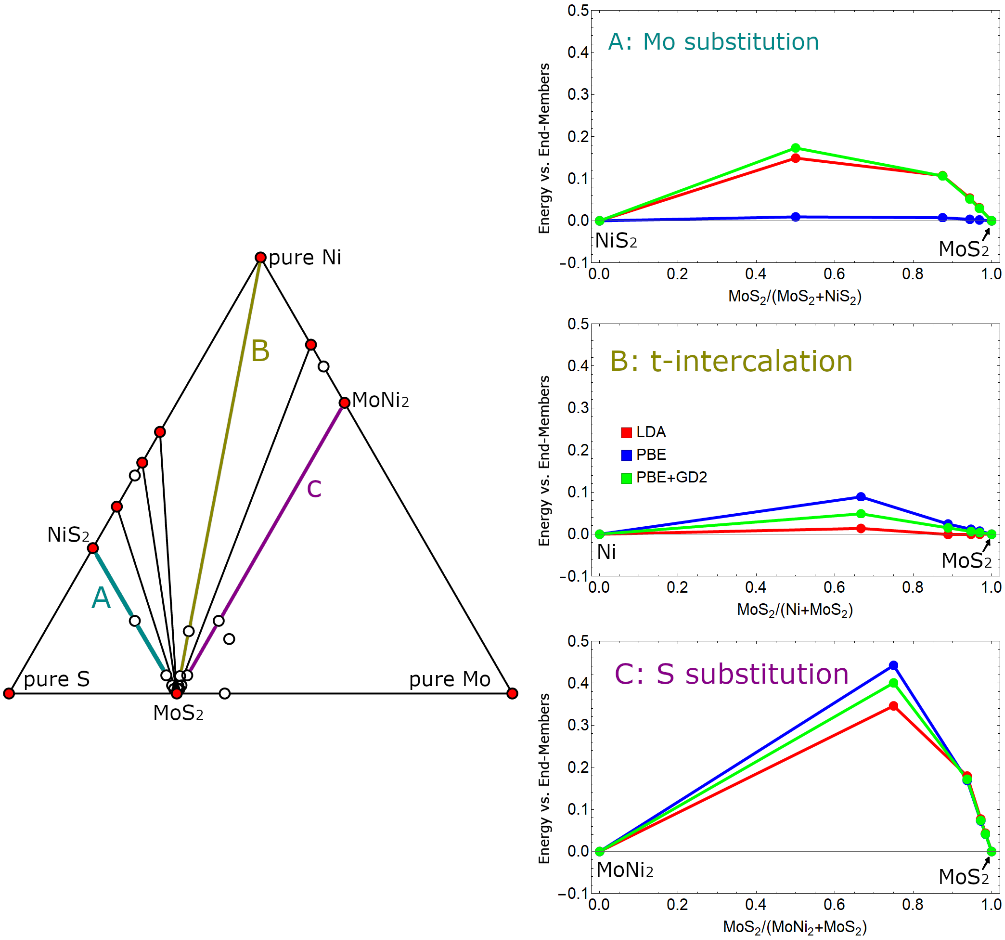

Figure 5.10: 1D convex hull diagrams from MoS_2 to: NiS_2 (Mo substitution, A), pure Ni (intercalation, B), and $MoNi_2$ (S substitution, C). The x-axis (energy $=$ 0) is always below the calculated structures, so it always constitutes the convex hull. These 1D convex hull diagrams (with energy in eV per atom) are comparable to previous literature on V, Te, and Mo ternary 2D alloys [94]. PBE behaves differently along the Mo substitution line, but overall the results are similar for the different functionals. T-intercalated energies are close to the convex hull line.

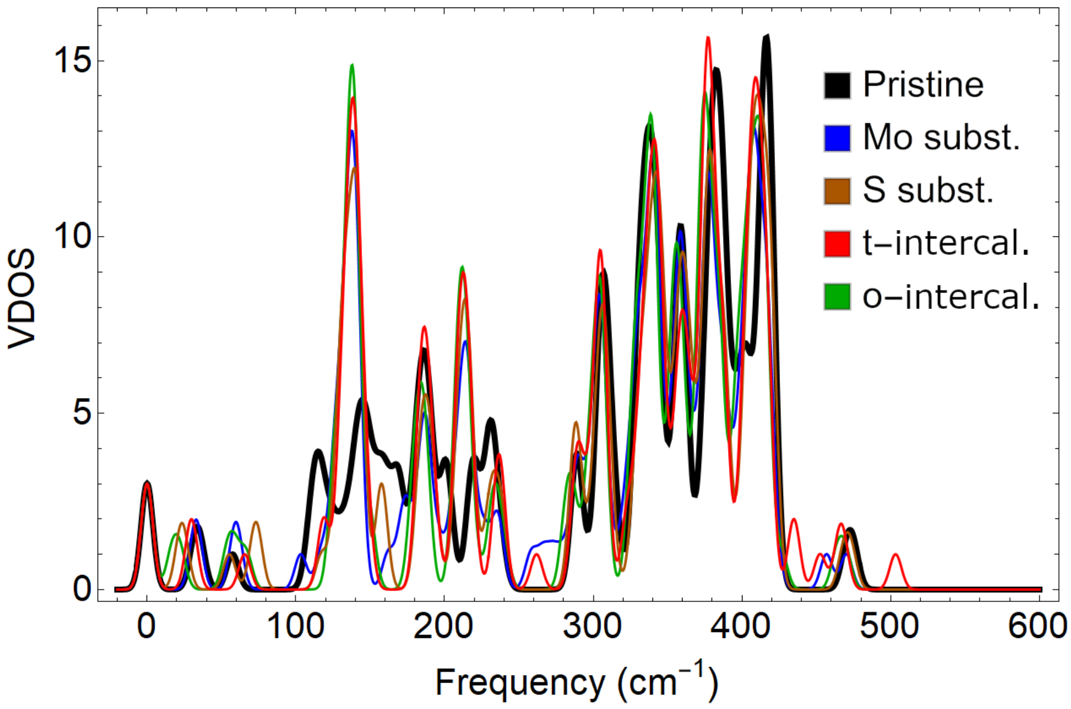

Figure 5.11: Vibrational density of states (VDOS) for doped structures using Gaussian broadening of 4 cm^{-1}. Doped structures are 3×3 supercells computed at $q = \Gamma$. The pristine case is a primitive cell calculated on a corresponding 3×3×1 q-grid. This data can be used to identify the origin of Raman/IR peaks in doped MoS_2.

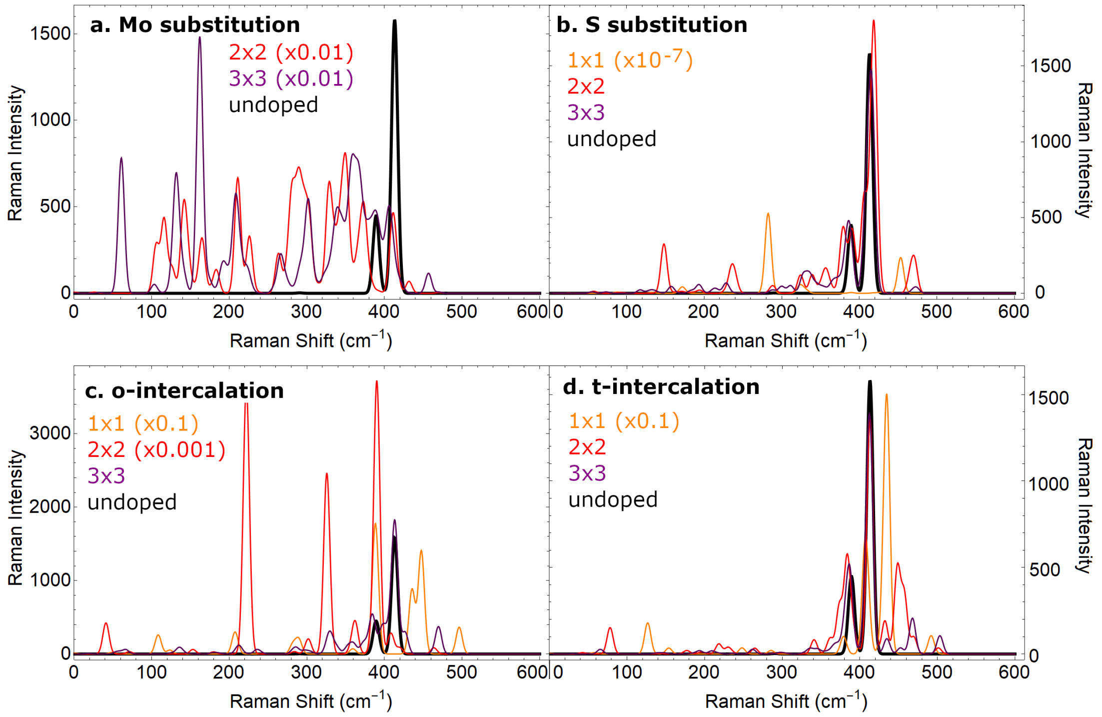

Figure 5.12: Raman spectra, in A^4/amu per MoS_2 unit, for types of doping as a function of supercell size. Gaussian broadening of 4 cm^{-1} was used. Some spectra were too intense to fit in the plot, so they were scaled by the factor in the legend. 1×1 Mo substitution was metallic and so the dielectric calculation could not be done by DFPT.

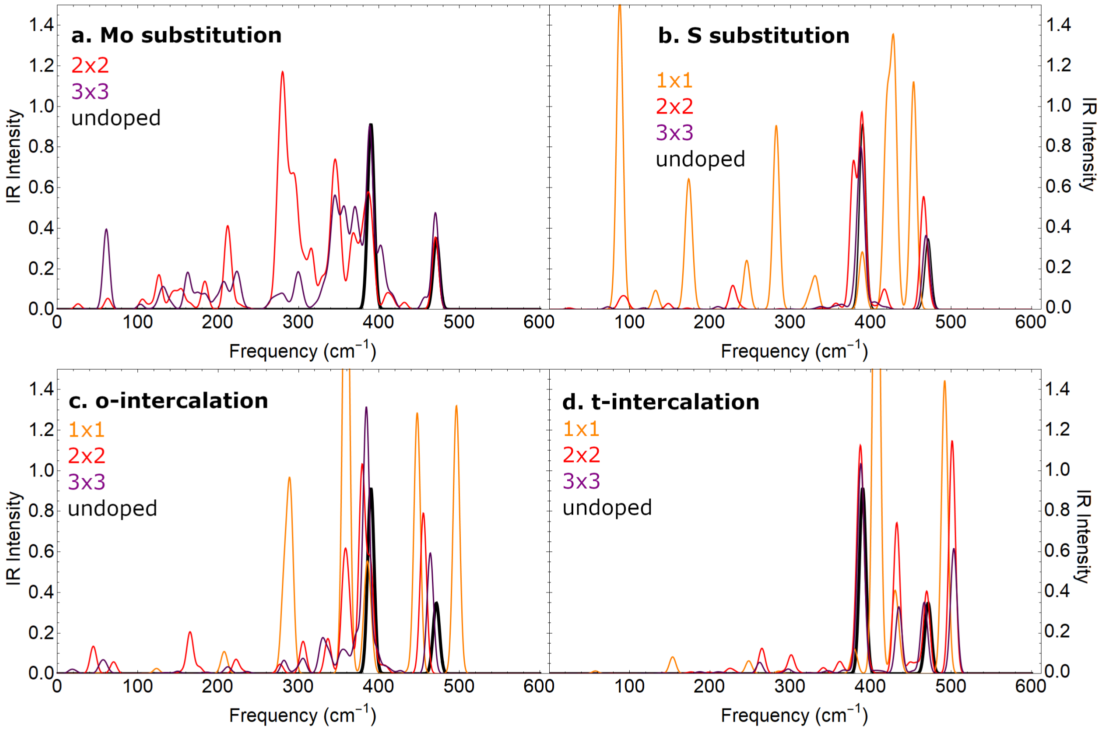

Figure 5.13: IR spectra in $(D/A)^2$/amu per MoS_2 unit for types of doping as a function of supercell size. Gaussian broadening of 4 cm^{-1} was used.

Table 5.6: Structural parameters of computed Ni-Doped MoS_2 as computed by PBE + GD2.

(Å)		**w/o Ni**	**Ni@Mo**	**Ni@S**	**Ni@t**	**Ni@o**
a	1 × 1	3.19	3.30	3.19	3.22	3.18
	2 × 2	"	3.20	3.18	3.20	3.19
	3 × 3	"	3.19	3.18	3.19	3.19
	4 × 4	"	3.20	3.19	3.19	3.19
c	1 × 1	12.4	11.3	10.8	12.6	12.5
	2 × 2	"	12.3	12.3	12.5	12.4
	3 × 3	"	12.4	12.3	12.5	12.4
	4 × 4	"	12.4	12.4	12.5	12.4
Ni-S distances (Å) below 3.1 Å						
	1 × 1		2.23 × 6	2.16 × 3	2.15 × 1, 2.18 × 3	2.38 × 2, 2.39 × 4
	2 × 2		2.37 × 4, 2.38 × 2		2.12 × 1, 2.17 × 3	2.36 × 4, 2.37 × 2
	3 × 3		2.23 × 2, 2.25 × 2, 2.39 × 1		2.12 × 1, 2.17 × 3	2.28 × 2, 2.29 × 1, 2.45 × 1, 2.48 × 2
	4 × 4		2.22 × 2, 2.24 × 2, 2.42 × 1		2.11 × 1, 2.17 × 3	2.26 × 1, 2.27 × 2, 2.50 × 3
Ni-Mo distances (Å) below 3.1 Å						
	1 × 1			2.68 × 3, 2.78 × 1	2.76 × 1	
	2 × 2			2.55 × 3	2.61 × 1	
	3 × 3		2.80 × 1, 2.82 × 1	2.56 × 3	2.59 × 1	
	4 × 4		2.80 × 2	2.56 × 3	2.59 × 1	

a parameters (Å) are the average over the primitive cells in the supercell. Ni-S and Ni-Mo distances below 3.1 Å are shown multiplied by how many equal distances there are in a given structure, *i.e.* 2.23 × 6 means six bonds with a length of 2.23 Å.

Table 5.7: Energies above hull (eV/atom) for computed structures with PBE + GD2.

Formula	LDA	PBE	PBE + GD2
Mo	0	0	0
Ni	0	0	0
S	0	0	0
MoS_2	0	0	0
Mo_3S_4	0.065	0.074	0.124
Ni_2Mo	0	0	0
Ni_3Mo	0.024	0.016	0.013
Ni_4Mo	0	0	0
NiS_2	0	0.021	0
Ni_3S_4	0	0	0
NiS	0.018	0.022	0.014
Ni_9S_8	0	0	0
Ni_3S_2	0	0	0
$NiMo_3S_4$	0.050	0.097	0.117

Dopant Site	Supercell Size	LDA	PBE	PBE + GD2
Mo subs.	1 × 1	0.149	0.136	0.173
	2 × 2	0.107	0.102	0.107
	3 × 3	0.054	0.049	0.052
	4 × 4	0.031	0.281	0.030
S subs.	1 × 1	0.173	0.221	0.200
	2 × 2	0.090	0.084	0.086
	3 × 3	0.039	0.036	0.037
	4 × 4	0.022	0.021	0.021
t-intercal.	1 × 1	0.025	0.089	0.049
	2 × 2	0.002	0.024	0.015
	3 × 3	0.001	0.012	0.007
	4 × 4	0.001	0.007	0.004
o-intercal.	1 × 1	0.116	0.219	0.167
	2 × 2	0.044	0.062	0.049
	3 × 3	0.021	0.012	0.023
	4 × 4	0.012	0.018	0.013

Table 5.8: Formation energies (eV/atom) with respect to bulk elemental phases for $\Delta\mu_{\mathrm{S}} = 0$, $\Delta\mu_{\mathrm{Mo}} = 0$, $\Delta\mu_{\mathrm{Ni}} = 0$.

Formula	LDA	PBE	PBE + GD2
Mo	0	0	0
Ni	0	0	0
S	0	0	0
MoS_2	-1.023	-0.890	-0.872
Mo_3S_4	-0.812	-0.689	-0.623
Ni_2Mo	-0.203	-0.112	-0.109
Ni_3Mo	-0.160	-0.078	-0.079
Ni_4Mo	-0.174	-0.082	-0.082
NiS_2	-0.461	-0.249	-0.292
Ni_3S_4	-0.549	-0.347	-0.367
NiS	-0.538	-0.342	-0.360
Ni_9S_8	-0.559	-0.370	-0.376
Ni_3S_2	-0.520	-0.332	-0.335
$NiMo_3S_4$	-0.755	-0.591	-0.557

Dopant Site	Supercell Size	LDA	PBE	PBE + GD2
Mo subs.	1 × 1	-0.593	-0.444	-0.409
	2 × 2	-0.846	-0.710	-0.693
	3 × 3	-0.938	-0.807	-0.788
	4 × 4	-0.975	-0.843	-0.824
S subs.	1 × 1	-0.645	-0.475	-0.481
	2 × 2	-0.883	-0.757	-0.738
	3 × 3	-0.962	-0.832	-0.814
	4 × 4	-0.989	-0.858	-0.839
t-intercal.	1 × 1	-0.861	-0.677	-0.694
	2 × 2	-0.982	-0.831	-0.820
	3 × 3	-1.005	-0.862	-0.849
	4 × 4	-1.013	-0.874	-0.859
o-intercal.	1 × 1	-0.769	-0.547	-0.575
	2 × 2	-0.940	-0.793	-0.787
	3 × 3	-0.985	-0.862	-0.832
	4 × 4	-1.002	-0.864	-0.849

Table 5.9: Formation energies (eV/atom) with respect to bulk elemental phases for $\Delta\mu_{\mathrm{Ni}} = 0$ and S-rich (Mo-rich) conditions.

Formula	LDA	PBE	PBE + GD2
Mo	3.070 (0)	2.670 (0)	2.615 (0)
Ni	0 (0)	0 (0)	0 (0)
S	0 (1.535)	0 (1.335)	0 (1.308)
MoS_2	0 (0)	0 (0)	0 (0)
Mo_3S_4	0.504 (0.065)	0.455 (0.074)	0.498 (0.124)
Ni_2Mo	0.821 (-0.203)	0.778 (-0.112)	0.762 (-0.109)
Ni_3Mo	0.607 (-0.160)	0.590 (-0.078)	0.575 (-0.079)
Ni_4Mo	0.440 (-0.174)	0.452 (-0.082)	0.441 (-0.082)
NiS_2	-0.461 (0.563)	-0.249 (0.641)	-0.292 (0.580)
Ni_3S_4	-0.549 (0.329)	-0.347 (0.416)	-0.367 (0.380)
NiS	-0.538 (0.229)	-0.342 (0.326)	-0.360 (0.294)
Ni_9S_8	-0.559 (0.163)	-0.370 (0.258)	-0.376 (0.239)
Ni_3S_2	-0.520 (0.094)	-0.332 (0.202)	-0.335 (0.188)
$NiMo_3S_4$	0.396 (0.012)	-0.410 (0.076)	0.423 (0.096)

Dopant Site	Supercell Size	LDA	PBE	PBE + GD2
Mo subs.	1 × 1	-0.081 (0.430)	0.001 (0.446)	0.027 (0.463)
	2 × 2	0.050 (0.178)	0.068 (0.180)	0.070 (0.179)
	3 × 3	0.028 (0.085)	0.034 (0.083)	0.035 (0.084)
	4 × 4	0.017 (0.049)	0.020 (0.048)	0.021 (0.048)
S subs.	1 × 1	0.378 (0.122)	0.416 (0.193)	0.391 (0.173)
	2 × 2	0.141 (0.077)	0.133 (0.077)	0.133 (0.079)
	3 × 3	0.061 (0.033)	0.058 (0.033)	0.058 (0.034)
	4 × 4	0.035 (0.019)	0.033 (0.019)	0.032 (0.019)
t-intercal.	1 × 1	0.017 (0.017)	0.086 (0.086)	0.053 (0.053)
	2 × 2	0.0001 (0.0001)	0.024 (0.024)	0.016 (0.016)
	3 × 3	0.0001 (0.0001)	0.012 (0.012)	0.007 (0.007)
	4 × 4	0.0002 (0.0002)	0.007 (0.007)	0.004 (0.004)
o-intercal.	1 × 1	0.108 (0.108)	0.216 (0.216)	0.172 (0.172)
	2 × 2	0.042 (0.042)	0.062 (0.062)	0.050 (0.050)
	3 × 3	0.020 (0.020)	0.012 (0.012)	0.024 (0.024)
	4 × 4	0.011 (0.011)	0.017 (0.017)	0.014 (0.014)

Table 5.10: Formation energies with vacancy structures as the reference.

eV	Mo subst.	S subst.
2×2	-2.544	0.092
3×3	-2.609	0.159
4×4	-2.584	0.162

Formation energies are calculated for substitutional doping by filling a vacancy. Energies were calculated using: $E_{\text{form}} = E_{\text{doped}} - E_{\text{vacancy}} - E_{\text{Ni}}$. Mo substituted structures are calculated from Mo vacancies that are filled with a Ni atom. S vacancies are calculated from S vacancies filled with Ni.

Table 5.11: Newly active modes in Raman/IR spectra for 3×3 Mo substitution.

Classif.	Freq. (cm^{-1})	Activity	Description
New peak	60.92	R/I	In doped layer: in-plane, Mo, S, and Ni; S in-phase
	131.46	R/I	In doped layer: in-plane Mo, S, Ni
	132.40	R/I	S out-of-phase some z-direction and some in-plane
	161.97	R/I	Around dopant: Ni-Mo in-plane and S z-direction
	266.09	R	Around dopant: Ni in-plane and Ni-S symmetric stretching
	301.00	R/I	In doped layer: S out-of-phase
	345.17	I	In doped layer: S out-of-phase, in-plane
	356.06	I	S out-of-phase, in-plane
	363.88	R	In doped layer: in-plane 1st and 2nd S and Mo neighbors of Ni
	370.37	I	In doped layer: S in-phase, in-plane
Activation	208.86	R/I	In doped layer: Mixed $E_{1\mathrm{u}}$, $A_{1\mathrm{g}}$, $B_{1\mathrm{u}}$, and $E^1_{2\mathrm{g}}$
	223.87	I	In doped layer: Mixed $E_{1\mathrm{u}}$ and $E^1_{2\mathrm{g}}$
	387.74	I	In undoped layer: Mixed $E^1_{2\mathrm{g}}$ and $E_{1\mathrm{u}}$ (x)
	389.33	I	In undoped layer: Mixed $E^1_{2\mathrm{g}}$ and $E_{1\mathrm{u}}$ (y)
	456.80	R	In doped layer: Mixed $A_{2\mathrm{u}}$ and $B^1_{2\mathrm{g}}$-like mode
	470.18	I	In doped layer: Mixed $A_{2\mathrm{u}}$ and $B^1_{2\mathrm{g}}$-like mode

“In-” and “out-of-phase” refer to two S planes within a layer.

Table 5.12: Newly active modes in Raman/IR spectra for 3×3 S substitution.

Classif.	Freq. (cm^{-1})	Activity	Description
New peak	327.17	R	S out-of-phase between adjacent S planes, in- and out-of-plane, in-phase between layers
	333.45	R	In doped layer: S in-plane on doped S plane, out-of-plane in adjacent S plane
	336.69	R	In undoped layer: S in-phase between planes
Activation	473.49	R/I	$B^1_{2\mathrm{g}}$-like only on undoped layer

Table 5.13: Newly active modes in Raman/IR spectra for 3×3 t-intercalation.

Classif.	Freq. (cm^{-1})	Activity	Description
New peak	261.85	I	S in-plane breathing mode near Ni
	366.42	R	In 1-bond layer: in-plane breathing mode around Ni
	372.07	R	In 3-bond layer: in-plane breathing mode S near Ni
	434.90	R/I	In 3-bond layer: Ni-S asymmetric stretching
	452.44	R	In 3-bond layer: Ni-S symmetric stretching and S out-of-plane
	503.26	R/I	In 1-bond layer: Ni-S bond stretching
Activation	335.80	R	In 1-bond layer: $E_{1\mathrm{g}}$-like out-of-phase in x/y
	465.14	R/I	In 1-bond layer: Mixed $A_{2\mathrm{u}}$ and $B^1_{2\mathrm{g}}$-like + Ni-S stretch in 3-bond layer
	468.12	R/I	In 3-bond layer: Mixed $A_{2\mathrm{u}}$ and $B^1_{2\mathrm{g}}$-like + Ni-S stretch in both layers

Table 5.14: Newly active modes in Raman/IR spectra for 3×3 o-intercalation.

Classif.	Freq. (cm^{-1})	Activity	Description
New peak	212.48	R	Mostly in far layer: breathing mode around Ni, Mo and S in-phase, in-plane and S mostly out-of-plane (away from Mo plane)
	235.11	R	In far layer: in-plane breathing mode, Mo and S out-of-phase
	329.64	R/I	Mostly out-of-plane breathing by S around Ni
	360.58	R	In close layer: in-plane breathing by S atoms in one layer
	426.60	R	Symmetric Ni-S stretch
Activation	53.91	I	In close layer: $E_{2\mathrm{g}}^2$-like shearing mode and Ni plane-direction vibration (x)
	59.14	I	In close layer: $E_{2\mathrm{g}}^2$-like shearing mode and Ni plane-direction vibration (y)
	66.75	R	$B_{2\mathrm{g}}^2$-like layer breathing mode
	134.82	R	Mixed $B_{2\mathrm{g}}^2$ near Ni and Ni z-direction
	281.80	I	$E_{2\mathrm{u}}$-like mode (x)
	281.83	I	$E_{2\mathrm{u}}$-like mode (y)
	286.80	R	$E_{1\mathrm{g}}$-like mode (x)
	286.83	R	$E_{1\mathrm{g}}$-like mode (x)
	469.73	R	$B_{2\mathrm{g}}^1$-like mode

"Close" and "far" layer refers to proximity to the Ni atom, which is 0.3 Å closer to one layer than the other.

Chapter 6

Ni-doped MoS_2: Atomistic Mechanisms of Sliding in Few-Layer and Shearing in Bulk Doped MoS_2

This chapter is based on our publication in progress, “Atomistic Mechanisms of Sliding in Few-layer and Bulk Doped MoS_2” [56]. It is a followup applications to the structures found in Ch. 5. We use the different doped structures and subject them to shearing and interlayer sliding. We can compute the sliding potential, the change in energy throughout sliding, and explain it with atomic motion and bond changes. Unique challenges related to dopant are overcome by sliding while using steps of relaxation with analyses of the structures and energies at each step. We compared doped bulk and bilayer structures and quantified an important finding that explains results of previous works—the sliding potential can be described as pairwise interactions between layers. Furthermore, the outer S-layer decides the majority of the interaction. In effect, this means that the potential of an N-layer system can be computed as $N - 1$ sliding interactions.

6.1 Abstract

Sliding of two-dimensional materials is critical for their application as solid lubricants for space, and also relevant for strain engineering and device fabrication. Dopants such as Ni improve lubrication in MoS_2, surprisingly given that Ni intercalates and forms interlayer bonds. While atomistic mechanisms of sliding have been theoretically investigated in pristine 2D materials, there has been little work on doped forms, especially for the complicated case of intercalation. We use density functional theory to study sliding of Ni-doped MoS_2, considering Mo/S substitution and octahedral/tetrahedral intercalation. We find that bulk and trilayers are well described by pairwise bilayer interactions. There is a dramatic increase in the sliding barrier for tetrahedral intercalation, but the dopant minimally affects sliding between undoped interfaces, allowing Ni-doped MoS_2 to remain an effective lubricant. We provide an atomistic view of how sliding occurs in doped transition-metal dichalcogenides, and a general methodology to analyze doped sliding.

6.2 Introduction

MoS_2 is a semiconducting transition metal dichalcogenide with low-friction lubricative properties due to the ease of shearing of its lamellar structure. Doping of MoS_2 is a method to alter the electronic properties [11], increase the catalytic activity [123, 111], increase lubrication [191, 192], or layer dependence of friction [1]. Computations of friction in two-dimensional (2D) materials like MoS_2 [101, 213, 65, 198, 105], graphene [173, 198], and boron-nitride [112, 30] has been computed using models of varying complexity, but studies of the doped material are rare—especially intercalated doped materials. Some studies of C and Li in graphite have found tunability with those dopants, but we have not found studies of bulk or transition-metal-doped 2D material sliding potential analysis [129]. Mechanics of sliding in 2D materials is typically explored through computations of the sliding potential energy surface: [185] energies at different sliding amounts are computed with altering variables such as load or layer orientation. Sliding can also be important for strain engineering [134], nanoelectromechanical systems [100], oscillators [214], sliding ferroelectrics [209], and assembly of twisted bilayer structures [104]. For all these applications, it is important to understand how the atomistic mechanisms of slip which are understood in bulk materials are modified on the nanoscale for sliding in novel 2D materials, and especially how dopants influence sliding. In these van der Waals (vdW) mediated systems, a consensus has formed that the interfacial geometries and resulting charge density fluctuations are primarily responsible for the sliding potential's shape [101, 197, 198, 30] and has been used as the basis for a classical approximation of the potential [18, 112]. The sliding potential has been shown to be altered by S corrugation from layer rotation [101] or vacancy introduction [197] which can also happen by formation of distorted 1T phases [80]. In graphene/MoS_2 heterostructures, the sliding potential between structures is controlled by fluctuations in interfacial charge densities and not bonding [198]. This could be different when there are defects between layers [212], such as in the Ni-intercalated cases [58], where atoms between layers [28] can form covalent interlayer bonds [58]. Dopants, especially intercalated dopants, introduce local bond strain and atomic mobility which must be carefully considered during computation and analysis when compared to the standard approach. Ni increases the degrees of freedom, meaning we have to balance relaxing the local structure and preserving a quantifiable sliding amount. Previous simplifying methods like the registry index [18] are not easily applicable with intercalation where significant structural changes (e.g. bond changes) can occur. Direct energy comparisons become cumbersome when considering structures of different geometries, particularly when some layers are sliding and others are not, energy scales as with the number of active layers. Finally, choice in the initialization of structures in independent computations can affect the final result and lead to pathway discontinuities.

Previous sliding studies have extended to bilayers with vacancies [197, 219]. Like dopants, vacancies could introduce local bond reorganization which must be considered. Vacancy complexes as large as seven atoms were found to universally reduce the sliding barrier while leaving the potential's shape unaffected [197].

Dissociated H_2O's between layers has been found to severely diminish frictional capabilities, behaving similar in that capacity to the intercalated Ni computed in this work [212]. Conversely, Cheng *et al.* consider carbon doping in hexagonal boron-nitride bilayers with DFT. C's presence was shown to decrease the friction for substitution of either B or N [30]—the interlayer interaction is weakened by the dopant and thus lubricity is improved. By contrast, calculations showed that Li intercalation in graphite greatly increased barriers to sliding, due to electrostatic interactions after charge transfer from Li to semimetallic graphene layers [129]. We have previously computed that Ni-doped MoS_2 does not reduce the binding energy between adjacent layers as Li might do [38] but rather increases it substantially in t-intercalated doping [81], opposite to what was found for C-doped BN. While intercalated Li can be thought of like ball bearings that decouple MoS_2 layers and would reduce friction (though surprisingly it is not clear this effect has been measured), intercalated Ni instead increases the coupling between MoS_2 by bonding. Ni has been found to not significantly alter MoS_2's friction and enhance its resistance to wear, or layer flaking [170, 192], and may have promise for increasing the capabilities of lubrication in space [92]. This is consistent with the idea that Ni-doping improves MoS_2's resistance to wear (material loss through flaking) but appears counter to the idea that Ni doping improves lubrication [170, 192]. Calculations of Graphene/Fe_2O_3 interfaces with B, P, Si, and S dopants have found a frictional reduction. These defective cases do not consider the possibility of geometrical reorganization during sliding beyond the out-of-plane direction [101]. While that direction is likely the most energetically important, local bond distortions could occur at the defect sites during sliding and alter the sliding potential.

Ni has been found to improve MoS_2's lubrication performance [170], enhance MoS_2's catalytic activity, and alter the electronic properties [58]. We have previously computed four potential Ni dopant sites to MoS_2 [58, 81]: Mo substitution, S substitution, tetrahedral (t-) intercalation and octahedral (o-) intercalation and consider all of them in this work. In this article, we use density functional theory to explore how the presence of Ni modifies energy pathways and structures during sliding under different atomic constraints. We consider the Ni dopant locations in Fig. 6.1 and find the relation between bilayer sliding and bulk shearing. We provide insight and methods for analysis generally applicable to sliding of doped 2D materials.

6.3 Methods

6.3.1 DFT

We use the plane-wave DFT code Quantum ESPRESSO [50] to compute the properties of bilayer and bulk Ni-doped MoS_2, like our previous work on the material [58, 81]. We use the Perdew-Burke-Ernzerhof [139] generalized-gradient-approximation functional the Grimme-D2 [53] (GD2) vdW correction term. This correction is necessary in MoS_2 to capture the weak vdW interactions which mediate the sliding potential in pristine MoS_2. We use the Norm-Conserving pseudopotentials [153] as parameterized by PseudoDojo [187].

$2 \times 2 \times 1$ supercell of the 6-atom unit cell were used with one Ni atom per cell. Bulk (finite layers) were computed using a half-shifted Monkhorst-Pack grid of $6 \times 6 \times 2$ ($6 \times 6 \times 1$) for the pristine cell and $4 \times 4 \times 2$ ($4 \times 4 \times 1$) for doped cells. Kinetic energy cutoffs of 60 Ry were used. Self-consistent field (SCF) energies were computed to thresholds of 10^{-8} Ry. Total energies and forces were relaxed to 10^{-6} Ry and 10^{-4} Ry/Bohr. Stress relaxations used thresholds of 0.05 kbar.

6.3.2 Few-layer computations

Bilayer cells' component c_z was set to 25 Å and were not relaxed and c_x was not altered, unlike their bulk counterparts. Trilayers of pristine, Mo-substituted, and t-intercalated structures were computed by adding a third, pristine layer to the bilayer structure and adding the layer thickness to c_z and used identical approximations as the bilayer. 4-layer out-of-plane supercell bulk structures are extensions of the pristine, Mo-substituted, and t-intercalated bulk structure cells with the dopant kept in only one layer.

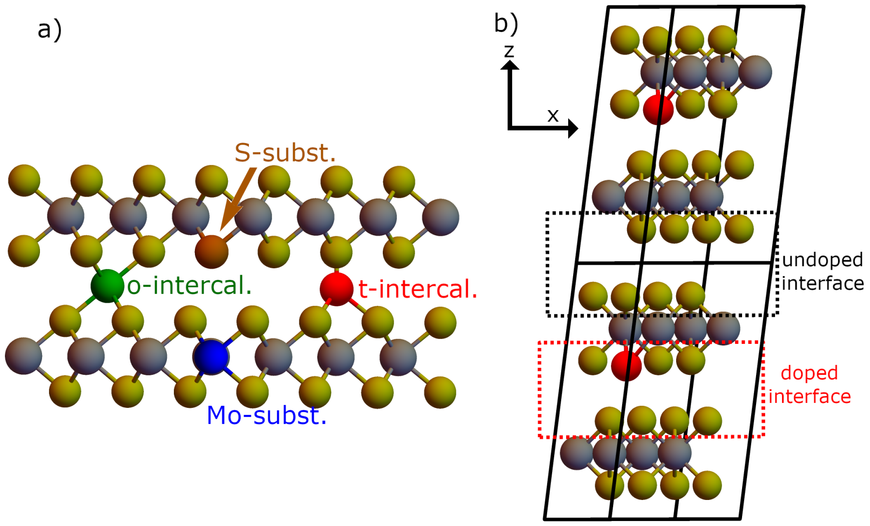

Figure 6.1: a) The four considered dopant sites previously found to be stable or metastable [58]. Bilayer and bulk structures with similar atomic coordinates are computed. b) A sheared S-substituted cell showing two distinct interfaces in each bulk cell.

6.3.3 Sliding and shearing under four sets of constraints

The energies of doped and pristine 2H-MoS$_2$ were computed after relative sliding using different stages of constraints. Initial structures are generated by fully relaxing doped bulk structures, then forcing hexagonal symmetry onto the cell (relaxed cell angles differ from the pristine 120° by at most 0.025°, and energies differ by 10^{-4} eV/atom). Our coordinate system has the x-axis in the zigzag direction and y-axis in the armchair direction. The top layer is then displaced in the x-direction by Δx in steps of 1/12th of the cells' respective lattice constant a. a was set to 3.19018 Å, 6.39945 Å, 6.38666 Å, 6.35100 Å, and 6.39413 Å for pristine, Mo-substituted, o-intercalated, S-substituted, and t-intercalated in both bulk and bilayers. In bulk, the x-component of the out-of-plane vector a_3 was set to $2\Delta x$, such that every pair of layers experienced relative sliding of Δx. In intercalation, Ni was moved along with the mobile top layer, since it was closer to the intercalant. Substitutional Ni was moved along with the layer it is in. Energies are computed by SCF and then the structure is relaxed by three successive levels of constraints as summarized in Fig. 6.2. (1) Atoms are allowed to relax in the

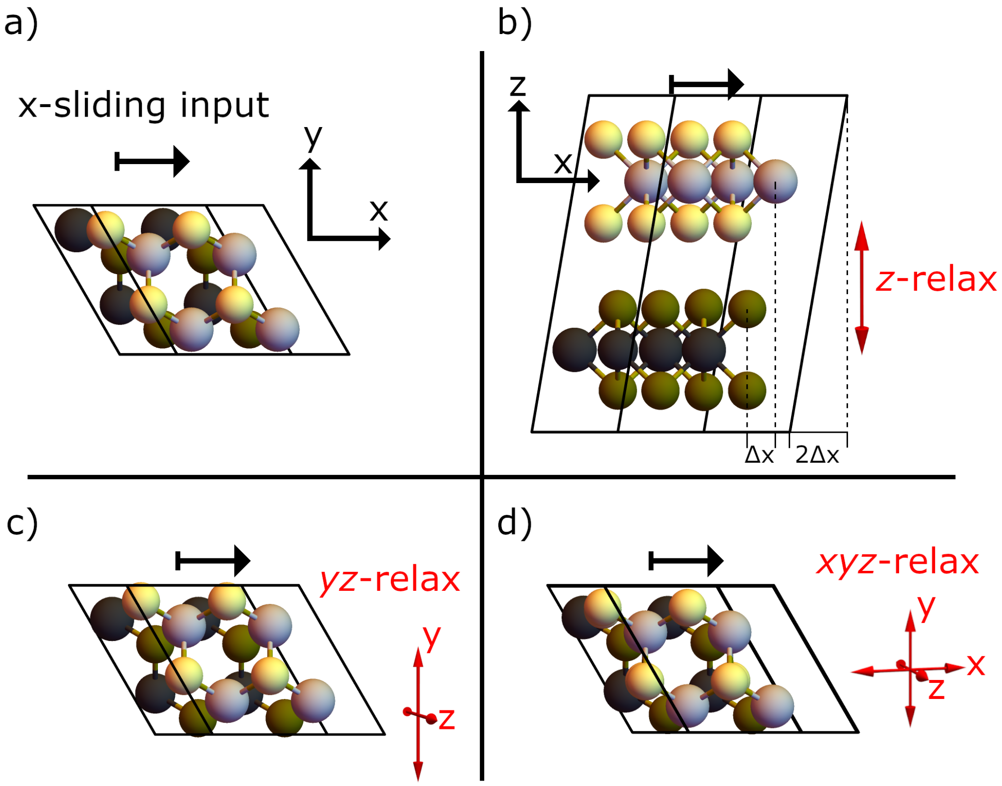

Figure 6.2: Sliding was analyzed using four kinds of calculations, with relaxation of an increasing number of degrees of freedom of the Mo and S atoms. a) No relaxation, b) z-relax, c) yz-relax and d) xyz-relax (only used for bulk). Dark atoms indicate the lower layer. Ni atom's coordinates are fully relaxed in b)-d).

x-direction and the c_z lattice parameter is relaxed (z-relax). (2) Atoms are further relaxed in their y coordinates (yz-relax). (3) Atoms are further still relaxed in x (xyz-relax). Throughout stages (1)-(3), the Ni atom is allowed to relax in all coordinates so as to capture its preferred movement throughout sliding.

Each constraint gives us different information about the structure throughout sliding. z-relax yields the 1D-sliding potential as it relates to interlayer distances. yz-relax allows us to access the 2D-sliding potential and find deviations from the low-barrier sliding pathway. xyz-relax allows us to test whether shearing occurs like a deck of cards or with the presence of slip planes. Furthermore, the initial structure after sliding but before relaxation can be thought of as stage (0) no relaxation. Here, we gather information about the symmetries.

It is important to relax the Ni during intercalated sliding because the local geometry is expected to change when it experiences different local environments. Ni bonding remains at 6 and 3 bonds for Mo-substituted and S-substituted sites throughout sliding respectively, but bonds form and break for intercalated sliding. Given full relaxation freedom in xyz-relax, both structures follow paths with four Ni-bonds, indicating the high stability of that bond configuration.

6.4 Results and Discussion

6.4.1 No-relax and symmetry

The sliding potential in both bulk and bilayer shows a mirror symmetry in the x-direction. This is due to the AA′ configurations of pristine, Mo-substituted, S-substituted, o-intercalated, and t-intercalated belonging to symmetry point groups $\mathrm{D_{6h}}$, $\mathrm{D_{3h}}$, $\mathrm{C_{3v}}$, $\mathrm{C_{3v}}$, $\mathrm{C_{3v}}$ respectively. Each of those point group contains an xz-function in an irreducible representation—guaranteeing a critical point in the sliding potential. In pristine, this information can be used to reduce the computational workload, but once the doped structure is relaxed, there is slight symmetry breaking in all doped cases, quantified in Fig. 6.14. Since every interface involves at least one pristine layer, the symmetry of the full sliding potential shows hexagonal symmetry.

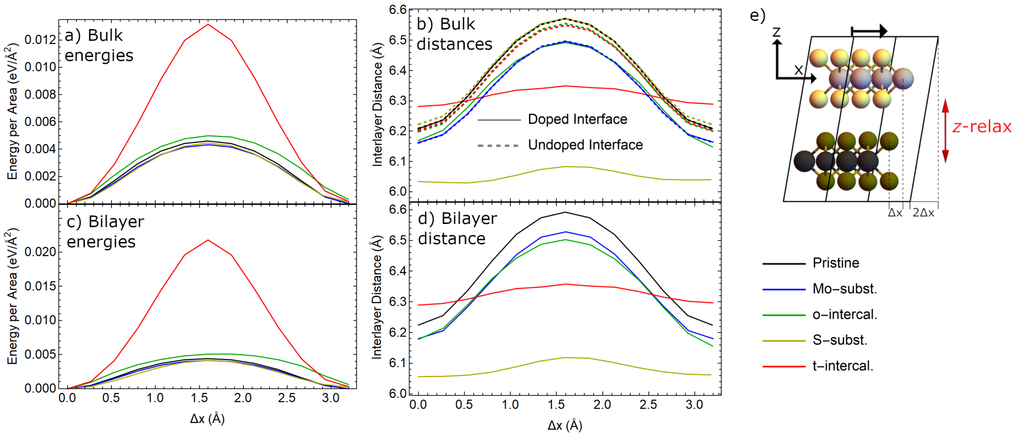

Figure 6.3: Energies and interlayer distances for x-sliding after z-relax conditions were applied as in e). Energies for a) bulk and c) bilayer shown are divided by the areas of the actively sliding interfaces (i.e. 2× cell's area in bulk, once in bilayer). Interlayer distances in b) are compared between doped (solid) and undoped (dashed) interfaces. S-substitution and t-intercalation show the largest difference between the two, where they have a strong preference to keep the interlayer distance the same. d) Bilayer distances are similar in shape to bulk.

6.4.2 z-relax: 1D sliding potential

Results of z-relax in Fig. 6.3 show that the sliding barrier is massively increased in t-intercalation, unlike previous results with vacancies [197]. This, along with Fig. 6.4, point to the high stability of the 4-bonded Ni-configuration. The difference between t- and o-intercalations' energetic response to 1D-sliding can best be explained by Fig. 6.4. Given that the 4-bonding Ni-configuration is low in energy, t-intercalation is forced to move away from that value while o-intercalation is allowed to move closer. Fig. 6.3b separates c_z into the two interlayer distances present in a cell. These distances are the same for pristine and Mo-substitution, where every other interface is equivalent, but are not for the other structures. This leads to the surprising result that t-intercalated and S-substituted structures attempt to keep their interlayer distance where the Ni is between two layers. This propensity for the interface in these sites to remain similar throughout sliding suggests that the slip planes occur away from the dopant site.

Bonds to Ni were counted in Fig. 6.4 using the Tersoff bond order function [177] $f_C(r)$, where r is the interatomic distance for a given pair of atoms and is

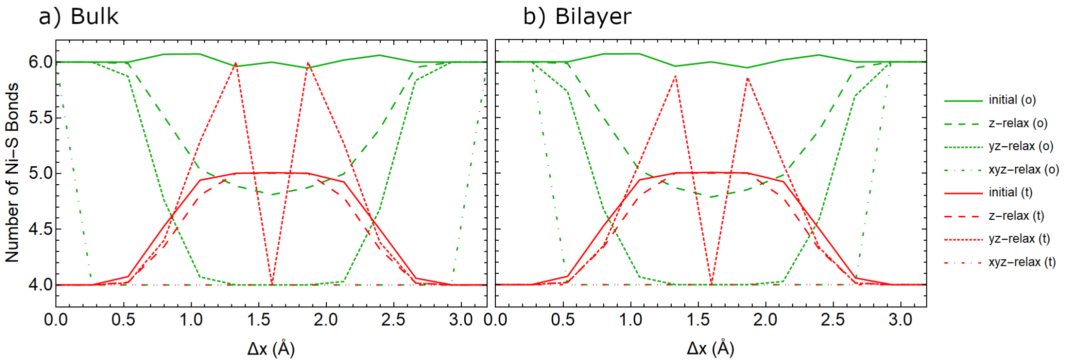

Figure 6.4: Bond count as a function of Δx for o-intercalated (green) and t-intercalated (red) structures at the four constraint levels as computed by the Tersoff bond order function for a) bulk and b) bilayers. Given the most freedom, xyz-relax, structures reorganize to form four bonds, despite less favorable stacking. The large spike at $\Delta x = 1.6$ Å for t-intercalated yz-relax is the result of the structure reorganizing to an equivalent stacking to the $\Delta x = 0$ Å configuration (see Fig. 6.5). a) and b) are nearly identical.

defined as:

$$N_i^{\text{bonds}} = \sum_{j \neq i}^{\text{atoms}} f_C\left(\|\vec{r}_i - \vec{r}_j\|\right) = \begin{cases} 1 & r \leq R - D \\ \frac{1}{2} - \frac{1}{2}\sin\left(\frac{\pi}{2}\frac{r-R}{D}\right) & R - D < r < R + D \\ 0 & r \leq R + D \end{cases} \tag{6.1}$$

where the bond cutoff $R = 3.2$ Å and the smoothing parameter $D = 0.3$ Å were chosen such that: (1) equilibrium o- and t-intercalated structures were computed to have 6 and 4 bonds respectively, (2) equilibrium Mo-substituted and S-substituted structures have 6 Ni-S and 3 Ni-Mo bonds respectively, and (3) variation in numbers of bonds with sliding is reasonably smooth. At equilibrium, the Ni-S bond lengths are 2.38 Å, 2.12-2.17 Å, and 2.36 Å for Mo-substituted, t-intercalated and o-intercalated respectively, while the Ni-Mo bonds lengths in S-substitution are 2.68-2.78Å [58]. As layers slide, the identifiers “tetrahedral” and “octahedral” are used to describe the initial structure, despite the fact that bonds change as in Fig. 6.4.

6.4.3 yz-relax: Traversing the 2D sliding potential

In yz-relax, the structures are free to follow a curved path indicative of the familiar zigzag sliding pattern [101, 18] of hexagonal lattices. This curved path is quantified as $\Delta y_{\text{relaxed}}$, the mean difference in Mo y-coordinates when compared to the $\Delta x = 0$ Å structure. The white circle in Fig. 6.5 represents the metastable AB$'$ stacking of the pristine structures. Besides t-intercalation, doped structures follow a pathway to equivalent sites through the same metastable site. The t-intercalated structure instead relaxed to a stacking equivalent to the lowest-energy stacking, causing discontinuities in Δy at $\Delta x = 1.6$ Å in Figs. 6.5 and 6.4. This is likely due to the deep well at the equivalent stable stacking to attract our system to that configuration, and small barriers could be overcome by the BFGS quasi-Newton algorithm as implemented in ESPRESSO [44]. In Fig. 6.3, we included a structure computation which follows the trends better, but was obtained by altering the relaxation scheme. It was initialized by sliding a nearby structure, rather than the initial 2H structure. Furthermore, both intercalated structures deviate slightly in their sliding pathway due to forces from the Ni-S bonds. The results of this method are reminiscent of what may be achieved through the nudged elastic band method [213, 221]. though we do not require the images to remain close by. This method accesses the 2D-sliding path by simply allowing the system to 'fall' into low-energy pathways in the potential energy surface. Given the complexity introduced by local atomic organization, this analysis approach can capture the concerted relative sliding of layers but also allowing for local symmetry breaking with relaxations of atoms nearby the Ni atom. Along the stable-metastable sliding path, S-substituted layers attract the opposite layer during sliding (Fig. 6.5b), as we also found when applying increasing loads in Fig. 6.13. For y-sliding in Fig. 6.11, we instead use xz-relax conditions, but we found that the structure did not deviate from a straight path along the y-axis due to mirror symmetry in the xz-plane which is preserved for displacement along the y-axis.

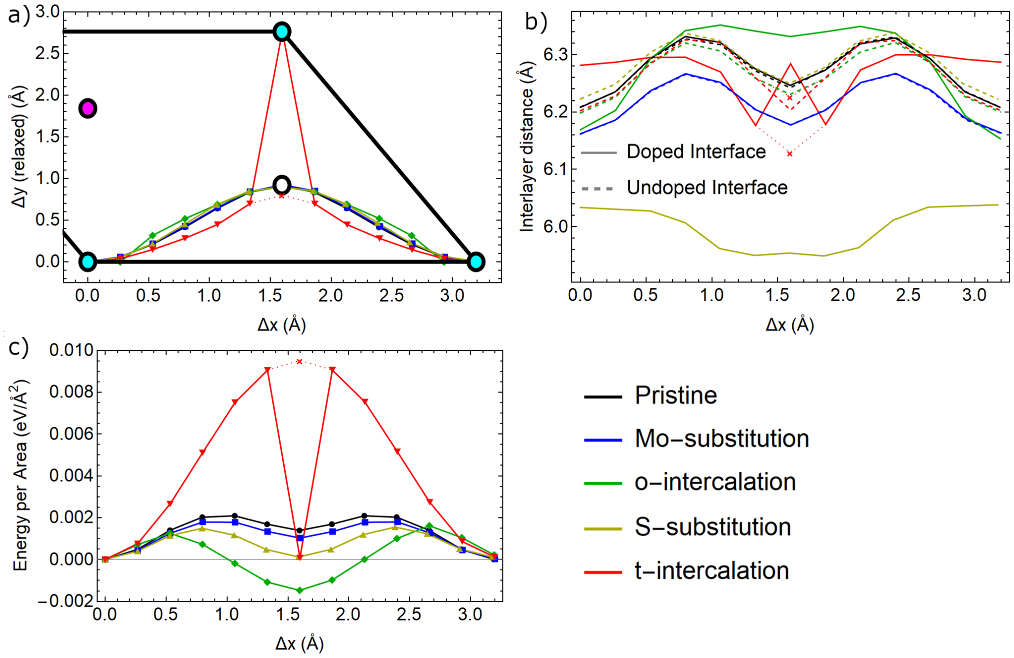

Figure 6.5: Structure and energy of bulk sliding layers by Δx then relaxing in y and z coordinates. a) The relative displacement after relaxation. Cyan circles indicate the starting AA′ structure. White indicates the metastable AB′. Magenta indicates A′B stacking. Given the opportunity to relax in y, structures traversed the potential surface between stable and metastable stackings. b) Mo-Mo interlayer distances are shown for both doped and undoped interfaces. S-substitution, unlike others, does not increase its doped interface's interlayer distance, indicating an attraction between the dopant and its opposite layer. c) Energies along the sliding path are displayed as well. For b)-C), a red × indicates the t-intercalated structure as generated by a different scheme than other structures to target the AB′ stacking.

6.4.4 xyz-relax: Slip-plane detection

We use the final constraint, xyz-relax to detect the preferred locations of slip-planes. Fig. 6.6a shows $\Delta x_{\text{relaxed}}$, the difference between x-coordinates of Mo atoms of the two layers in the cell with respect to Δx. By sliding the layers uniformly and shearing the cell then relaxing along that same sliding direction, we can see whether it is favored to have uniform relative displacements between layers, more displacement between doped interfaces, or less displacement between doped interfaces. For pristine and Mo substitution, the two interfaces are identical by symmetry and must have the same displacement, but other structures break this symmetry and can have different displacements. The t-intercalated interface shows a strong preference for the 2H AA$'$ stacking. Conversely, S-substituted and o-intercalated interfaces prefer the metastable stacking. This suggests that these structures show a preference to the slip plane shown in 6.6b, but larger supercells in the z direction are required to break the Mo-substituted symmetry and test its slip-plane preference directly.

To that end, we compute a few bulk supercells with 4-layers but only one doped layer in (Fig. 6.6c-d) (note this has half the Ni concentration as our structures thus far). Both Mo-substitution and t-intercalation relax to alternative stacking configurations than the input uniform sliding. We compute the $\Delta x_{\text{relaxed}}$ of the four interfaces, or pairs of layers, and contrast the behavior of interfaces involving *vs.* not involving the dopant. We find doped Mo-interfaces absorb the sliding, while the undoped interfaces attempt to remain in 2H-stacking. At around 0.5 and 1.2 Å, instabilities due to small energy differences in layer orientation emerge, but the undoped interface ultimately remains closer to AA$'$ stacking. Conversely in t-intercalation, $\Delta x_{\text{relaxed}}$ stays near 0 Å throughout sliding for the doped-interface, just as in the two-layer per cell structure in Fig. 6.6a. Pristine structures, even when perturbed, relax to a uniform shearing as in Fig. 6.6b. This study locates the slip plane at the doped interface for Mo-substitution (as in Fig. 6.6b iii) and away from the interface at t-intercalation (as in Fig. 6.6b ii). The in-plane lattice is not relaxed.

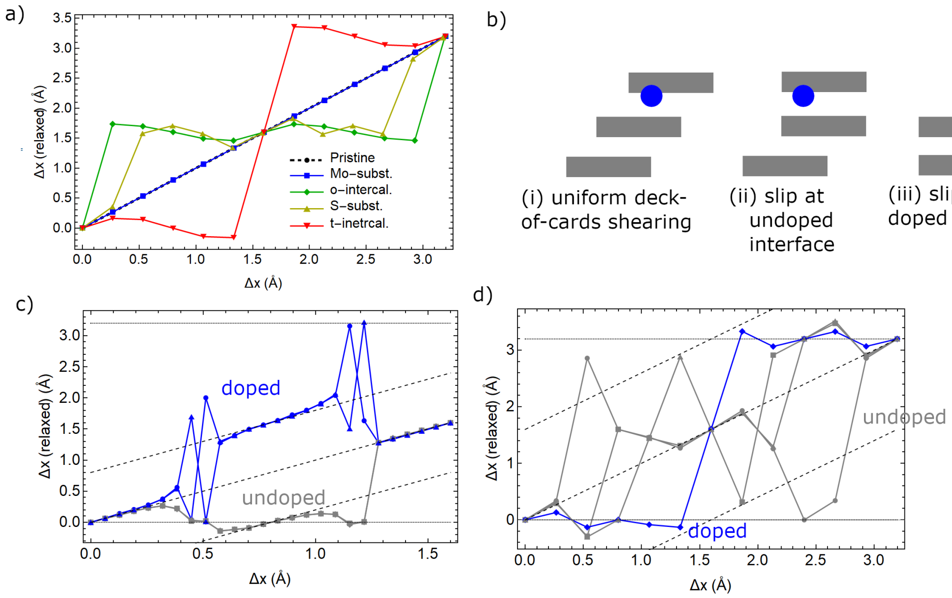

Figure 6.6: Geometry after bulk shearing in x by Δx then relaxing in x, y and z coordinates. a) The relaxed sliding distance Δx_{relax} as a function the input sliding distance Δx. b) A schematic of potential multilayer slip-plane configurations. c) Mo-substituted and d) t-intercalated interlayer x displacements, Δx(relaxed) for doped (blue) or undoped (gray) interfaces for four-layer bulk structures.

6.4.5 Matching bilayer sliding to bulk shearing

The bulk structure we have shown thus far contains two interfaces within each cell and have a concentration of one Ni for 8 MoS_2 units. To understand the range of interactions and quantify how well this may match other concentrations of dopants, we computed an isolated bilayer system with the same starting structures as in bulk, but with vacuum in the c direction. Relaxing such structures with identical constraints yields the same stacking configurations found in the bulk. This leads to the intuitive result that the interlayer interactions in the bulk structure can be computed as pairwise interactions of bilayers as summarized in Fig. 6.7—effects are local to the layers, van der Waals and covalent, not modified by farther away or electrostatic charge transfer. This coincides with comments that the interfacial geometry [198], and not any deeper structures, are almost entirely responsible for the shape of the sliding potential. As shown in Fig. 6.7, the practical result is that we can construct the bulk sliding energies by summing up appropriate sliding potentials of bilayer computations. Namely, bulk o-intercalation, t-intercalation, and S-substitution potentials are sums of their bilayer counterparts and the pristine computation while bulk Mo-substituted and pristine are twice their bilayer counterpart potentials. Fig. 6.7d, for example, has two interface interactions in our bulk structures, one interface with no Ni atom and one with the Ni atom—so we approximate it by summing up a pristine bilayer sliding potential and the Ni@t-intercalation bilayer sliding potential to remarkable accuracy. In effect, this leads to the conclusion that arbitrary layered structures can be computed as an appropriate ensemble of bilayer computations that match the interfacial geometry. Work by Hu *et al.* [65] studied sliding in 5-layer systems using classical potentials. Such a study would be expensive using density functional theory due to the large number of atoms, but could be cheapened dramatically while achieving DFT-level accuracy by careful combination of four bilayer computations representing the interfaces.

To directly test the localization of the interaction at the interface, we computed a few trilayer scenarios. The top two layers were pristine in all scenarios. The third layer is initially attached to the middle layer and is set to either t-intercalated,

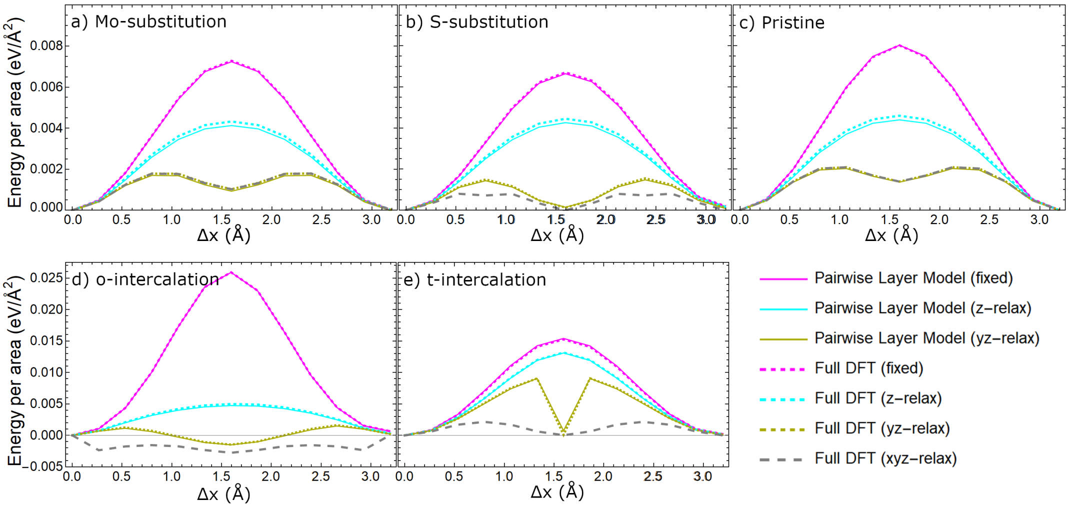

Figure 6.7: The computed (dashed) variation in sliding potential in bulk plotted against sums of bilayer sliding potentials (solid). Bilayer structures whose interfaces match those in bulk are used: two Mo-substituted-to-undoped bilayer interactions generate one bulk Mo-substituted sliding potential, others are sums of one undoped interface (i.e. pristine bilayer sliding) and one doped interface. The approximation would only be suitable for xyz-relax conditions if a full 2D sliding potential is computed, since relaxing bilayers in all coordinates yields the 2H stacking.

Mo-substituted, or pristine. We treat the system up to yz-relax only. We find that the bottom pair of layers remain in the 2H stacking throughout sliding in all conditions. The top pair of layers follow an identical trajectory as the pristine bilayer and the sliding potential per area is indistinguishable in all three scenarios, corroborating that only the active interface contributes to the sliding potential of 2D materials. As a lubricant, Ni-doped MoS_2 shows higher resistance to wear and lower friction than pristine MoS_2. Given the increased sliding potential maximum of t-intercalated MoS_2 when compared to pristine, one may be tempted to assume the increased lubrication incompatible with t-intercalation. Our result subverts that expectation. With previous computations of the dissociation energy [81], t-intercalation may bind the layers therefore decreasing the wear rate. Slip in t-intercalated MoS_2 can occur at the undoped interface, avoiding high-barrier t-intercalated sliding and relegating all of the sliding to undoped interfaces.

6.5 Conclusion

This work elucidates the atomistic mechanisms of doped 2D materials and outlines a systematic pathway to study systems with otherwise large degrees of freedom. The analysis pathway used is applicable to any layered material and at computational levels other than DFT, though an adequate model of the vdW interaction is critical for accuracy. Given that the pairwise bilayer interactions accurately describe the bulk, arbitrarily-layered systems could be discretized and computed as bilayers that represent each interface. This could reduce computational cost while keeping accuracy of many-layered studies [65]. The variable constraint method used here can be used to simplify the complicated structures with dynamic internal components, such as in S-substituted or intercalations. We used these to find a low-barrier sliding path, compare the Ni's site-dependent alterations to the sliding potential, and locate the likely slip planes in those structures. A potentially perplexing result that t-intercalation has a large sliding potential and yet can lead experimentally to lower friction can be explained as the presence of shear planes away from intercalated layers. Our results provide general insight into sliding of doped 2D materials, for use in applications and for tuning sliding interactions in 2D materials, and our work offers a general approach for analysis, including for mapping out sliding potential energy in 2D.

6.6 Supplementary Materials

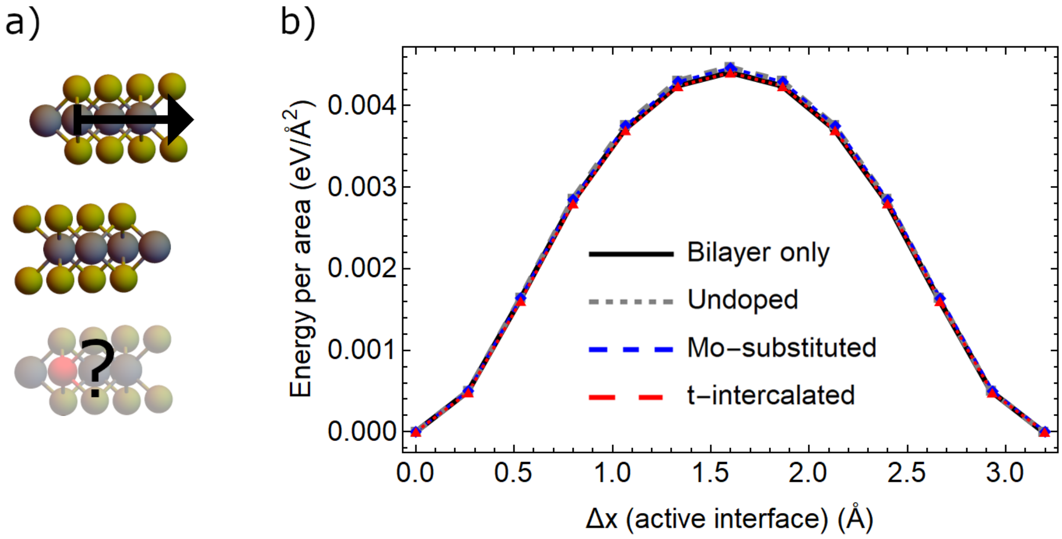

Figure 6.8: Sliding in three-layer systems *vs.* undoped bilayer (black). The top pair of layers are undoped and are slid next to each other then relaxed in the z-direction. The sliding energy is divided by the area of the active sliding area, so as to keep it comparable with the bilayer. The presence of a third layer (doped or undoped) does not change the sliding potential by more than 1.5%.

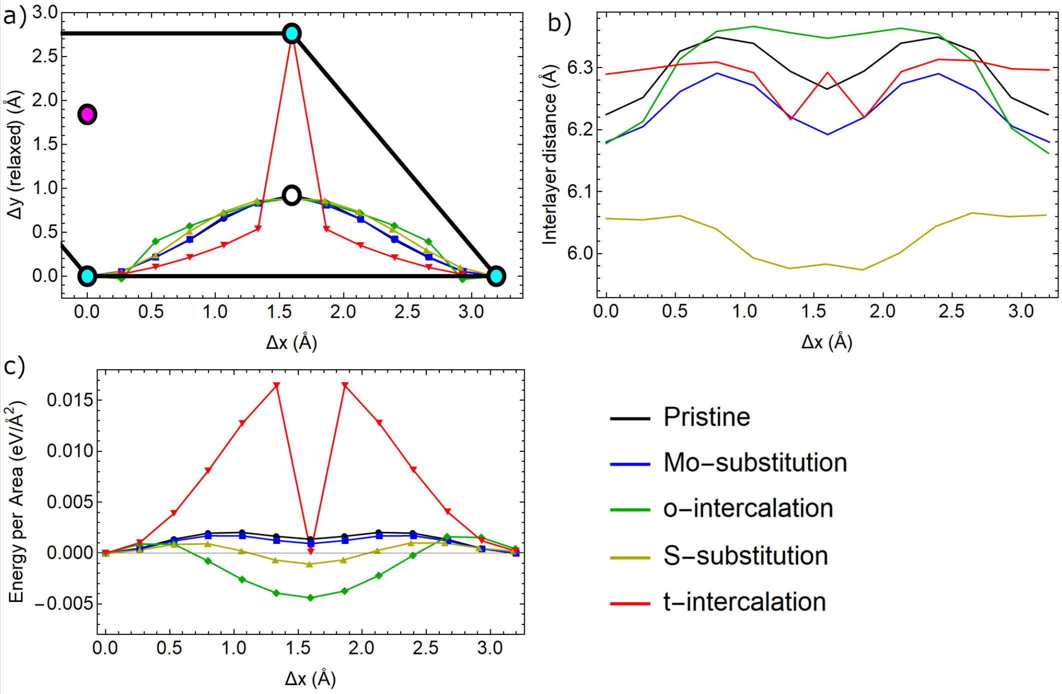

Figure 6.9: a) Sliding path under yz-relax constraints of bilayers slid in the x-direction. Deviations from the pristine zig-zag path are slightly more pronounced in all cases. b) Interlayer distances show identical pattern to bulk shearing, albeit at a slightly larger value as compared in Fig. 6.10. c) Sliding energies divided by one cell's area.

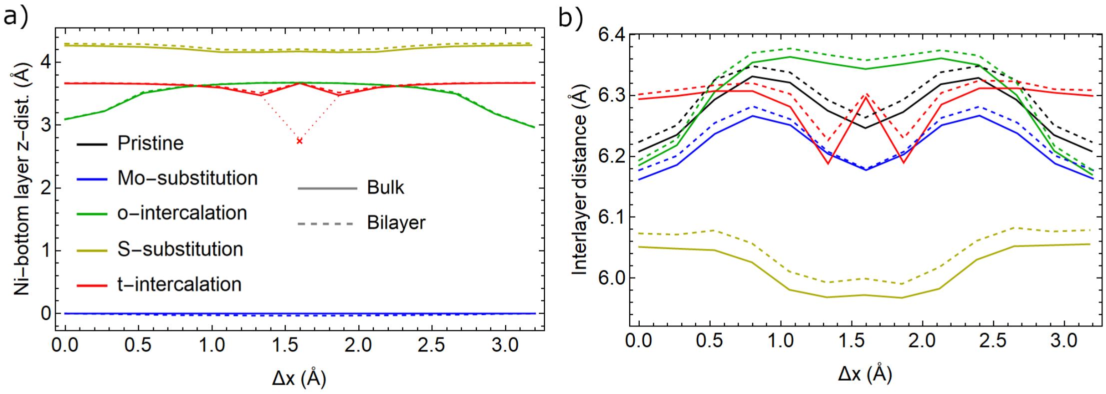

Figure 6.10: a) Ni's out-of-plane distance with respect to the bottom layer (see Fig. 6.1 for relative Ni positions in main text) under xz-relax. The red × indicates the t-intercalated structure that used a different generation scheme to relax it near the AB′ stacking configuration. b) Mo-Mo interlayer distances comparing bilayer (dashed) to bulk (solid) for xz-relax.

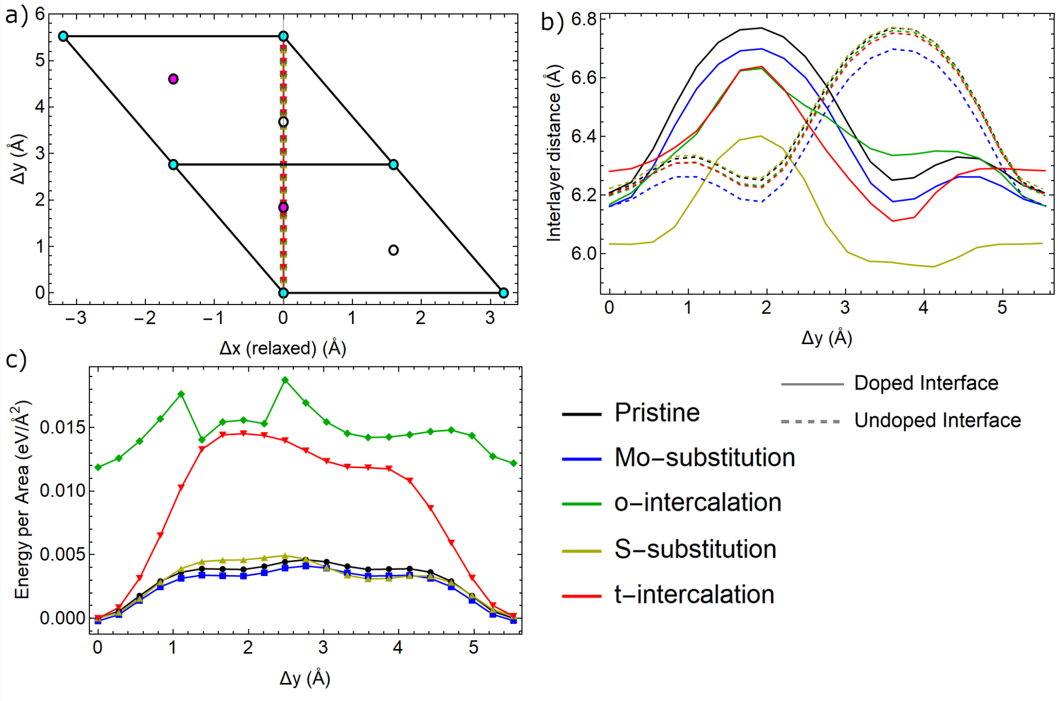

Figure 6.11: Relative sliding for y-sliding of bulk and bilayer with xz-relax constraints. a) Sliding path with respect to the pristine cell sites. Cyan, white, and magenta circles indicate AA′, AB$_1$, and A$_2$B respectively. Yellow circles represent the saddle-point stacking. Unlike in x-sliding, the structure did not deviate much (10^{-4} Å) from the path, despite being given freedom in the x-coordinates. b) The Mo-Mo interlayer distance shows little difference in the undoped interfaces between the different sites, but the doped interfaces vary in shape with S-substitution then intercalations showing greatest variabilities. c) Sliding energies (divided by twice the cell's area, once for each active sliding interface) lack the same mirror-symmetry seen in x-sliding. Ni in the o-intercalation case switches between the same state as the t-intercalation, between 1.5-2.0Å. Since these are stoichiometrically equivalent, we referenced the octahedral energies against the $\Delta y = 0$Å, t-intercalated structure.

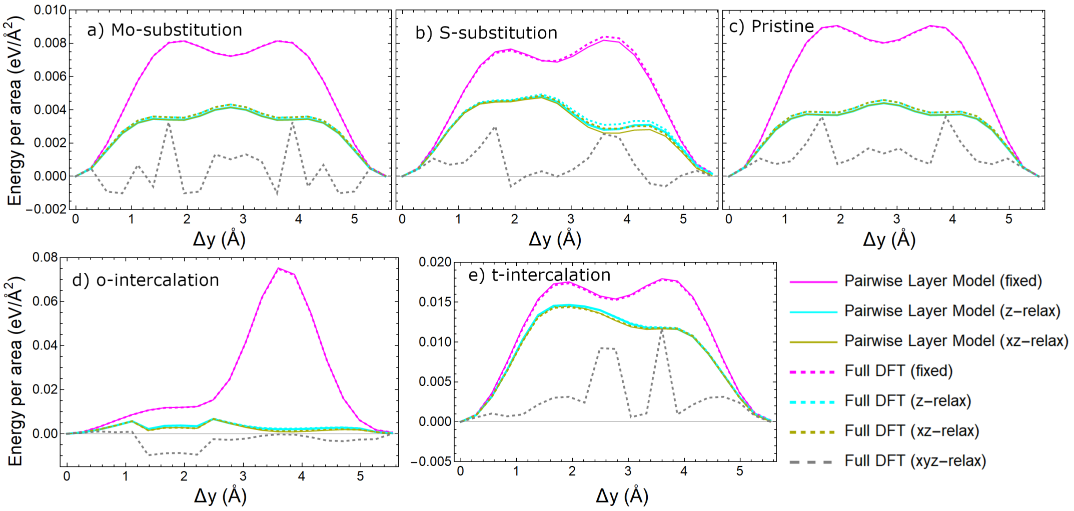

Figure 6.12: Energies per sliding active layer are plotted for the different doped structures. Full bulk DFT (solid) and pairwise combinations of bilayers (dashed) for doped MoS_2. The y-direction sliding potential for a single pristine interface is not symmetric, but the two interfaces in the bulk structure are sliding in opposite orientations. This leads to a symmetry in c) pristine from a 180° rotation of the interface, which is broken in the doped structures. Bulk sliding potentials for b) S-substitution, d) o-intercalation, and e) t-intercalation are computed as sums of the doped bilayer and the undoped potential. Bulk a) Mo-substitution and c) pristine potentials are sums of their bilayers potential and its own reverse, to account for the interlayer sliding orientations.

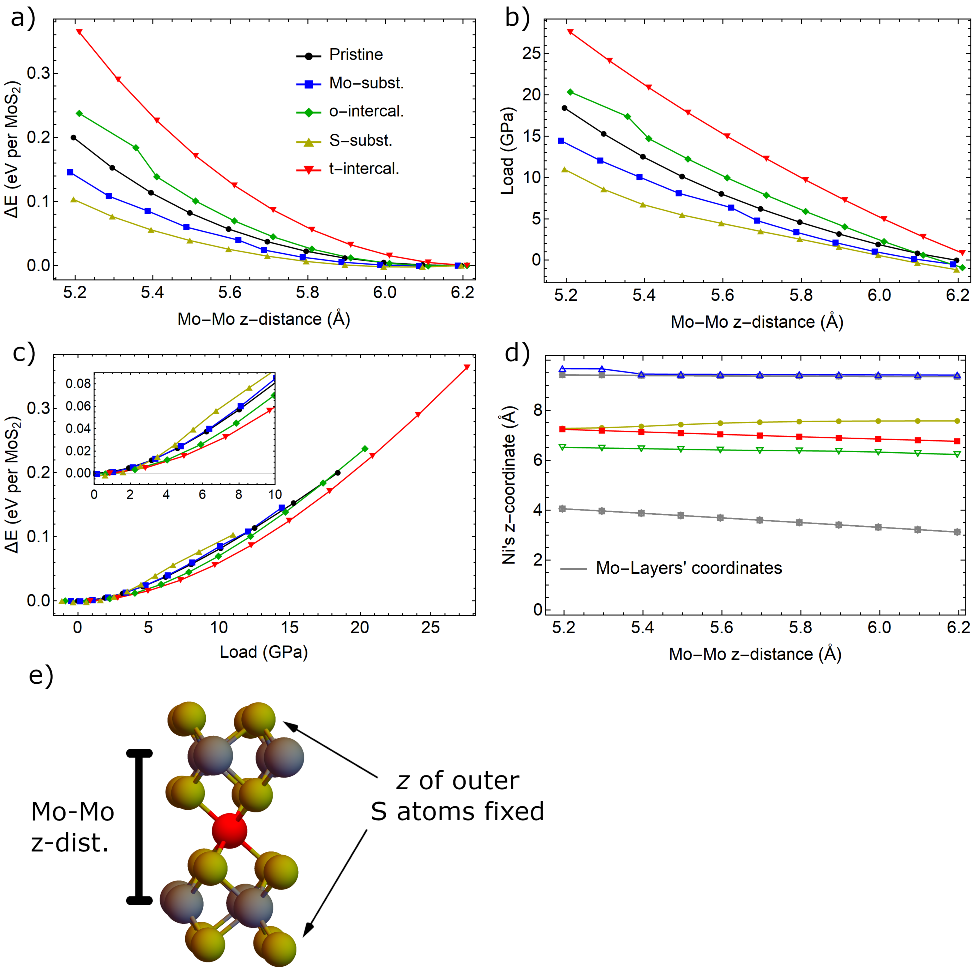

Figure 6.13: Computations of load applied to the sliding = 0 Å bilayer of 2 × 2 supercells. The layers are compressed and the z-coordinates of the outer S atoms are fixed, as shown in d. All other atomic coordinates and the cell parameters a and b are allowed to relax. The relative energy a) and load b), computed as the sum of the forces on the upper fixed S-atoms divided by the cross-sectional area) are plotted against the Mo-Mo z-separation, or interlayer distance. Loads show a similar ordering in elastic C_{33} values previously computed [58], except for S which shows nonlinear behavior in its Ni. Energies and loads of intercalated MoS_2 are more sensitive to compression than pristine MoS_2, opposite to the substituted structures. Load *vs.* ΔE c) show that doped and pristine are not related by a simple scaling factor, but nonlinear relationships emerge from the Ni's dynamic behavior. This is most apparent in S-substitution in the zoomed inset in c., where, unlike other scenarios, the Ni atom is attracted to the opposite layer during compression, rather than repelled. d) Ni-coordinates are for the different doped structures are plotted along with the layers' coordinates (gray). S is attracted to the opposite layer with increased compression.

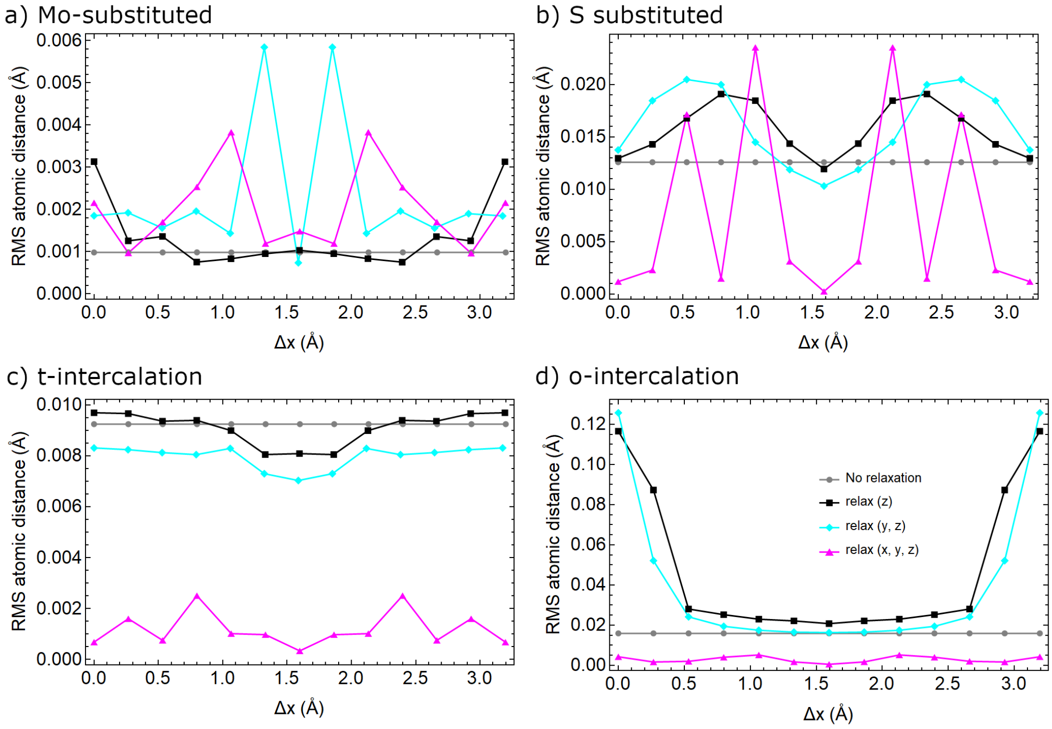

Figure 6.14: The RMS of the atomic distances between a right-direction bulk slid structure and its left-direction counterpart. These are computed by taking the structure slid by Δx, reflecting across the yz-plane, then comparing to its nearly symmetric counterpart, at $a_p - \Delta x$, where a_p is the pristine lattice constant. RMS of the atomic distances between atoms that lay nearly on top of one another are shown. (i.e. $\sum |S_x \mathbf{R}(\Delta x) - \mathbf{R}(a_p - \Delta x)|^2$).

Chapter 7

Ni-Doped MoS_2: Paremetrization of a ReaxFF Reactive Force Field for Ni-Doped MoS_2 using DFT

This chapter is based on our contribution to the publication in progress led by Karen Mohammadtabar at the Martini group at UC Merced [116]. The goal is to use DFT to parameterize a classical reactive force field for Ni-doped MoS_2 for use in tribological studies. The result is a faster and cheaper classical force computation but with accuracies only limited by the quality of the parametrization. This force field is designated to model sliding in larger MoS_2 systems (1000+ atoms), but it could be used in other applications, such as catalytic activity. One of the Martini group's computational methods involves using ReaxFF [186, 156], a method that uses a "reactive" force field that can model bond breakage and formation accurately. The Martini team was tasked with that aspect of the project while ours was focused on the DFT parametrizations. Applications of interest have been detailed in Chs. 5 and 6. With the plan of using the ReaxFF potential to study tribology, this chapter follows Ch. 6 which conducted smaller scale but in-depth analyses of Ni-doped MoS_2 sliding.

7.1 Introduction

Density functional theory (DFT) can provide a great deal of information about the possible structures involved in sliding, but they can be computationally demanding for large structures—especially those that may play a role in macroscopic sliding. Classical molecular dynamics (MD) is an approach that can be used in tandem with DFT. Here, the evolution of the structure is tracked through solving low-cost Newtonian equations, but the potential must first be parametrized and validated by DFT [148].

ReaxFF reactive force fields [186] are classical force fields designed to generate accurate models of systems with bond breakage and formation. The potential requires a choice of empirical parameters that weighs the importance of its energy components. ReaxFF has previously been parametrized for bilayer 2H-MoS_2 which successfully captured vacancies formation energies, large curved geometries, and relative stacking configurations [127]. Their work also provided an initialization for our Ni-doped potential, as it should capture most of the Mo and S behavior and leaves us to optimize mostly the Ni-related parameters. Force fields have successfully studied many of MoS_2's mechanical and catalytic properties, however the surface energy barrier height has been inaccurate. Successes include MoS_2 formation [127, 27], the active sites of MoS_2 edges [66], defect creation [127, 216], and multilayer tribology [160].

Previously, DFT works have investigated the tribology of MoS_2 under various conditions as discussed in Ch. 6. Vacancies, a comparable defect to substitution, have been found to have reduced sliding barriers [197]. Layer orientation and stress can alter the shape of the sliding potential and can move the maxima and minima to different stackings [101]. Sliding heterostructures, such as MoS_2 on graphene [198] or MoO_3 [105], are extended versions of what we are studying here—where one layer is doped and another is not. These studies all find that the outer S layers are the most significant to the sliding potential. We confirmed this in the previous chapter by direct comparisons of few layers against bulk. The registry index method has been applied to MoS_2 [18, 22] and other layered materials as a lower computational cost approach than DFT.

7.2 Methodology

7.2.1 Parametrization

Our parametrization of ReaxFF was trained by straining bulk 2H-MoS$_2$ (uniaxially, biaxialy, triaxially, and with in-plane shear) and by simulating relative sliding of the layers along the basal plane. These computations were repeated once for each of the four dopant sites starring in previous chapters: Mo substitution, S substitution, octahedral (o-) intercalation, and tetrahedral (t-) intercalation. The force field was then validated by using the relaxed bond lengths, lattice parameters, and by computing defect site stability.

In this parametrization process, two sets of data are created using DFT—a training set to find appropriate energy weights and a testing set to evaluate the accuracy of the potential. During parametrization, errors are computed between the energies of DFT and ReaxFF as $Error = (\frac{E^{\text{ReaxFF}} - E^{\text{DFT}}}{w})^2$ for identical structures. w is relative weights.

The ReaxFF potential we use is as follows:

$$E_{\text{system}} = E_{\text{bond}} + E_{\text{o.c.}} + E_{\text{angle}} + E_{\text{dih}} + E_{\text{vdW}} + E_{\text{Coulomb}} \tag{7.1}$$

With respect to bonding, E_{bond} varies with interatomic distance and is related to bond formation, while $E_{\text{o.c.}}$ penalizes overcoordination. E_{angle} and E_{dih} are related to 3- and 4-body angle strains. E_{vdW} is the important van der Waals term which dominates the MoS$_2$ interlayer interaction and E_{Coulomb} is the electrostatic contribution.

7.2.2 DFT

As in our previous work on thermodynamics and vibrational properties of Ni-doped MoS$_2$ [58], the plane-wave density functional theory (DFT) code Quantum ESPRESSO [50] was used for quantum-level calculations. The Perdew-Burke-Ernzerhof [139] (PBE) generalized gradient approximation was used with Grimme-D2 [53] van der Waals correction, and the electron-ion interaction was described with Optimized Norm-Conserving Vanderbilt pseudopotentials [153] parametrized by Schlipf and Gygi [187]. All DFT computations used a kinetic energy cutoff of 60 Ry. PBE + Grimme-D2 has been shown to accurately compute the lattice parameters, elastic constants, and phonon frequencies of MoS_2 [58].

The training set was composed of pristine 2H-MoS_2 supercell sizes of $2 \times 2 \times 1$, where the third direction is the one perpendicular to the layers. Pristine 2H-bulk structures have 6 atoms per unit cell and a half-shifted k-grid of $4 \times 4 \times 4$ was used. The pristine a- and c- vectors relaxed to 3.19 Å and 12.40 Å, respectively. The dopant sites were chosen because they are meta-stable; other sites such as intralayer interstitial or S-S bridge intercalation, would relax to other structures. The stable doped structures (Mo substitution, S substitution, and intercalation at the tetrahedral (t-) and octahedral (o-) sites) were computed using a $2 \times 2 \times 2$ supercell of the pristine structure. Bilayer calculations used identical parameters except for large c-parameters and only one k-point in the z-direction.

7.3 Results

Full discussion of the process and results can be found in the prepint when available [116]. The sample figures shown here capture two types of data. For the first in Fig. 7.1, the potential was trained explicitly to capture the strain response. We included very large strain values to hopefully capture the scenarios which may be present in sliding under heavy load. Overall, the potential follows the training set well except for the most extreme strains.

Bond lengths in Table 7.1 are an emergent quantity that we did not explicitly train. Ni-S bonds show good agreement between both computational methods. The Ni-Mo distance is substantially different in the S-substituted case. This may be due to Ni's tendency to prefer the other sites, as S-substituted has the highest formation energy.

Sliding potentials have thus far not been captured well. It was originally set as testing data, but we have thus turned it into training data to assure that the potential will capture sliding accurately.

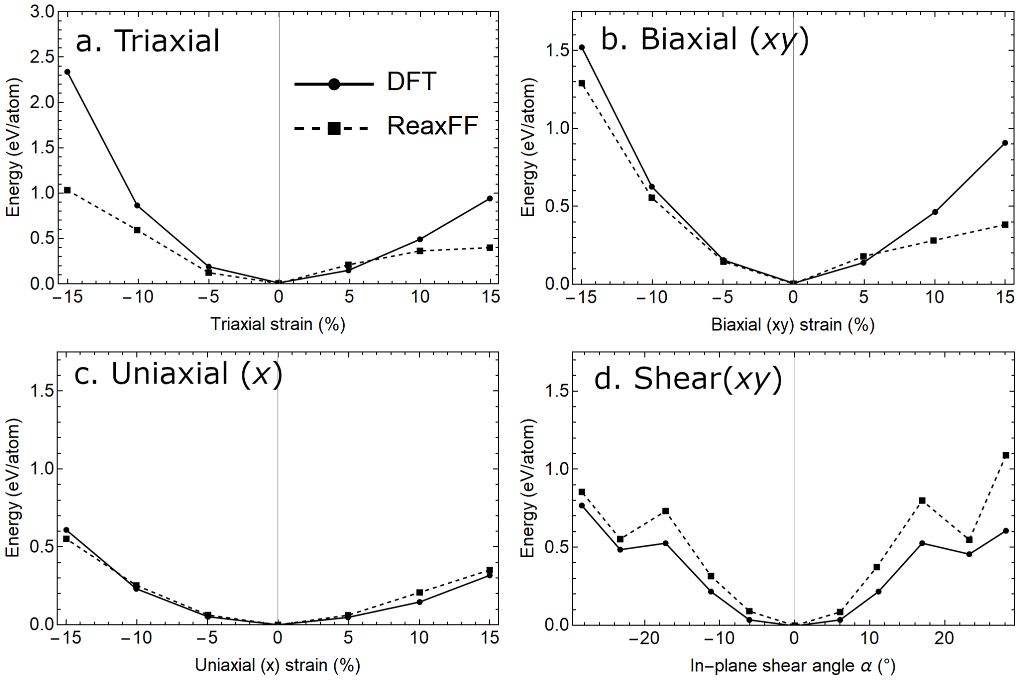

Figure 7.1: Performance of the ReaxFF potential against its own DFT training set under a. triaxial, b. biaxial, c. uniaxial strains or d. in-plane shearing of undoped MoS_2. Note a. has a larger energy scale than others. Uniaxial strain-energy is captured most accurately, but shear-strain is not captured well.

Table 7.1: Ni-S bond lengths compared between the two computational types.

Structure	DFT (Å)	ReaxFF (Å)
Mo-sub	2.38	2.32
S-sub*	2.55	2.75
Octahedral	2.34, 2.38	2.30, 2.40
Tetrahedral	2.12, 2.17	2.14, 2.30

They are mostly accurate to within 0.05 Å, except for the Ni-Mo bond length and the tetrahedral single bond. *S-substitution used Ni-Mo bonds instead of Ni-S.

7.4 Conclusion

We have generated a training set of data for ReaxFF. The structures were generated based on previous work as the starting structures, but they were then subjected to heavy strains. Testing has thus far not yielded accurate sliding in cases except for Mo-substitution and pristine, but it has shown accurate structural parameters—namely the bond lengths and lattice constants. Refining the parametrization should yield fast and accurate sliding simulations.

Chapter 8

Re-Doped MoS_2: Structure, Stability, and Vibrational Spectroscopy

Chs. 8 and 9 were initially inspired by a collaboration with the Baykara group at UC Merced. Their experiment [1] finds interesting tribological properties of Re-doped MoS_2. This section focuses on establishing the structure of Re-doped MoS_2 and does not yet connect with their work (Ch. 9 connects with that work directly). A significant finding of this work is a new way to compute the Raman spectra of a material with metallic qualities. This can work for a material which is nearly identical to a non-metal, such as how Re-doped MoS_2 is almost the same as pristine MoS_2, which is a semiconductor.

8.1 Abstract

Doping MoS_2 with Re is known to alter the electronic, structural, and tribological properties. Re-doped MoS_2 has been mainly studied in monolayer or few-layer form, but can also be relevant for applications in many-layer or bulk form. In this work, we use density functional theory to explore the structure, phase stability, and Raman spectrum of bulk Re-doped MoS_2. We consider the possibility of the Re dopant existing at different locations and provide experimentally distinguish-

able characteristics of the most likely sites: Mo-substitution and tetrahedral (t-) intercalation. We demonstrate and benchmark an approach to calculate Raman spectra of doped materials with metallic densities of states by using atomic Raman tensors from the pristine material. Applying this method to the metallic Re-doped structures, we find characteristic shifts in the Raman-active peaks depending on Re dopant position: redshifts in both $\mathrm{A_{1g}}$ and $\mathrm{E^1_{2g}}$ peaks in the t-intercalated case versus a redshift for $\mathrm{A_{1g}}$ and blueshift (sometimes accompanied by a smaller redshifted peak) for $\mathrm{E^1_{2g}}$ peaks in the Mo-substituted case, which can be used to identify the dopant sites in experimental samples. We analyze the interactions giving rise to these shifts.

8.2 Introduction

MoS_2 is a versatile semiconductor having an anisotropic, two-dimensional structure, with interesting electronic [11], optical, tribological [191, 144], catalytic [111], and spintronic properties [151]. Doping has been used as a strategy to tune these properties for applications of interest. Re is one of the most studied MoS_2 dopants [36, 2, 218], having one more *d*-electron than Mo and making MoS_2 *n*-type [61]. It can be incorporated by various synthesis methods [2, 48, 47, 107, 211] and also occurs as a natural impurity in MoS_2 [19]. Most of the recent interest in Re-doped MoS_2 system has been in single-layer structures [226, 179], with few multilayer or bulk studies [61, 2]. The bulk is also interesting in that it shares some of the optoelectronic properties and is the limit of trends in increasing layers. It is also important in macroscale applications such as solid lubrication [191, 1].

MoS_2 is an effective solid lubricant owing to the ease of shearing along the basal planes [191]. Doping MoS_2 alters material growth patterns [90] and enhances tribological properties [170]. Frictional forces on MoS_2 have been measured by AFM, and generally friction decreases with more layers, as for other 2D materials [99]. Surprising opposite trends in friction have been measured for Re-doped MoS_2 however, in a recent AFM study which we interpreted with theoretical calculations on friction and elastic stiffening by the dopants [1]. This work gives background on the basic properties of structures of Re-doped MoS_2.

The consensus in the literature is that Re in monolayer MoS_2 substitutes for Mo, which previous works have indicated with annular dark-field imaging [47, 107] and scanning atomic tomography [179] experiments, as well as calculations of formation energy [36] and consideration of the general chemical similarity between Mo and Re. In bulk, neighboring layers allow for the possibility of intercalation also. The favored site is unclear and has not been established by experiments, which are not necessarily able to distinguish between the sites in a multi-layer structures. In particular, there is some experimental evidence of intercalation from Raman spectroscopy interpreted by our density-functional theory (DFT) calculations [1], and energy dispersive x-ray analysis on samples from chemical vapor transport (though for a phase identified as 3R and not 2H) [180]. Moreover, DFT studies indicate the stability of other transition metals in tetrahedral (t-) intercalation [58, 70], making this and other possibilities worth investigating.

Raman spectroscopy is a key characterization method for 2D materials, and can be used to probe differences in microstructure—particularly local bonding configurations [58]. Doping MoS_2 with Re (as with other dopants) can shift the pristine Raman-active E^1_{2g} and A_{1g} peaks. The experimental literature has found different magnitudes and directions of these shifts in monolayer Re-doped MoS_2: redshifts in the A_{1g} peaks [2, 179, 48], redshifts of the E_{2g} peak [2, 48, 103, 210], or blue shifts in the E_{2g} peak [48]. The interpretation in terms of Re sites has been unclear and not investigated in detail, and has generally been vaguely attributed to overall strengthening or weakening of bonds by doping [68]. Calculation of Raman spectra in such systems poses a problem, because of new states at the Fermi level compared to the pristine system. The resulting metallic density of states cannot be handled by the typical DFT methods in the static approximation [97], despite the Raman spectra being physically observable. To overcome this, we develop an method to approximate the Raman tensor and thus obtain a Raman spectrum.

In this work, we investigate the structure and bonding of bulk Re-doped MoS_2, showing the phase stability that leads us to two structures of interest—the t-intercalated and Mo-substituted sites. Our Raman calculations find clear differences between intercalated and Mo-substituted Re-doped MoS_2, with redshifts of both peaks in the intercalated case and a blue- and red-shift of the E^1_{2g} and A_{1g} respectively in the Mo-substituted case, which can be experimentally identifiable features. To accomplish these Raman computations, we propose a method to estimate the Raman tensor for a metallic doped system, and benchmark its accuracy.

8.3 Methods

We use plane-wave DFT and density functional perturbation theory [6] (DFPT) implemented in `Quantum ESPRESSO` [50] version 6.6. Calculations were performed using either the Perdew-Burke-Ernzerhof [139] (PBE) generalized gradient approximation with the Grimme-D2 (GD2) [53] van der Waals correction, or the Perdew-Wang [138] local density approximation (LDA). We use ONCV pseudopotentials [153] parametrized by PseudoDojo [187].

PBE+GD2 yields slightly better structural parameters than LDA [58]. Unlike PBE, LDA is compatible with `Quantum ESPRESSO`'s implementation of Raman intensities, so we decided to use LDA for vibrational spectra (including initial structure optimization) and use PBE+GD2 otherwise. 60 Ry was used as the kinetic energy cutoff for PBE while 80 Ry was used for LDA—a higher cutoff was required for more accurate phonon modes in DFPT but not required for reasonable structural optimization. We applied 0.001 Ry Gaussian smearing to the electronic occupations to be able to handle metallic structures. Electronic energy, force, and pressure thresholds of 10^{-6} Ry, 10^{-4} Ry/Bohr, and 0.005 GPa were used respectively in variable-cell relaxations.

We model Re-doped MoS_2 with charge-neutral periodic supercells, using increasing supercell sizes to test the dependence on Re concentration and approach the low-doping limit, as summarized in Table 8.1. We tested the effect of out-of-plane dopant interactions on some properties using the $2 \times 2 \times 2$ supercell. Electronic density of states calculations used 0.1 eV broadening, and 20% additional unoccupied states. All k-grids are half-shifted. An exception is the $3 \times 3 \times 1$ t-intercalated structure which was numerically troublesome and used 15% unoccu-

Table 8.1: Supercell parameters.

supercell	Re concentration	scf k-grid	DOS k-grid
$2 \times 2 \times 1$	4.17 at-%	$6 \times 6 \times 2$	$8 \times 8 \times 4$
$2 \times 2 \times 2$	2.08 at-%	$6 \times 6 \times 1$	$8 \times 8 \times 2$
$3 \times 3 \times 1$	1.85 at-%	$3 \times 3 \times 2$	$6 \times 6 \times 4$
$4 \times 4 \times 1$	1.04 at-%	$2 \times 2 \times 2$	-

pied states and a Γ-centered grid to converge successfully.

Spin-polarized calculations were used for relaxations since Re doping introduces an odd number of electrons and so there is the possibility of magnetization. Magnetization has been observed [210] in 1T Re-doped MoS_2 and predicted in monolayers [226]. However, energy differences between spin-polarized and spin-unpolarized states are roughly 10^{-5} eV per atom (Table 8.2) and so we conclude that magnetism is not significant for the computed values in this system. Moreover, our computational treatment of Re-doped MoS_2 as a periodic supercell likely overestimates the magnetic effects compared to the probable disordered Re distributions in a real sample. Because of this, we included magnetization when it was feasible (relaxations and total energy for phase diagrams) but used spin-unpolarized calculations for vibrational spectra, which are sensitive to small energy differences.

8.4 Results and Discussion

8.4.1 Structure and Bonding

We consider the following possible Re dopant sites: Mo substitution, S substitution, t-intercalation, octahedral (o-) intercalation, Mo-Re split interstitial (similar to the Mo-Mo split interstitial from Komsa and Krasheninnikov [89]), bridge-site intercalation, and hollow-site intercalation. These structures were chosen as they

Table 8.2: Magnetization for Re-doped MoS_2 supercells from PBE+GD2, and energy differences between the spin-polarized and spin-unpolarized states.

s.c.	Mo subst.		S subst./ S vac.+Re		o-intercal.		t-intercal.		Re-Mo interst.	
	μ	ΔE	μ	ΔE	μ	ΔE	μ	ΔE	μ	ΔE
$2 \times 2 \times 1$	0.00	0	0.67	5.5	0.00	0	0.00	0	0.33	4.4
$2 \times 2 \times 2$	0.00	0	0.00	0	0.00	0	0.00	0	0.00	0
$3 \times 3 \times 1$	0.33	3.1	3.00	84.2	1.00	4.1	0.00	0	1.00	45.9
$4 \times 4 \times 1$	0.00	0	3.00	116.0	0.00	0	1.00	18.0	1.00	18.0

μ in μ_B and ΔE are in meV, both per Re atom (one per cell); structures as defined in Fig. 8.1.

are commonly considered in computational studies of MoS_2 doping [70, 89]. The bridge and hollow sites are unstable and relaxed to o-intercalation, and are not considered further. The relaxed structures are pictured in Fig. 8.1. We focused on three structures: undoped 2H-MoS_2, Mo-substituted, and tetrahedral-intercalation (t-intercalated). All structures retained a 2H structure and we found no evidence of shifting to, for example, the 1T phase as has been obtained in some experimental studies [210, 39]. There is one exception – the t-intercalated $3 \times 3 \times 1$ (with PBE+GD2) relaxed to a structure (see Fig. 8.8) with the Mo atoms aligned above one another, in which the Re atom now has octahedral bonding to S atoms. This corresponds to aBa cBc stacking (using the convention in Song *et al.* [162]), similar to the "Min 2" structure from sliding in Levita *et al.* [101]. This structure is lower in energy by 0.02 eV per atom than if it had the typical stacking.

The pristine structure has $a = b = 3.190$ Å, $c = 12.415$ Å, $\alpha = \beta = 90°$ and $\gamma = 120°$, as shown in Fig. 8.1. For most of the computed structures, the lattice parameters match the pristine to within 0.5%. There is a 1-2% increase in c in t-intercalation, consistent with a previous calculation [61] and similar to results for Ni [81] but considerably less than the increase in layer spacing for Li [38]; the anomalous $3\times3\times1$ structure shows a lesser increase in c. The split interstitial shows

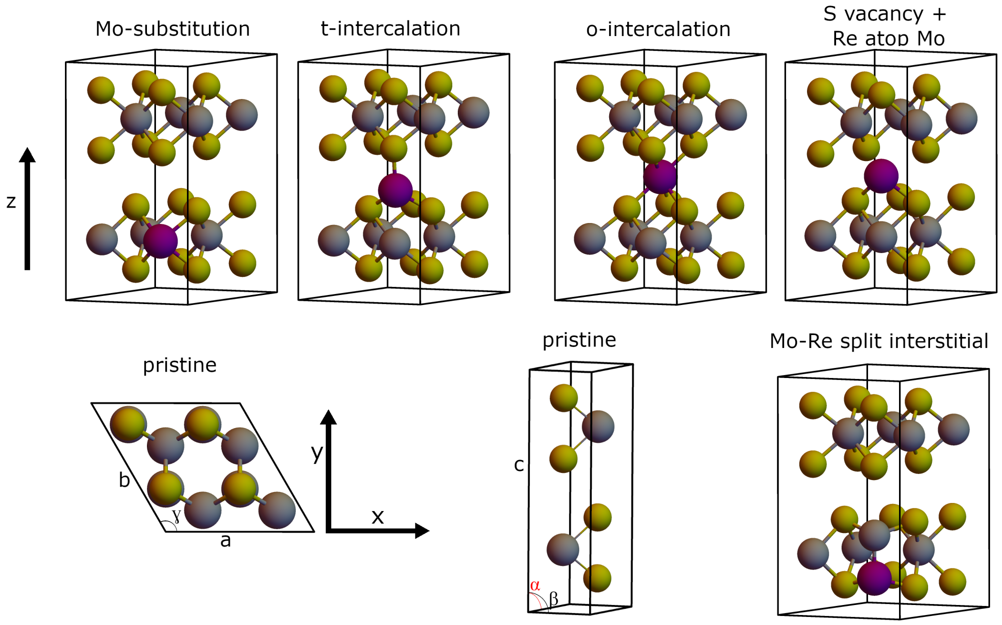

Figure 8.1: Re-doped MoS_2 structures found to be stable or metastable: Mo in gray, S in yellow, and Re in purple.

a 0.5-2.5% increase in a and b. The 2×2×1 and 2×2×2 S-substituted structures show a substantial change in structure when relaxed—they are better described as a S vacancy with a Mo-atop Re dopant, as in Fig. 8.1. This is visible in the charge densities in Fig. 8.2. 3×3×1 and 4×4×1 show 2% and 1% reductions in c, respectively. Angles are within 0.05% of the pristine with few exceptions. The t-intercalated α and β are 0.4%, 0.2%, and 8.2% larger (smaller) than the pristine α (β) for 2×2×1, 2×2×2, and 3×3×1 respectively. In the Mo-substituted case, there is a noticeable local symmetry-breaking around the Re atom, leading to Re-S bonds in two groups measuring about 2.38 Å and 2.41 Å respectively at a 3×3×1 supercell. O-intercalation's 6 bonds, due to the symmetry of the site, occur in two or three groups with differences of around 0.005 Å in bond length. Full structural information is found in Table 8.4.

Analysis of the electronic density demonstrates that Re is able to form interlayer covalent bonds, as shown by significant electronic density between Re and S across layers in Fig. 8.2(c,d): comparable to, or even larger than, the electronic density in Mo-S bonds. This happens in o- and t-intercalation, as for Ni [58]. While

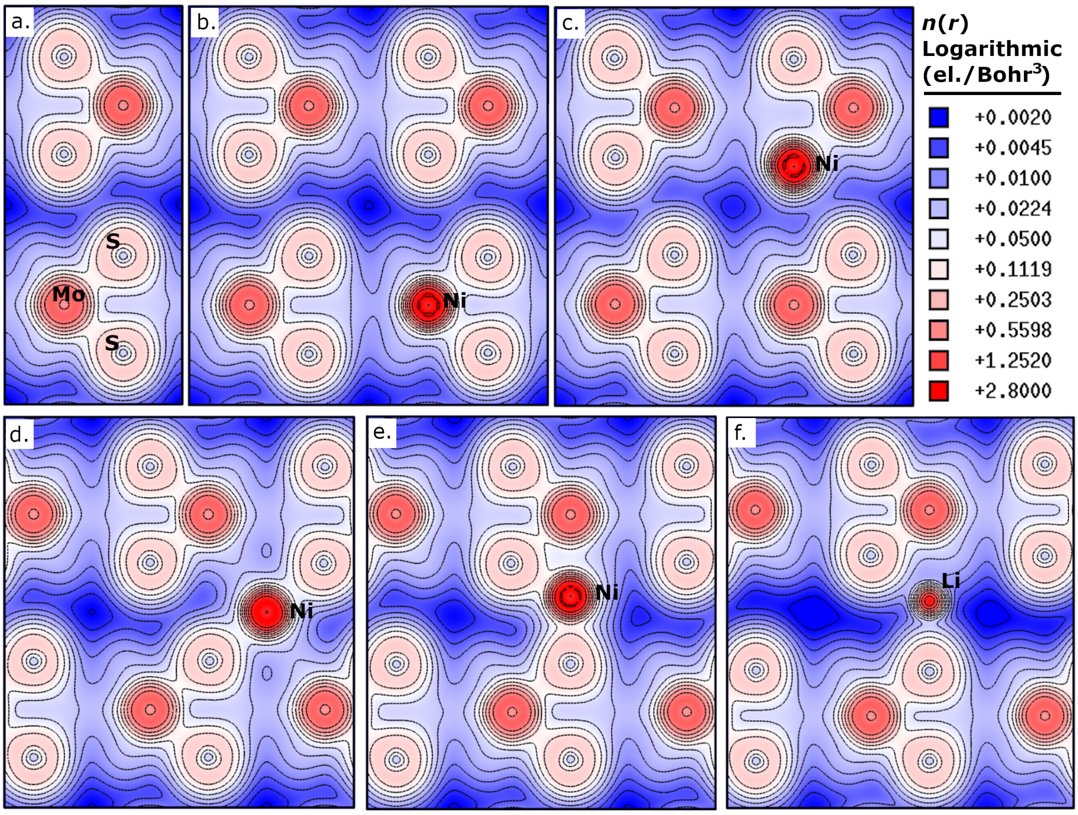

Figure 8.2: Electronic densities of MoS_2: a) pristine, b) Mo-substituted, c) t-intercalated, d) o-intercalated, e) S vacancy + Re atop Mo, and f) split-interstitial, in cross-sections of the 2 × 2 × 1 supercell in an Mo-S plane close to the dopant. S atoms are shown in yellow, Mo atoms are in gray, and Re atoms are purple. Intercalated and S-vacancy structures show strong out-of-layer bonding. All structures besides the highly distorted S vacancy structure show densities in the Re-S bonding region to be as strong as Mo-S bonds.

Mo-substitution is nearly indistinguishable from pristine in its electronic density, there is a slight increase in the density in the S-bonding region in both layers of the Mo-substituted structure. Re's presence in other cases reduces the electronic density in the region between two S atoms in the same layer. Intercalated Re also reduces electronic density between S atoms it is bonded and their adjacent Mo atoms, suggesting a weakened bond. The non-intercalated doped structures however show only van der Waals interactions between layers.

8.4.2 Thermodynamic Stability

With the method we previously used for Ni-doped MoS_2 [58], we compute the phase diagram, marking the most stable structure at a given chemical potential. The relative stability of structures with different stoichiometries can be analyzed using the formation energy:

$$E_{\text{formation}} = E_{\text{mixed}} - \sum_i N_i E_{i,\text{bulk}} - \sum_i N_i \mu_i \tag{8.1}$$

where the energies are referenced against stable bulk elemental phases of Mo, S, and Re.

These computations require the energies and composition of different phases of Re, Mo, and S compounds. We used the set of stable and metastable structures we found: Mo substitution, S substitution, t-intercalation, o-intercalation, and the Mo-Re split interstitial. O-intercalation, t-intercalation, and Mo-Re split interstitial have the same chemical composition and thus their energies are directly comparable. Of these, t-intercalated consistently has a lower energy by 0.01–0.02 eV/atom. There is one exception: the 4 × 4 × 1 split-interstitial is very slightly energetically favorable over either intercalated structure by 0.001 eV/atom. Full formation energies are given in Table 8.5.

The T=0 K phase diagram (Fig. 8.3) shows that the Mo-substituted structure is the most stable and the only structure consistent with stability of pristine MoS_2. This result is consistent with experimental observation of Mo-substituted monolayers [107], which have a comparable geometry. While Re adatoms on monolayers are much less stable, bulk intercalation of Re has been inferred in experimental samples [1], which can be due to out-of-equilibrium or higher-temperature synthesis processes. The picture is quite different from that for Ni-doping of $\mathrm{MoS_2}$, in which only t-intercalation was compatible with pristine $\mathrm{MoS_2}$ stability (except at the highest doping levels) [58]. Phase stability at higher temperature can be estimated in the harmonic approximation by calculating the lattice vibrations' contributions to the free energy [89] $F = E - TS$, using the entropy

$$S(T) = k_B \sum_{\lambda} n_B(\hbar\omega_\lambda, T) \ln n_B(\hbar\omega_\lambda, T) \tag{8.2}$$

with Bose-Einstein populations n_B and phonon frequencies ω_λ. The lowest-frequency modes contribute most to this term, namely the acoustic modes as well as shearing $\mathrm{E}_{2\mathrm{g}}^2$-like (35.2 cm^{-1} in pristine) and layer-breathing $\mathrm{B}_{2\mathrm{g}}^2$-like (55.7 cm^{-1} in pristine) modes. Compared to Mo substitution, t-intercalation has a 6–10 cm^{-1} lower frequency in the $\mathrm{E}_{2\mathrm{g}}^2$-like mode but a 5–20 cm^{-1} higher frequency (*i.e.* stiffer atomic vibrations) in the $\mathrm{B}_{2\mathrm{g}}^2$-like mode. Throughout most of the Brillouin Zone, the $\mathrm{E}_{2\mathrm{g}}^2$-like modes are the lowest in frequency, below even the acoustic modes, and will be significantly populated at room temperature ($k_BT \sim 200$ cm^{-1}). Therefore this mode can contribute considerably to the free energy. Since this mode is lower in energy for t-intercalation, it will contribute to a more negative entropy for t-intercalation *vs.* Mo substitution, and at high temperatures the free energy could favor t-intercalation, making it accessible even within the pristine stability triangle in Fig. 8.3.

8.4.3 Raman spectra

The standard approach to Raman spectra in DFPT [97] calculates atomic Raman tensors via electric-field and atomic-displacement perturbations, and then combines these with phonon eigenvectors to obtain the Raman intensities of phonon modes. The formalism is based on the Placzek approximation and a static approximation for the dielectric constant ϵ^∞, which is typically valid for sub-gap

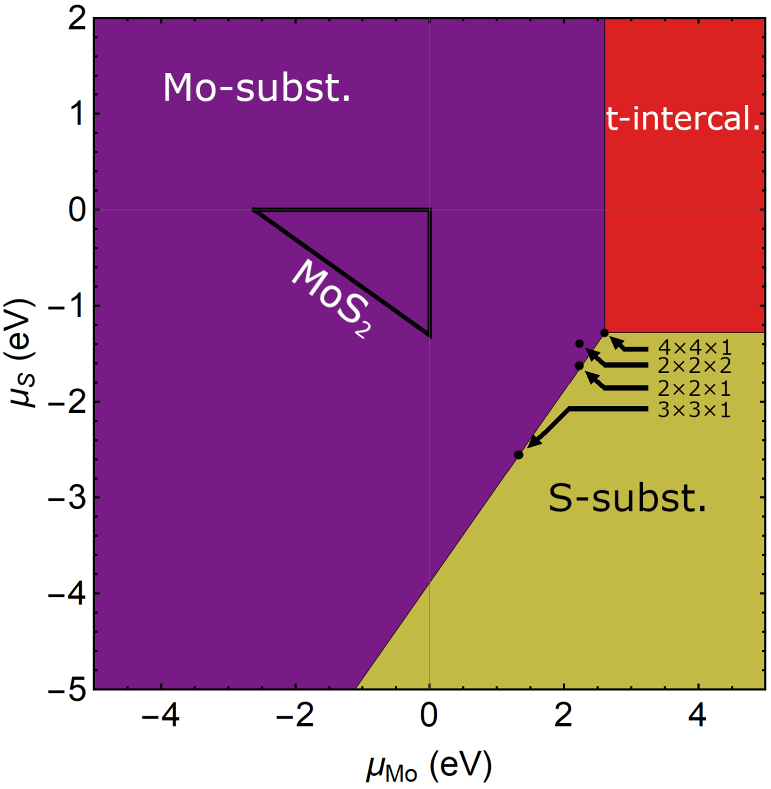

Figure 8.3: The $T = 0$ K phase diagram for Re-doped MoS$_2$ in a 4×4 supercell. Only the Mo-substituted Re-doped MoS$_2$ falls within the stability triangle (black) for MoS$_2$ (as in Guerrero *et al.* [58]). The labeled dots show the location of the intersection point for other supercell sizes. The pristine MoS$_2$ line meets the axes at $\mu_S = -1.308$ eV and $\mu_{Mo} = -2.616$ eV. Structures considered include Mo-substituted, S-substituted, tetrahedral intercalation, octahedral intercalation, and the Mo-Re split interstitial. Note that for $4 \times 4 \times 1$ the Mo-Re split interstitial has essentially the same energy as t-intercalation.

(non-resonant) incident light.

$$I_{i,s}^{\nu} \propto \left|\hat{e}_i \cdot A^{\nu} \cdot \hat{e}_s\right|^2 \frac{1}{\omega_{\nu}} \left(n_{\mathrm{B}}\left(\hbar\omega_{\nu}, T\right) + 1\right) \tag{8.3}$$

where $I_{i,s}$ is the intensity for incident direction i and scattered direction s, ν is a mode index, A_{ν} is the mode Raman tensor, and ω_{ν} is the phonon frequency. The mode Raman tensor is calculated in terms of atomic Raman tensors $A_{lm}^{k\gamma}$:

$$A_{lm}^{\nu} = \sum_{k\gamma} A_{lm}^{k\gamma} \frac{w_{k\gamma}^{\nu}}{\sqrt{M_{\gamma}}} \tag{8.4}$$

$$A_{lm}^{k\gamma} = \frac{\partial^3 U^{el}}{\partial E_l \partial E_m \partial u_{k\gamma}} = \frac{\Omega}{4\pi} \frac{\partial \epsilon_{lm}^{\infty}}{\partial u_{k\gamma}} \tag{8.5}$$

where w^{ν} is the displacement pattern of mode ν; k, l, and m are Cartesian directions, γ is an atom index, M_{γ} is the atomic mass, Ω is the unit cell volume, U^{el} is the electronic energy, u is an atomic displacement, and E is the electric field. Clearly this approach is only meaningful when a finite ϵ^{∞} can be defined. Metallic systems, i.e. those without a bandgap, cannot be calculated because of the divergence of the dielectric constant in this case. Practically speaking, any system treated with smearing in `Quantum ESPRESSO` falls in this category.

True metals generally do not have observable Raman intensity because light will be reflected rather than undergoing Raman scattering, due to a large ϵ^{∞} at the incident frequency; exceptions are Feldman et al. [41] and a recent work on Cu surfaces [33]. Doped semiconductors however do typically show Raman intensity, in particular for low doping concentration and therefore typically a low density of states at the Fermi level. The metallic nature in a small supercell calculation may be due to spurious formation of impurity bands. Moreover, n-type doping as for Re-doped MoS_2 in a low-doping limit is expected to leave the bandgap intact and simply move the Fermi level into the conduction bands, as in Hallam *et al.* [61] In this case, the dielectric constant remains finite at the optical frequencies of incident light for Raman experiments. Indeed this is exactly the situation sought for transparent conductors [20]. In our calculation, all the t-intercalation and Mo substitution supercells have metallic density of states (Fig. 8.4). Given the small supercells we use to make Raman calculations tractable, we do see significant modification of the density of states, including in-gap states, rather than simply electron donation.

We also note that many works have reported Raman scattering measurements from Re-doped MoS_2 [1, 61], so there should be a way to obtain these Raman tensors theoretically. Rather than use prohibitively large supercells and/or perform computationally intensive resonant Raman calculations (e.g. using time-dependent DFT or the Bethe-Salpeter equation [200]), we develop an alternate approach based on the approximation that the atomic Raman tensors are similar to those of pristine MoS_2 and/or a similar reference system which has a well-defined gap and can be calculated in the usual way. We use directly calculated phonon displacement patterns and simply substitute the atomic Raman tensors from the reference system in Eq. 8.4. In practice, this is done by inserting the reference atomic Raman tensors from the undoped case into the files `Quantum ESPRESSO` uses to compute the Raman intensities. Individual Mo and S atoms are matched to their counterparts in a pristine structure. There are several plausible options for the dopant atom: approximation as Mo, approximation as another dopant from a similar system, or neglect as zero, which we test below. Our method could also be applied to materials with very large numbers of atoms per unit cell, such as amorphous materials; the phonon modes may be computed by classical force fields to save computational effort, while the tensor could use DFT methods. Atomic Raman tensors can be rotated when atoms appear with a different orientation of bonds, along the lines of Raman bond-polarizability models [204].

Our scheme is related to a more limited approach taken in recent work [63, 91], in which the Raman *intensities* from a reference system are used to calculate Raman spectra of a doped system, to avoid the need for explicit calculations on the doped system. It can be derived by projecting the doped mode (ν) eigenvectors onto the pristine mode (μ) eigenvectors, giving coefficients $c_{\mu\nu}$, and expanding the

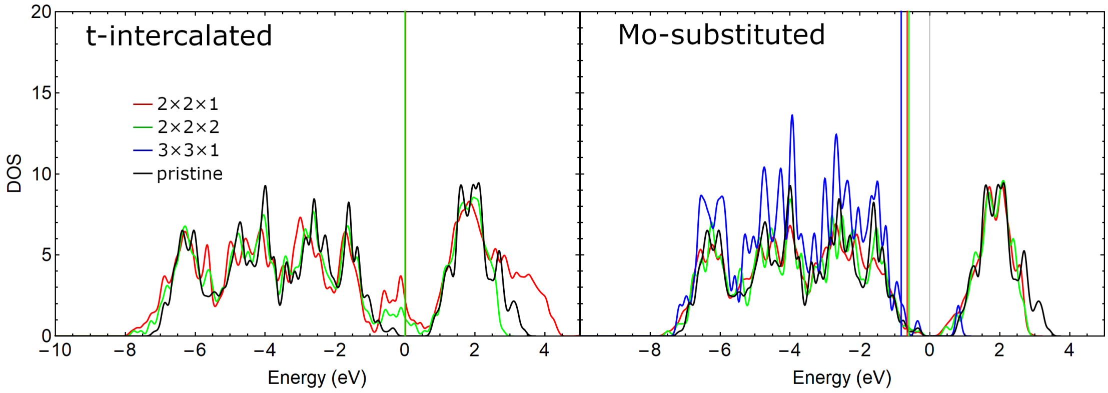

Figure 8.4: Electronic density of states (DOS) for Mo-substituted and t-intercalated structures (using the LDA relaxed structures, as in the Raman calculations). Energies are aligned to the lowest-lying Mo states. Vertical lines indicate the Fermi energies. All doped structures have nonzero DOS at the Fermi level.

Raman tensors accordingly in terms of those $\tilde{A}$ of the pristine reference system:

$$|\hat{e}_i \cdot A^\nu \cdot \hat{e}_s|^2 = |\hat{e}_i \cdot \sum_\mu c_{\mu\nu} \tilde{A}^\mu \cdot \hat{e}_s|^2 \tag{8.6}$$

$$= \sum_\mu c_{\mu\nu} \left(\hat{e}_i \cdot \tilde{A}^\mu \cdot \hat{e}_s \right) \sum_\sigma c^*_{\sigma\nu} \left(\hat{e}_i \cdot \tilde{A}^{\sigma *} \cdot \hat{e}_s \right) \tag{8.7}$$

$$\approx \sum_\mu |c_{\mu\nu}|^2 |\hat{e}_i \cdot \tilde{A}^\mu \cdot \hat{e}_s|^2 \tag{8.8}$$

Cross terms ($\mu \neq \sigma$) are neglected to reach Eq. 8.8. The intensity I can be written correspondingly in terms of the intensities $\tilde{I}$ of the reference system:

$$I^\nu_{i,s} = \sum_\mu |c_{\mu\nu}|^2 \tilde{I}^\mu_{i,s} \tag{8.9}$$

As in our method, only the phonon eigenvectors are needed for the system of interest, which could be computed by any means, including classical force fields. A key limitation is that working with only the scalar intensities means losing a significant amount of information about the Raman response; in particular, interference effects (the cross terms in Eq. 8.8) are neglected, which can be significant, in particular for the case of symmetry-breaking of a Raman-inactive mode into Raman-active modes.

We tested our method, and the intensity mapping of Eq. 8.8, on our previously computed $3 \times 3 \times 1$ supercell, t-intercalated, Ni-doped MoS_2 [58], which does not require smearing and can be handled by standard methods. We use Raman tensors for Mo and S from pristine MoS_2, and initially set the Raman tensor of Ni to zero. The relative peak heights are 15% below the full computation as shown in Fig. 8.5, and the peak height ordering is preserved. Compared to the intensity-based scheme, we see that our Raman-tensor treatment makes small improvements near the pristine Raman-active peaks of Ni-doped MoS_2 (around 380 cm^{-1} in Fig. 8.5). Both methods significantly underestimate the intensity of some modes which are highly local to the Ni (435 cm^{-1} and 470 cm^{-1}) due to lack of information about the distinctive contributions of these atoms, but are better at modes which contain both local components and pristine-like vibrations (452 cm^{-1} and 502 cm^{-1}).

We further found that by comparing structures with different choices for replaced Raman tensors against the pristine result, we can identify which peaks in the spectra are due to geometry changes rather than new Ni-bond related activity. In this case Ni introduces shifts to the active peaks, new peaks related to new modes local to the Ni, and activations of existing MoS_2 modes that were previously inactive by symmetry [58]. Our Raman tensor approximation method is versatile when distinguishing changes in the intensities as being caused by lattice distortions or charge transfer from doping. By setting to zero specific atomic components (e.g. those of the dopant and its nearest neighbor) we are able to analyze the effect of different atoms in the Raman scattering intensity. In Fig. 8.6, we test different approximation schemes for the Ni component of the atomic Raman tensor. Setting Ni and its nearest neighbors' (NN) contributions to zero is the most reductive approximation and is thus furthest from accurate—this is clearest in the muted shoulder of the E_{1g} peak. It is still useful, however, in interpreting the nature of modes such as the 505 cm^{-1} peak. The lack of intensity in the NN line means that activity of this peak is highly localized to the Ni atom. The approximation works well near the pristine-active peaks, but fails whenever the activity is localized around the Ni atom. The fact that the peak around 150 cm^{-1} has too *large* an intensity when these contributions are set to zero underscores the importance of interference effects in the Raman intensities, as captured by our approach. We can see the small effect of Ni-doping on the Raman tensors of Mo and S (neglected

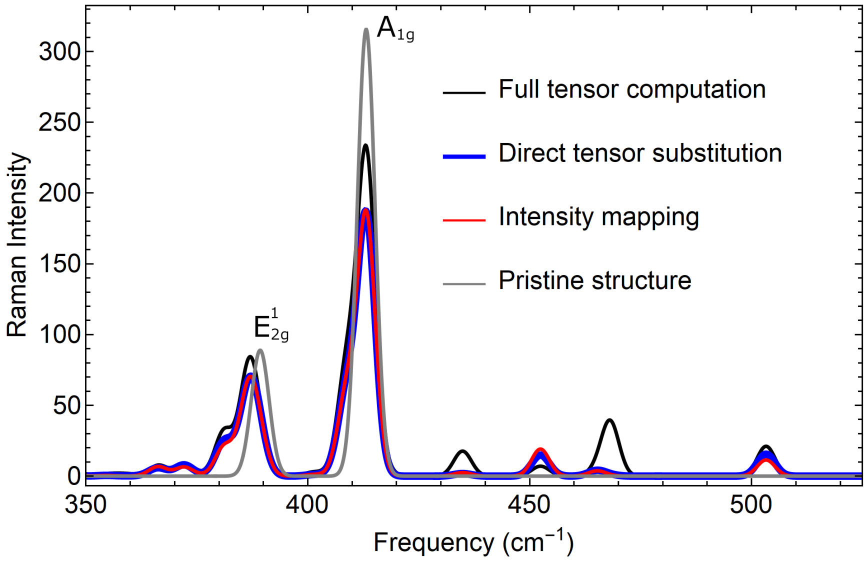

Figure 8.5: Raman spectra (Å^4/amu per MoS$_2$ unit) of t-intercalated Ni-doped MoS$_2$, comparing intensity approximations to a full tensor computed using the Lazzeri method [97] which is not possible with Re-doped MoS$_2$. The tensor substitution is a slight improvement when compared to the intensity mapping [63, 91] method. The spectra uses Gaussian smearing with a width of 4 cm^{-}1.

in our scheme), in the small difference between the full computation, and the approximation in which Mo and S tensors are from pristine and the Ni tensor is from the full computation. We see better agreement with the full computation when the Ni tensor is approximated as Mo then when it is set to zero; this ability to control contributions from the dopant atom is an advantage of our scheme over one using just intensities. Since altering just the Ni dopant's contribution does not change the pristine-active region much, we expect that this method can predict the Re-doped structures' spectra with little loss in accuracy in this frequency regime.

Now we turn to our main interest, the Re-doped case. As for Ni-doped MoS$_2$, the doped structure closely resembles the pristine structure, making our approximation reasonable. In Mo substitution, we approximate the Re tensor with Mo, and in t-intercalation, we approximate Re by the Ni tensor from t-intercalation in a $3 \times 3 \times 1$ supercell, as this is a transition metal in the correct bonding geometry. Raman spectra in the pristine-active frequency regime are plotted in Fig. 8.7. Complete IR, Raman, and vibrational density of states spectra are provided in

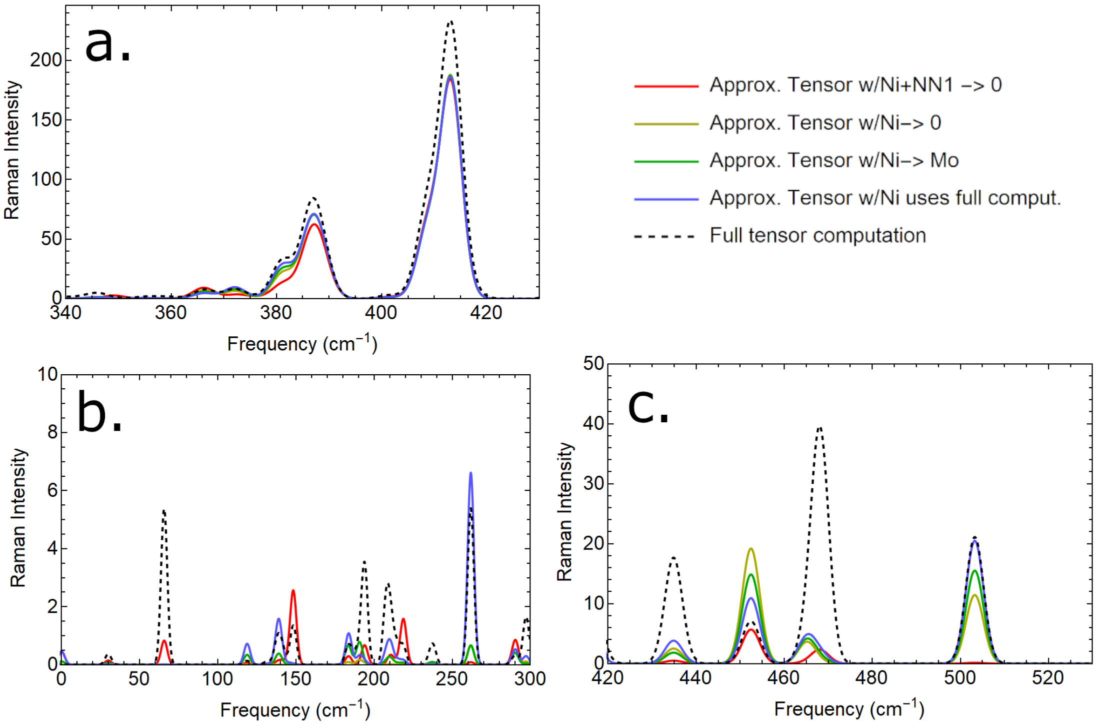

Figure 8.6: Comparison of the Ni-doped spectra for different approximations of the Ni atomic Raman tensor across three ranges in Å^4/amu per MoS$_2$ unit (note the different scale for the three plots). The Mo and S atoms use the same tensor as the pristine. For the red line, the Ni and its nearest neighbor (NN) S atoms' contributions to the Raman tensor have been set to 0. For the rest, the Ni atom's contribution only has been set to 0 (yellow), the same as Mo in pristine (green), and the same as the full computation (blue). The pristine-active modes (a) show the least amount of change, except on the shoulder of the E^1_{2g} peak. For the high-frequency modes (c), the 435 cm^{-1} and 470 cm^{-1} peaks are highly localized to the Ni and are not described well. At 505 cm^{-1}, the peak is entirely localized near the Ni and its NN, as evidenced by the lack of intensity when those contributions are removed.

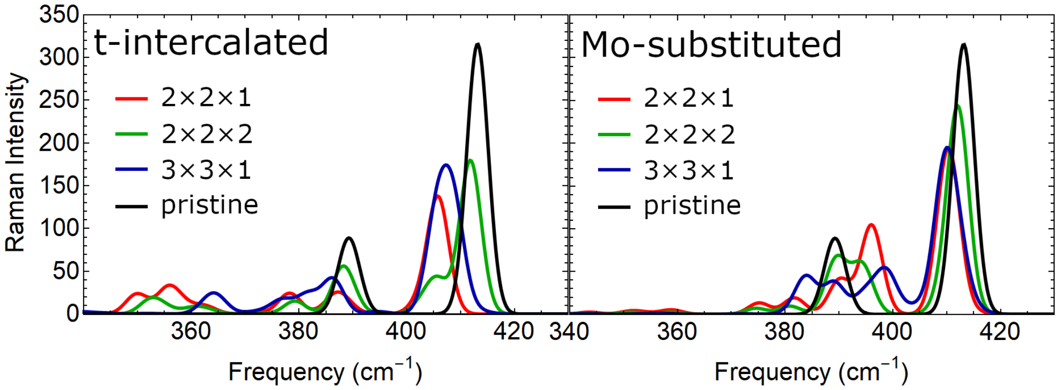

Figure 8.7: Raman spectra (in Å^4/amu per MoS$_2$ unit) of t-intercalated and Mo-substituted Re-doped MoS$_2$ as computed by DFPT with substitution of the Raman tensor by those in a pristine computation (Mo and Ni replace the Re atom's contribution in the Mo-substituted and t-intercalated respectively). The direction of the peak shifts is generally preserved among the supercell sizes used: redshifts in both peaks when t-intercalated and blue- and redshifts in the E^1_{2g} and A_{1g} peaks respectively while Mo-substituted. Gaussian broadening of 2 cm^{-1} was used.

Fig. 8.10. We find a consistent trend among the Mo-substituted and t-intercalated Re-doped Raman spectra for different supercells we computed: there is a redshift of both peaks in the t-intercalated case and blue- (E^1_{2g}) and red- (A_{1g}) shifts in the Mo-substituted case. The t-intercalated shifts are consistent with some experimental reports on multilayers [2, 48, 210] and monolayers [103], though the Raman spectra were not typically studied in much detail and A_{1g} shifts were not resolved except in Al-Dulaimi *et al.* [2]. Al-Dulaimi et al. [2] argued that a red shift of E_{2g} was a sign of Mo substitution in their sample, and the effect of a heavier mass of Re than Mo, but our results show that this interpretation is not correct since Mo substitution in fact blueshifts this peak. The agreement between intercalation and monolayers perhaps suggests adatoms on those monolayer samples. Another experiment on monolayer samples believed to be Mo-substituted [47] showed shifts consistent with our calculations for Mo substitution. The bulk Raman spectra of Hallam *et al.* [61] by contrast do not have the resolution to show any doping-induced shifts. Different synthesis methods and conditions can cause different doping sites (or distributions of sites) in their samples. It is worth noting that Z-contrast imaging [107] is often used to locate the Re dopant, but

Table 8.3: Vibrational frequency shifts for t-intercalated and Mo-substituted structures with respect to undoped MoS_2.

Dopant Site	Supercell	A_{1g} (cm^{-1})	E^1_{2g} (cm^{-1})
t-intercal.	$2 \times 2 \times 1$	-7.4	-2.0
t-intercal.	$2 \times 2 \times 2$	-1.3	-1.0
t-intercal.	$3 \times 3 \times 1$	-5.9	-3.2
Mo-subst.	$2 \times 2 \times 1$	-2.8	+6.8
Mo-subst.	$2 \times 2 \times 2$	-1.1	+0.7, +4.5
Mo-subst.	$3 \times 3 \times 1$	-3.1	-5.3, -0.34, +9.1*

* Appears near E^1_{2g} but actually more related to A_{1g} in character.

the basal (in-plane) position of the t-intercalated dopant is the same as the Mo or S site, depending on which side it is viewed from, and so this method cannot give a conclusive answer. We can compare our calculated shifts to our previous Raman calculations for Ni-doped MoS_2: in that case, both Mo-substitution and t-intercalation caused red shifts for both of the main Raman peaks, making it harder to use for experimental identification. In both cases, t-intercalation induces extra peaks around 450-500 cm^{-1}, but whereas Re Mo-substitution induces few new peaks below 400 cm^{-1}, there are many significant new peaks in that range for Ni.

Inspection of the phonon modes that contribute to the Re-doped spectra show that the Mo-substituted activity near 395 cm^{-1} is (surprisingly) more related to A_{1g} rather than E_{2g}. This means that the A_{1g} mode splits and both peaks are redshifted. The nature of the 395 cm^{-1} would have experimental signatures in polarized Raman. Redshifts in the t-intercalated case are supplemented by activations and mixing with the forbidden B_{2u} which has a slightly lower frequency. High-frequency vibrations of the Ni-atom exist above the A_{1g} peak (Fig. 8.10), but the (out-of-plane) A_{1g}-like vibrations are lower in frequency than the pristine—despite the increase in out-of-plane stiffness found in our calculations [1]. Comparing Mo-S interatomic force constants, those nearby the Re are lower in magnitude by about 25% than those farther from Re in the z-direction. This is consistent with the observation that Re-doping lowers the A_{1g} frequency in both cases. Magnitudes of force constants in the x- and z-directions are lower for t-intercalation than pristine by roughly 10%, but are not appreciably changed for Mo-substituted, which is consistent with the different effects on the (in-plane) E_{2g} frequency between the two dopant sites. The reduction in force constant is also consistent with the reduced Mo-S electronic density near Re for t-intercalation, indicating a weakening of the covalent bond (Fig. 5.2). We note the complexity of the interactions here between the dopant and different modes – quite different from the typical idea that doping simply increases or decreases bond strength and thus gives small shifts in modes that essentially retain their pristine character [68], or that shifts are due simply to the effect of the different mass of dopant atoms.

8.5 Conclusion

We have computed properties of bulk and few-layer Re-doped MoS_2 in different dopant configurations. We found that when intercalated, Re forms covalent interlayer bonds, and the tetrahedral geometry is most stable. In some cases, S-substituted structures rearrange into an S vacancy and Re adatom on the opposite layer. Mo-substitution is the most thermodynamically stable at equilibrium, though t-intercalation may be favorable at high temperature, and in general other structures can be formed out of equilibrium. These considerations of structure, bonding, and thermodynamics provide the basis for investigation of other properties such as friction and elasticity [1].

We developed a new efficient method to calculate the Raman spectra of metallic doped systems with an accurate approximation benchmarked on our previously calculated Ni-doped Raman spectra. The approach is easily performed in `Quantum ESPRESSO` by substituting atomic Raman tensors from a reference system. We find the t-intercalated Raman spectra shifts *vs.* the pristine in ways that are consistent with experimental literature on Re-doped MoS_2. The doped E^1_{2g} peak is less like the pristine peak than the A_{1g} peak in frequency and shape. The direction of the E^1_{2g} peak shift can be used to identify the dopant site in experimental samples—Mo-substitution shows blueshifts (and sometimes a smaller redshift as well) while t-intercalated shows redshifts. These features we have identified provide an avenue to distinguish the doping site in bulk phases which have been a challenge to identify experimentally [176, 191] and may be different from the well-studied monolayer. Importantly, we have shown that the relationship between doping and peak shifts is complex, as also elucidated in our work on Ni-doped MoS_2 [58]. The effect is not simply an overall strengthening or weakening of bond strengths by a dopant, but rather there are local effects around Ni, different effects on different bonds, interaction between different modes, and emergence of new dopant-related modes. In particular, a mode with frequency similar to E^1_{2g} turned out to be more related to A_{1g}. Continued *ab initio* study is needed to understand all the complexities of how dopants affect Raman spectra of 2D materials, and enable accurate interpretation of experimental spectra in terms of the electronic and structural effects of dopants.

8.6 Supplementary Materials

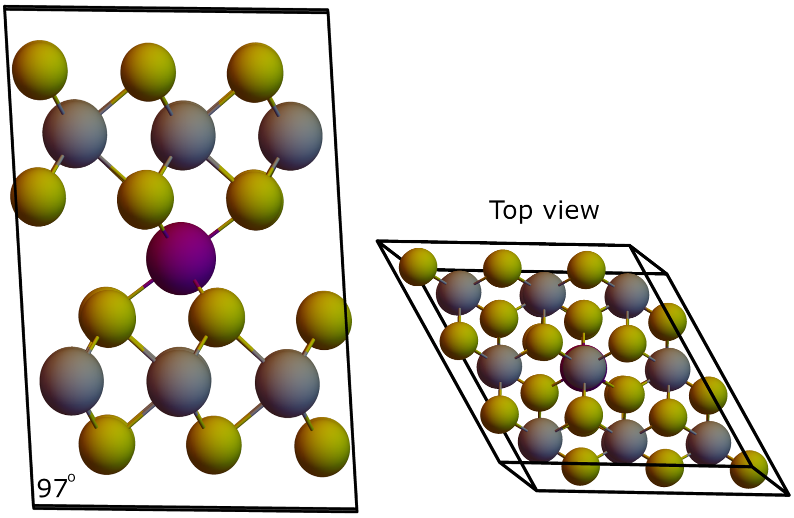

Figure 8.8: The anomalous 3 × 3 × 1 supercell t-intercalated structure with non-standard stacking. The cell has angles of 82.60°, 97.40°, and 119.99° and a stacking pattern typically seen as a metastable stacking configuration of pristine MoS_2.

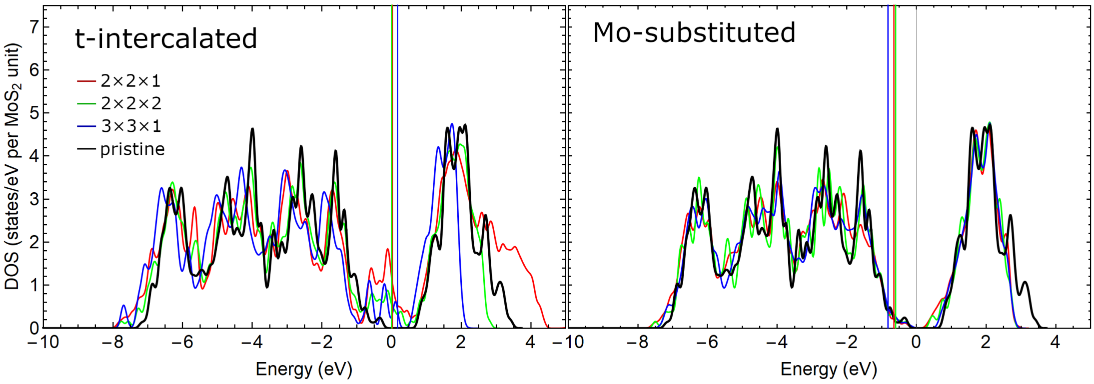

Figure 8.9: Electronic density of states (DOS) are computed for Mo-substituted and t-intercalated structures using the LDA configuration. The plots are aligned to the lowest lying Mo states. Vertical lines indicate the computed Fermi energies. All doped structures have nonzero DOS at the Fermi level.

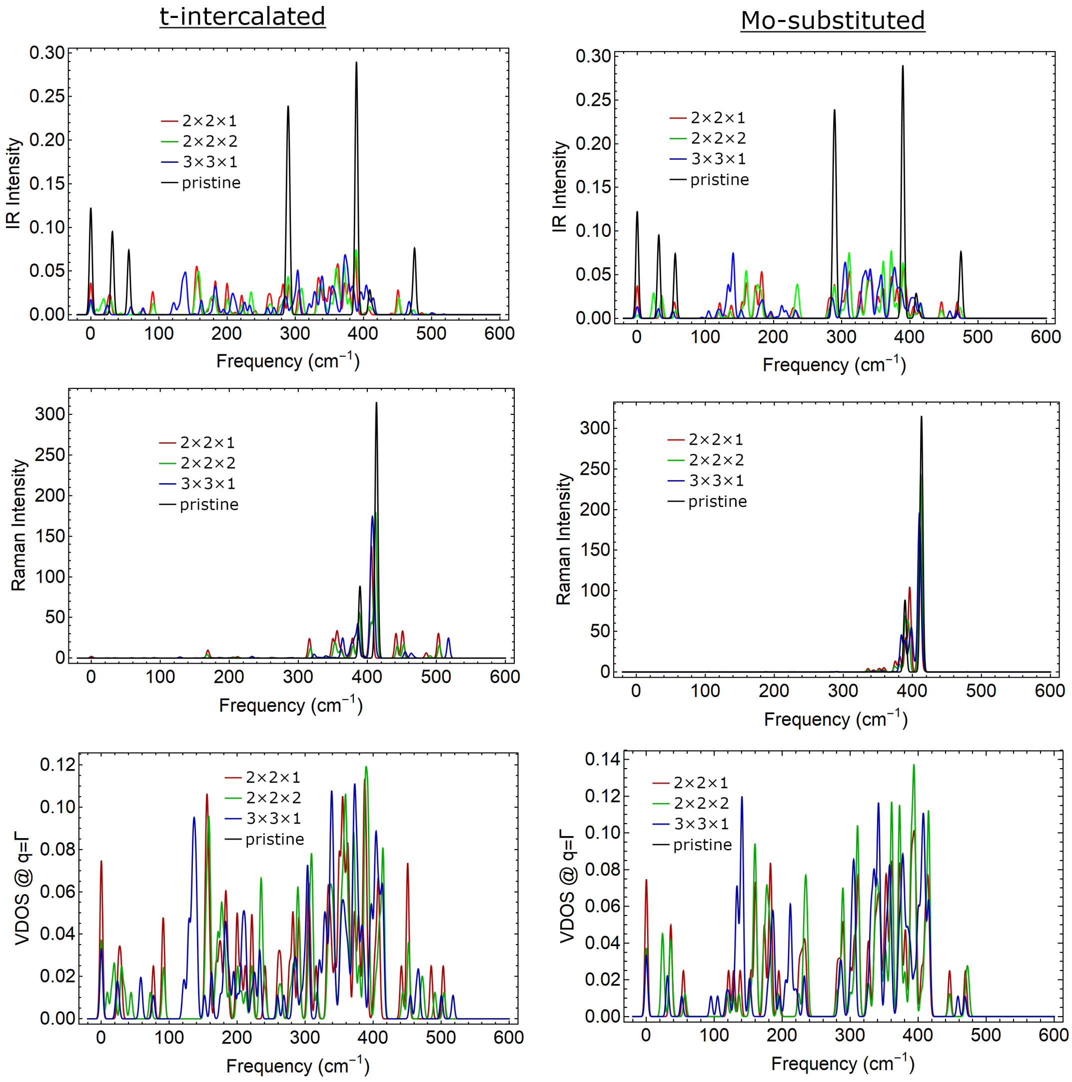

Figure 8.10: IR spectra, full Raman spectra, and VDOS at q=Γ of t-intercalated and Mo-substituted structures as computed by DFPT and Raman tensor substitution.

Table 8.4: Structural parameters (Å) for Re-doped MoS$_2$.

	Bond lengths	a, b, c (Å)	α, β, γ (°)
Pristine	-	3.191, 3.191, 12.415	90.0, 90.0, 120.0
$2 \times 2 \times 1$			
Mo-subst.	Re-S: 2.375×2, 2.414×2, 2.415×2	6.367, 6.382, 12.351	90.00, 90.00, 119.91
t-intercal.	Re-S: 2.224, 2.226×2, 2.245	6.399, 6.399, 12.758	89.95, 90.05, 120.05
S vac.+Ni	Re-S: 2.320×3	6.394, 6.394, 11.659	90.02, 89.99, 120.05
o-intercal.	Re-S: 2.393×2, 2.395×4	6.372, 6.372, 12.671	90.04, 89.96, 120.08
Split Mo/Re	Re-S: 2.222×3, Re-Mo: 2.249	6.541, 6.541, 12.466	90.00, 90.00, 120.00
$2 \times 2 \times 2$			
Mo-subst.	Re-S: 2.374×2, 2.415×2, 2.416×2	6.374, 6.382, 24.765	90.00, 90.00, 119.96
t-intercal.	Re-S: 2.224, 2.226×2, 2.243	6.390, 6.390, 25.176	89.99, 90.01, 120.02
S vac.+Ni	Re-S: 2.375, 2.405×2, 2.436×2	6.359, 6.359, 24.364	87.88, 92.12, 119.71
o-intercal.	Re-S: 2.391×4, 2.400×2	6.378, 6.378, 25.079	90.07, 89.93, 120.02
Split Mo/Re	Re-S: 2.211×3, Re-Mo: 2.252	6.462, 6.462, 24.903	90.00, 90.00, 119.99
$3 \times 3 \times 1$			
Mo-subst.	Re-S: 2.386×2, 2.394×4	9.584, 9.584, 12.367	90.00, 90.00, 120.04
t-intercal.*	Re-S: 2.380×6	9.599, 9.598, 12.394	82.60, 97.40, 119.99
S-subst.	Re-Mo: 2.706, 2.708×2	9.564, 9.564, 12.231	90.00, 90.01, 120.00
o-intercal.	Re-S: 2.378, 2.379, 2.39×4	9.572, 9.580, 12.560	89.97, 89.82, 120.01
Split Mo/Re	Re-S: 2.242, 2.246×2, Re-Mo: 2.261	9.656, 9.656, 12.471	90.00, 90.00, 119.91
$4 \times 4 \times 1$			
Mo-subst.	Re-S: 2.389×4, 2.392×2	12.775, 12.775, 12.385	90.00, 90.00, 119.94
t-intercal.	Re-S: 2.217×3, 2.218	12.775, 12.775, 12.567	90.00, 90.00, 120.00
S-subst.	Re-Mo: 2.701×3	12.756, 12.756, 12.313	90.00, 90.00, 120.00
o-intercal.	Re-S: 2.383×4, 2.399×2	12.758, 12.758, 12.499	90.19, 89.81, 120.04
Split Mo/Re	Re-S: 2.245×3, Re-Mo: 2.260	12.831, 12.830, 12.444	90.00, 90.00, 120.01

Re bonds are shown with a multiplier signifying multiple bonds of equal lengths. *The anomalous $3 \times 3 \times 1$ t-intercalated structure relaxed to a 6-bonded structure.

Table 8.5: Formation energies (eV per MoS_2 unit)

	$2 \times 2 \times 1$	$2 \times 2 \times 2$	$3 \times 3 \times 1$	$4 \times 4 \times 1$
($\mu_{\text{Mo}} = \mu_{\text{S}} = 0$)				
Pristine	-2.62	-2.62	-2.62	-2.62
Mo-subst.	-2.27	-2.44	-2.46	-2.53
t-intercal.	-2.00	-2.30	-2.39	-2.45
S-subst. / S vac. + Ni	-1.79	-2.22	-2.25	-2.41
o-intercal.	-1.93	-2.27	-2.30	-2.44
Split Mo/Re	-1.91	-2.25	-2.32	-2.45
Mo-rich ($\mu_{\text{Mo}} = -2.616$ eV, $\mu_{\text{S}} = 0$)				
Pristine	0	0	0	0
Mo-subst.	0.015	7.66×10^{-3}	9.23×10^{-3}	4.80×10^{-3}
t-intercal.	0.620	0.311	0.228	0.168
S-subst. / S vac.+Ni	0.823	0.398	0.370	0.208
o-intercal.	0.684	0.342	0.316	0.179
Split Mo/Re	0.705	0.367	0.297	0.168
S-rich ($\mu_{\text{Mo}} = 0, \mu_{\text{S}} = -1.308$ eV)				
Pristine	0	0	0	0
Mo-subst	0.342	0.171	0.155	0.0865
t-intercal.	0.620	0.311	0.228	0.168
S-subst. / S vac. + Ni	0.660	0.316	0.297	0.167
o-intercal.	0.684	0.342	0.316	0.179
Split Mo/Re	0.705	0.367	0.297	0.168

Chapter 9

Re-Doped MoS_2: Mechanics of Strain and AFM Sliding

This chapter is based on work with identical motivations to the previous chapter. The section outlines our contribution to a work led by the Baykara group on explaining an interesting phenomenon with Re-doped MoS_2 sliding in a future publication [1].

9.1 Introduction

Typically, as the number of layer increases between 2D materials, the frictional force measured via atomic force microscopy (AFM) decreases [43]. Recent measurements revealed an opposite trend with Re-doped MoS_2, i.e. friction increases with increasing layer count [1]. In this work, we provided density functional theory simulations of Re-doped MoS_2 to complement those observations with computation.

The atomistic mechanism for the typical layer count *vs.* friction relationship is related to puckering—out-of-plane deformations caused by the AFM probe [99]. The puckered material provides an increased friction when compared to a flat sheet. More layers in principle mutes the strength of puckering, and this is related to the out-of-plane stiffness.

To provide insight on this topic, we subject Mo-substituted and t-intercalated

Re-doped MoS_2 to two conditions and compute macroscopic observables using density functional theory (DFT). First we compute the elastic components of the material by applying strain in the bulk phase and computing the stresses. Secondly, we model a Si AFM tip and compute the energies and forces at points along a sliding paths for variable-layer Re-doped MoS_2. This AFM model is not large enough to compute puckering effects, but it serves to discount significant electronic rearrangement leading to the increased frictional force.

We will find a significant difference in C_{33}, the out-of-plane elastic component between t-intercalated and Mo-substituted MoS_2 where t-intercalation is stiffer. With AFM simulations, we find that the friction is larger when doped, but more importantly the frictional forces do not change when increasing layers.

9.2 Methods

We used the plane-wave density functional theory code Quantum ESPRESSO v6.6 [50, 49]. Calculations were performed using the Perdew-Burke-Ernzerhof (PBE) generalized gradient approximation [139] with the Grimme-D2 (GD2) Van der Waals correction [53]. The pseudopotentials used were obtained from PseudoDojo [187]. PBE+GD2 was used with 60 Ry plane-wave cutoff, as in the previous chapter, because of its superior performance for elastic parameters [137]. We study Mo-substitution and t-intercalation, which we found to be the most reasonable doping sites for Re in bulk 2H-MoS_2 [57]. Spin-unpolarized calculations are used for vibrations and forces, because spin polarization caused spurious irregularities due to switching between different magnetic states. Spin-polarized calculations are used for elasticity as it does not pose a problem in this case (except for the anomalous $3 \times 3 \times 1$ t-intercalated structure [57]). Our calculations are performed in periodic boundary conditions. For pristine MoS_2, it is sufficient to use the primitive unit cell, but for doped structures, we use supercells to see the effect of doping concentration on properties.

The elastic parameters in Fig. 9.7 were computed by linear regression and the stress-strain relationship $\sigma_i = C_{ij}\epsilon_j$ (in Voigt notation, where i or j can represent any pair of Cartesian directions), where σ is the stress, C is the elasticity tensor, and ϵ is strain. We have similarly computed these values for Ni in a prior publication [58]. Our coordinate system is as in the previous chapters, where z is out-of-plane. We used $2 \times 2 \times 1$, $2 \times 2 \times 2$, $3 \times 3 \times 3$ and $4 \times 4 \times 1$ supercells, in order of decreasing Re concentration, with Monkhorst-Pack k-grids of $3 \times 3 \times 2$, $3 \times 3 \times 1$, $3 \times 3 \times 2$, and $2 \times 2 \times 2$ respectively. For pristine, only the primitive unit cell is used (yielding the horizontal lines in Fig. 9.7, as the cell size has no effect due to periodicity. Structures were relaxed for strains of -0.002 to 0.002 in steps of 0.001, in the 1- (x-uniaxial), 3- (z-uniaxial) and 5-directions (xz-shear). These strain directions are important to sliding and friction. Shear results in sliding between layers [146]. Out-of-plane uniaxial strain is important in determining the amplitude of puckering as argued in the main text [1], and the out-of-plane Poisson's ratio ν_{zx} connects in-plane and out-of-plane deformation that can occur due to the load from an AFM tip. The various elastic parameters including the in-plane Poisson's ratio ν_{xy} occur in the formula for bending stiffness (flexural rigidity) [184]:

$$D = \frac{E_x h^3}{12(1 - \nu_{xy}^2)}$$

where in hexagonal symmetry the in-plane Young's modulus is

$$E_x = \frac{(C_{11} - C_{12})(C_{11}C_{33} + C_{12}C_{33} - 2C_{31}^2)}{C_{11}C_{33} - C_{31}^2}$$

and

$$\nu_{xy} = \frac{C_{31}^2 - C_{12}C_{33}}{C_{31}^2 - C_{11}C_{33}}.$$

ν_{zx} was computed as $C_{31}/(C_{11} + C_{12})$. The difference between the value from experimental elastic parameters (0.125) [42] and our computed value (0.05) for ν_{zx} in pristine MoS_2 is due to the highly sensitive nature of out-of-plane van der Waals interactions in these systems, as seen in the large variability [136] in computed C_{31} values with different DFT approximations. We nonetheless expect that trends in $\nu_z x$ could be meaningful. The ν_{xy} value by contrast agrees with the value 0.28 calculated from experimental elastic parameters [42].

We model slabs of t-intercalated, Mo-substituted, or undoped layers beneath an AFM probe tip. The tip cluster shown in Fig. 9.1 is a geometry used previously in the literature to simulate an AFM tip. It is generated by cleaving 10 atoms perpendicular to the (111) corner of the Si unit cell then passivating all dangling bonds with H except for the tip Si atom [46]. The top Si layer of 6 atoms was frozen to crystalline positions, but other Si and H atoms were allowed to relax. This structure was placed 5 Å above the topmost Mo layer of Re-doped MoS_2 (about 3.5 Å above the S plane). We studied the variation in energy for different distances of the tip from the MoS_2 surface (Fig. 9.2) and chose a working distance for force calculations which was close enough to measure friction forces above numerical noise but far enough that the Si tip and MoS_2 are not bonding. We used the atomic coordinates of a 4×4 in-plane bulk supercell with variable numbers of layers, fixed to the bulk values without relaxation at the beginning or during sliding. We avoid relaxation for simplicity and as part of the constraints defining the potential energy surface we are exploring. This lateral size of the structure provides sufficient vacuum for the AFM probe to be sufficiently separated from its periodic images in plane. A vacuum of 12.4 Å between the top Si layer and the S layer was used, as shown in Fig. 9.1. We varied the number of layers from 1 to 5 and varied the dopant site within each of those structures.

The probe was placed atop a Mo atom two rows away from the substitution site, as far as possible laterally. This is the best option as we do not expect a single-atom tip to be perfectly aligned with the dopant in experiment. Placing the tip directly above the Re site leads to larger variations in the forces while sliding as shown in Fig. 9.3. The probe was displaced in the x-direction in steps of 1/40th the cell's width ($\Delta x = 0.319$ Å) until the probe had moved by exactly one lattice vector. At each step, we calculated the DFT total energy. By differentiating with respect to the displacement, we compute the force along the path, $F_x = -\frac{\partial E}{\partial x} \approx -\frac{\Delta E}{\Delta x}$, which corresponds to friction forces. It is worth noting that the AFM structure does not have xz-mirror symmetry although MoS_2 does (see Fig. 9.1), and thus the sliding forces in Fig. 9.3 do not have that symmetry. The Hellmann-Feynman forces are computed by `Quantum ESPRESSO`, but we found the forces did not obey periodicity,

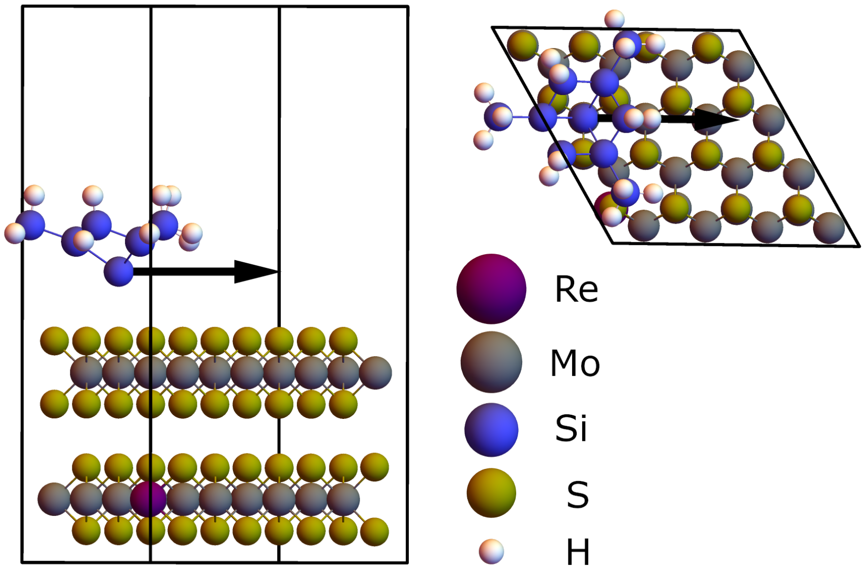

Figure 9.1: Example structure for AFM sliding: model H-passivated Si tip apex [46] above 2-layer Mo-substituted MoS_2.

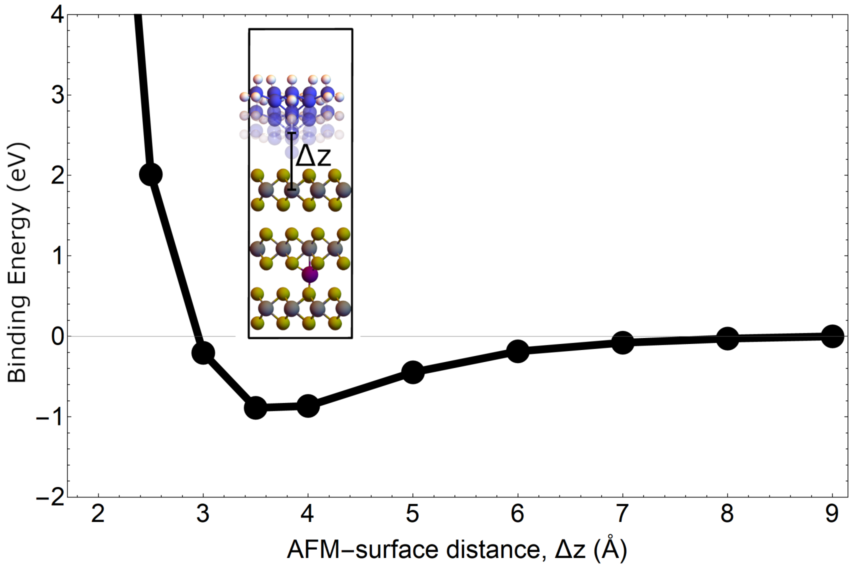

Figure 9.2: Energy dependence of the distance between the AFM probe and the surface of 3-layer t-intercalated MoS_2. The distance is measured between the Mo atom and the tip Si atom of the probe. Beyond 7 Å, the sliding dependence of the energy is lost to noise. Below 4 Å the interactions are strong and the tip bonds to the surface. Therefore 5 Å was used for our friction simulations.

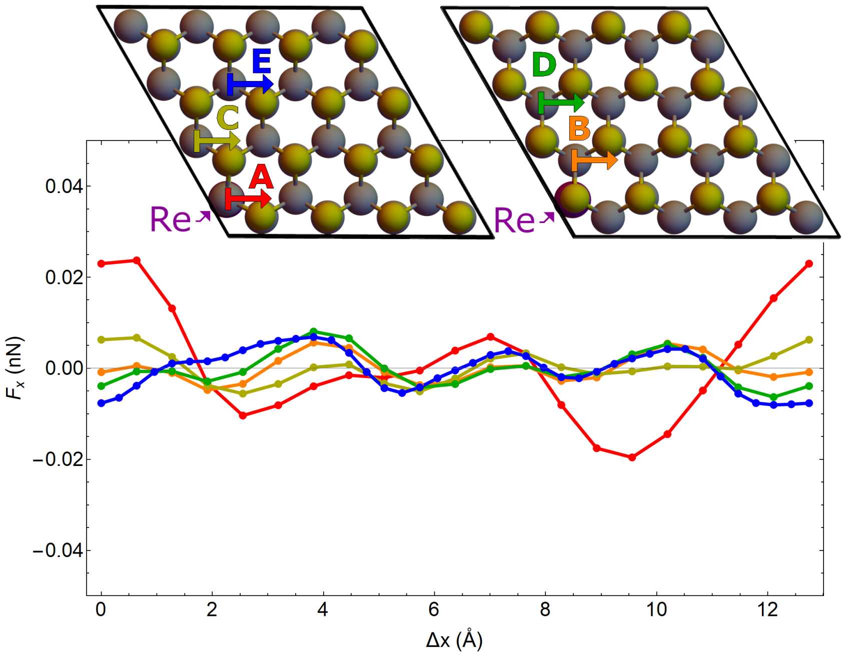

Figure 9.3: The sliding force calculated at different in-plane distances from Mo-substituted Re atoms. A, C, and E are computed for a 3-layer Mo-substituted structure while B and D are computed for a 2-layer Mo-substituted MoS_2, which allow different spatial relations between the top layer atoms and the dopant. In A, the tip passes directly above the Re atom, and thus the forces are larger. For choices besides A, the range of forces is similar. We use E, the furthest starting point in our supercell, as most representative of an AFM experiment for a sample with low doping concentration. The positive and negative x sliding directions are different due to the probe's asymmetric shape as seen in Fig. 9.1.

i.e. $\int_{cell} F_x dx \sim 5 - 50$ eV $\neq 0$ incorrectly. This imbalance can be improved by increasing the plane-wave cutoff, but we found that the effect was simply a constant shift (Fig. 9.4), and that the high-cutoff Hellman-Feynman forces agreed with lower-cutoff numerical derivatives forces (which correctly integrated to zero). Therefore we used the latter approach for lower computational expense.

The forces from each displacement are then collapsed into a distribution as shown in Fig. 9.6 based on how frequently the AFM experienced a given force throughout sliding. We use distributions rather than raw sliding forces since our single-atom tip may be more fine than an experimental tip, and real measurements would correspond to some convolution over our sliding forces. In theory, we would have to compute an N-layer (NL) system with the dopant in different layers,

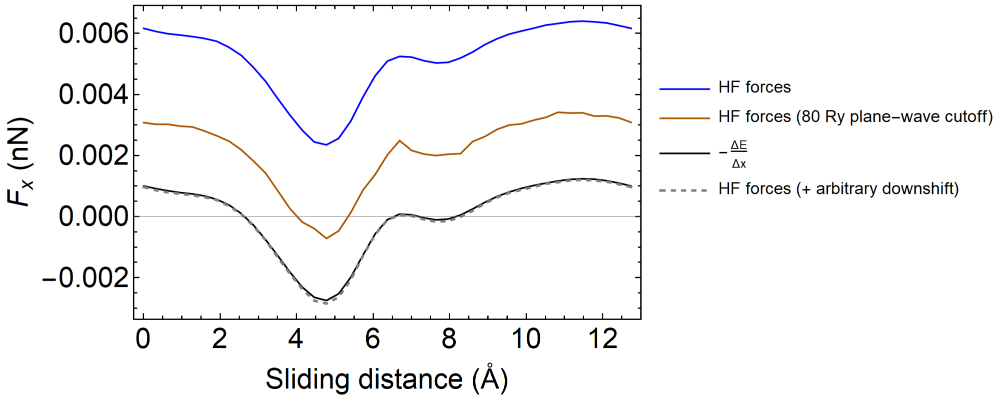

Figure 9.4: Computed sliding forces using different calculation modes. In blue, the Hellmann-Feynman x-forces on the AFM tip are computed for a 2-layer Mo-substituted structure with a 7 Å Si tip-to-Mo distance was computed using parameters mentioned in the main text. In brown, we have increased the plane-wave cutoff from 60 Ry to 80 Ry and reduced the SCF threshold to $10^{-6}Ry$ (this saves computational time but introduces noise). In black, we used the original 60 Ry computation's energies to compute the forces by finite differentiation of the energies. Note that unlike the blue and brown curves, the black curve correctly obeys the periodicity such that the forces sum to 0 across the sliding. The dashed curve is identical to the blue curve with an arbitrary 0.0052 nN downshift. In summation, this shows that increasing the plane-wave cutoff could yield Hellmann-Feynman forces that respect the periodicity, but it is unnecessary since the same effect can be achieved by using finite differentiation of the energies instead.

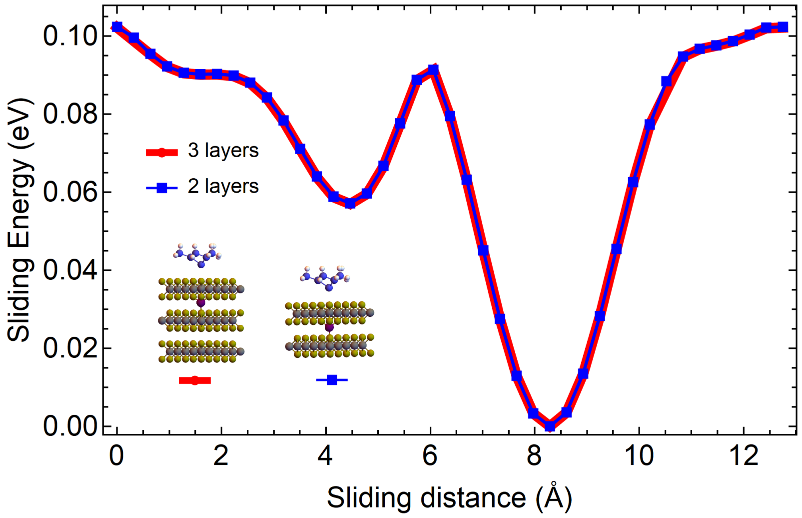

Figure 9.5: Energy change throughout sliding of the AFM system with a 3-layer and 2-layer t-intercalated Re-doped MoS_2 where the Re is in the same site in both systems. The additional layer in the 3-layer system leads to negligible changes to the sliding energies and thus forces.

rather than just using fewer layers, but we found that in practice adding undoped layers at the bottom of the slab, opposite the AFM tip, does not alter the energies (Fig. 9.5). Therefore we use slabs with just enough layers to contain the dopant, to minimize computational effort. The distribution is computed as the average of the smaller-layered distributions with each dopant position to generate Fig. 9.8. If n_i is the distribution of the forces while sliding an i-layer system, then the cumulative distribution is $n_{\text{cumul},i} = \frac{1}{N}\sum_{j\leq i} n_j$. We are assuming the dopant may be in any layer with equal probability, in the absence of clear evidence of the true distribution. There may be preferential locations however: placing the atom in different layers does lead to some changes in the energy, as we estimate by comparing energies for unrelaxed doped systems (i.e. the structure is that of pristine, with substitution or intercalation). In a 3-layer system, Mo substitution in the middle layer *vs.* surface is favored by 0.31 eV, while in a 4-layer system t-intercalation favors being bonded to a surface layer *vs.* the two middle layers by about 0.15 eV.

The small energy differences throughout sliding mean we need well-converged computational parameters to resolve them properly. The distance between the

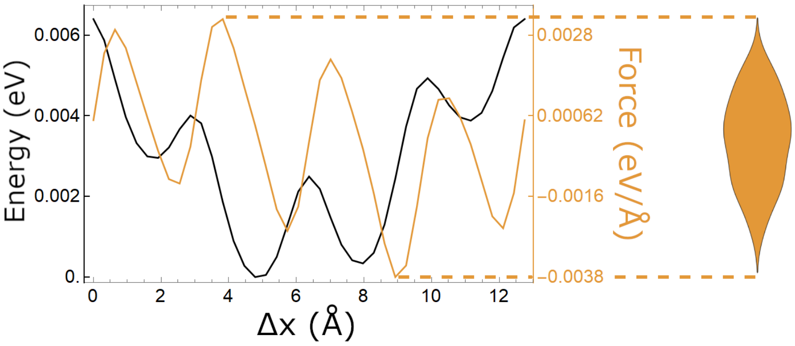

Figure 9.6: An example path to create a distribution of the t-intercalated 5L structure, where Re is between the bottom two layers. The energy curve is numerically differentiated to find forces, then those forces are compressed to a distribution. Assuming equal probability for the dopant to be between any of the layers in a real sample, we average the 5L distribution with the 4L, 3L, and 2L distributions, where in each case the Re is between the bottom two layers.

top of the probe and the bottom of the periodic image of the lowest sulfur atom was set to be 12.4 Å. Increasing this vacuum by 5 Å led to changes in energy differences below 10^{-4} eV—meaning our vacuum distance is sufficient to remove spurious interactions between periodic images in the z direction. Using a 3×3×1 k-grid yields nearly identical energy curves (like Fig. 9.6) to 2×2×1,

9.3 Results and Discussion

9.3.1 Elasticity

Intercalation alters the elastic parameters from the pristine more than Mo-substitution. This is due to the formation of interlayer bonds, which cause an increase in the out-of-plane C_{33} parameter in Fig. 9.7, similar to Ni-doping [58]. A drop in C_{55} for t-intercalation may enhance sliding, since reaching plastic deformation by shearing can be easier. Each elastic parameter shows linear trends, though with an outlier for C_{55} ($3 \times 3 \times 1$ t-intercalated, which has a different stacking [57]). The changes are quite small for C_{11} and E_x. ν_{xy} has irregular trends and relatively small changes. The largest systematic changes are in C_{33}, which we relate to a weakening of the puckering effect and the altered layer-dependence of friction. While other elastic parameters vary somewhat with concentration, and can be involved in the stress patterns of puckering, the lesser effect and/or irregular behavior indicates that they have only a minor contribution to the layer dependence of puckering.

9.3.2 AFM Simulation

The force distributions are shown in Figs. 9.8 and 9.9—they move to smaller forces as we go from 2 to 3 layers in doped systems. Beyond 2 layers from the AFM, however, layer-dependence is small. The range of the forces for doped MoS_2 is much larger than pristine MoS_2. The undoped forces decrease between 1 and 2 layers, but then change negligibly between 2 and 3 layers. The weak layer-dependence and reduction in force with number of layers, assuming rigid flat sheets, cannot explain the increase in friction seen in AFM experiments [1], pointing to the role of changes in puckering.

The force distributions for doped systems with many layers would be expected to converge to the pristine distribution as the Re atom's influence wanes with increasing distance from the AFM tip. However, we find convergence to a different distribution than pristine (Fig. 9.8). We considered whether this might be due to localization at the surface of electronic charge donated from Re to MoS_2, which would not vary with number of layers. We tested this with calculations of undoped slabs with extra charge from $-0.25\ e$ to $-1.0\ e$—in all cases, the extra charge is localized on the AFM. This is presumably not a physical effect and relates to the crude model of the AFM tip as well as perhaps difficulties with charge transfer in PBE and LDA [228], but it means that it is not meaningful to calculate AFM forces for such a charged system. A slab without the AFM tip does not show localization of charge to the surface. The difference in forces between pristine and slabs with Re far from the tip instead seems to be due to long-range interaction of the tip with polarization caused by the distortion of the MoS_2 geometry around Re. We calculate out-of-plane polarization by integrating the charge density, and find the following values for 3-layer systems: with Mo substitution in the outer surface, $-0.29\ e/\text{Å}$; with intercalation, $-0.29\ e/\text{Å}$; pristine but with the geometry

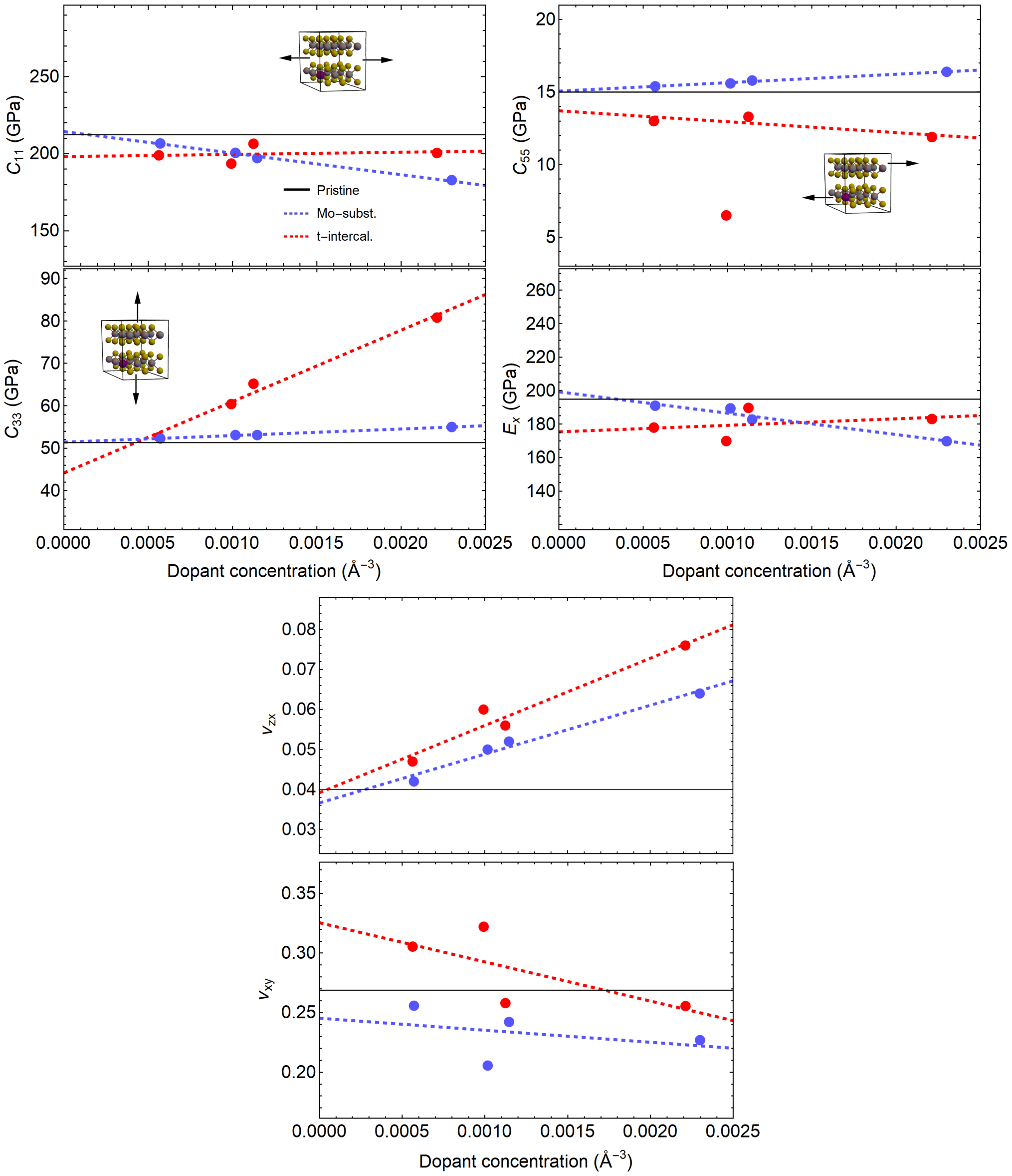

Figure 9.7: Elastic parameters C_{11}, C_{33}, C_{55}, E_x, ν_{zx}, and ν_{xy} of Mo-substituted and t-intercalated Re-doped MoS_2 with fit lines excluding outliers, compared to pristine values. The C_{33} parameter shows the largest and most consistent relative difference between t-intercalated and Mo-substituted structures, owing to the change in out-of-plane bonding.

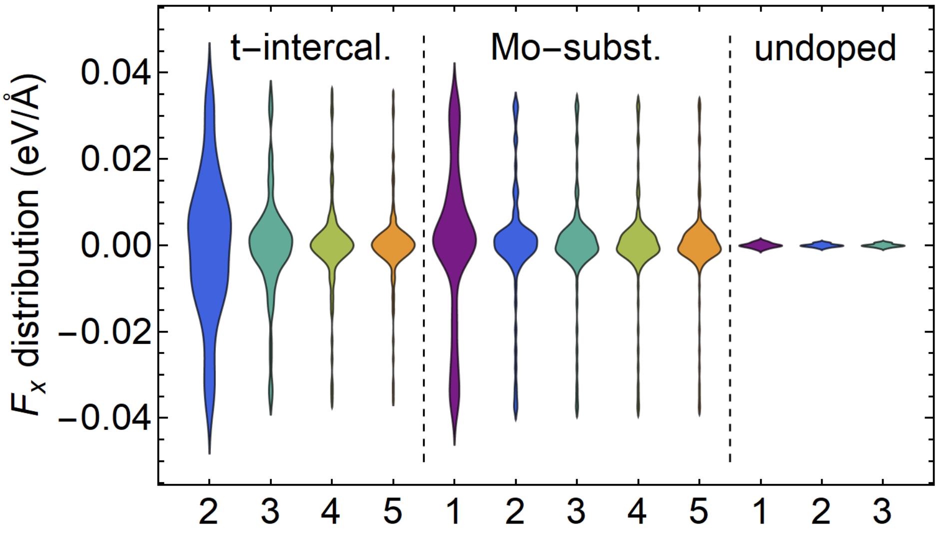

Figure 9.8: Cumulative force distributions throughout sliding calculations for different structural configurations. Beyond two layers, the force distributions are similar.

of Mo substitution, $-0.28\ e/\text{Å}$; non-distorted pristine, $-0.05\ e/\text{Å}$ (nonzero only due to some numerical symmetry-breaking). Interestingly, the values are consistent regardless of the site for Re.

9.4 Conclusion and Outlook

We modeled AFM friction on pristine, Mo-substituted and t-intercalated MoS_2, constrained the layers to remain flat, and found that Re doping increases friction, with an effect that decreases with layers but has little layer-dependence beyond two layers. These findings point to the importance of puckering changes in the experimentally observed [1] unusual increase in friction with number of layers. This effect can be connected to the strong increase in the out-of-plane stiffness C_{33} with doping concentration for t-intercalation. Other elastic parameters show lesser or irregular trends.

A few results of methodological interest were found. Experimental ambiguity of the Re's location is addressed by comparing cumulative forces, as well as layer-dependent forces. A remarkable compatibility between the sliding energies between 2- and 3-layer MoS_2 with Re in an identical location as in Fig. 9.5 yields similar

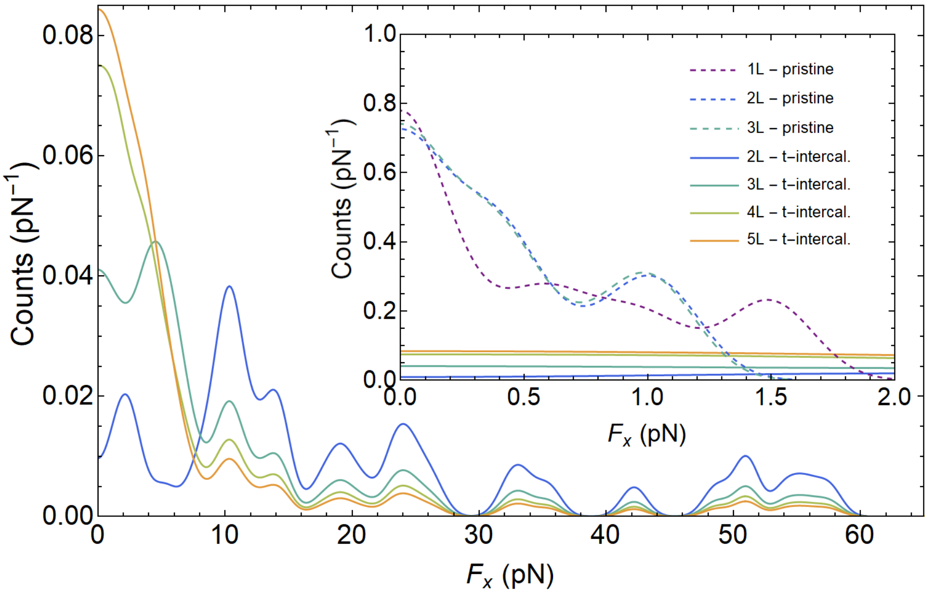

Figure 9.9: Friction force distributions for t-intercalated Re-doped MoS_2 with different numbers of layers, compared with pristine MoS_2. Each distribution describes the friction force experienced during sliding of the model AFM tip apex over an N-layer system, averaging over possible locations of the Re dopant among the layers. The saturation point is around 4 layers. A smoothing parameter of 1 pN is used for plotting with `Mathematica`'s `SmoothHistogram` function [206]. Inset: Expanded view to compare pristine MoS_2, having much lower forces, with doped MoS_2; two and three layers are almost identical. Smoothing parameter is 0.175 pN.

result to those seen in Ch. 6—only the sliding interface is relevant when computing the sliding potential.

Chapter 10

Conclusion: Summaries and Outlook

Throughout this work, we have developed methodologies for analyzing amorphous materials and two-dimensional materials. We have found a range of physical results in a-Si and doped $\mathrm{MoS_2}$ that could be used to further study and concentrate computational efforts on the materials.

With Si, we created a simple adjustment to the WWW algorithm to be able to generate structures with voids by initializing the structure with strain. The bonding topology at the void's surface is unique in that the existence of voids without dangling bonds (or capped dangling bonds) has not been previously reported. The relative size of the voids can be somewhat controlled by using larger strains, but this does not bias the voids' morphology since strain is applied everywhere equally. These voids appear as an emergent quality of the initial strain. A systematic method to study the range of void influence is presented in Ch. 3. Besides void topology, a-Si:H behaves qualitatively similar to a-Si in response to strain initialization, except that the DOF allotted by H lead to smoother parameter responses.

Though the exact atomic coordinates are adjusted by DFT, the simple Keating potential and WWW do not lose their bonding network when relaxed by DFT. Statistically averaged formulations of the Keating potential yield the result that $\Delta\theta$ is the dominant energetic term. With our work, this is confirmed by DFT.

The configurational energy gap posed by Drabold [37] can be reformulated as a gap in the order parameter, $\Delta\theta$. This removes a layer of abstraction of the energy gap which can be thought of as a geometric question—what is the minimum amount of bond distortion required for a structure to be considered amorphous? A continuation of the foundational work in Ch. 4 should yield more quantitative relationships between the DFT energy and $\Delta\theta$.

With 2D materials, we have outlined a specific methodology to study sliding of defected materials in Ch. 6. By utilizing successively less constraining restrictions on atomic relaxations, we learn more than what one can usually learn in the grid-based sliding potential search. Our relaxation scheme is able to detect slip planes and can access low-barrier sliding paths with no previous knowledge of their existence. We find that the sliding potential in MoS_2, even with a highly invasive intercalant, can be described as pairwise interactions of the MoS_2 interfacing surfaces. In effect, this gives credence to computing arbitrarily sized systems by only considering interactions of their interfaces.

This also has an added benefit of resolving an apparent paradox with tetrahedrally intercalated Ni-doped MoS_2. This structure, we computed, is the most stable despite it being often ignored in literature in favor of Mo-substitution. We found t-intercalation leads to strong covalent bonding between neighbors, thereby closing the van der Waals gap. This means t-intercalation binds layers together, leading to larger dissociation energies and possibly increased resistance to wear [81]. T-intercalation also has a high sliding potential (and thus friction) when sliding across the intercalant, suggesting a drop in lubrication. This paradox is solved if we consider slip planes—the material prefers to slip away from the intercalant and can do so at no penalty to the sliding barrier.

Atomic force microscopy experiments of Re-doped MoS_2 showed a peculiar relationship—as the number of layers increased, the frictional force also increased. This is counter to other studied 2D materials [1]. Computations from our work combined with experimental work from the Baykara group points towards intercalated Re potentially altering this relationship. In computing the vibrational spectroscopy, we found a method to compute the Raman spectra of an apparent metallic doped material. This Raman tensor replacement method is a bridge that overcomes unphysical restrictions as a consequence of the static approximation. Tensor replacement can also be used as a tool to classify phonon modes. Replacing the tensor, but keeping the symmetry-broken phonon modes, can locate regions of the Raman spectrum related to symmetry breaking, and not modes localized to the dopant.

Numerous future paths exist that can provide further insight as to the materials' properties. With a-Si, the void-rich structures can be used to study the difference in roles of dangling bonds or void presence in the SWE [163] by computing excited states. It has thus far been shown that dangling bonds are effective hole traps [76, 122], but it is unknown if voids can enhance the trap. Similarly, excited state computations of c-Si/a-Si interfaces could reveal hidden electronic structure, particularly any traps, at the interface of these highly compatible materials. Excited state forces could be computed on the void-rich hydrogenated structures we generated, and we can search for light-induced degradation directly.

The often cited Beeman-Tsu-Thorpe [8] relationship connects widths of peaks in Raman spectra to $\Delta\theta$ and is used in many experimental works. Experimentalists are unable to measure $\Delta\theta$ directly, but computationalists can. Using the variable $\Delta\theta$ structures we generated, we could test this relationship directly at the DFT level by comparing $\Delta\theta$ to computed Raman spectra, though this requires considerable computational effort. Findings in Ch. 8 that the Raman spectra of a difficult system can be computed with a proxy system immediately remind me of amorphous Si. Could this atomic Raman Tensor replacement method work for amorphous Si by replacing its tensor with the tensor of c-Si? If so, it could mean a DFT-level Raman intensity could be applied to classical phonons—the converse of what we accomplished in that chapter.

Paths currently being pursued in MoS_2 are related to sliding in the Ni-doped system. Karen Mohammadtabar [116] at the Martini group is using data from this work to simulate large scale sliding. Studying these events can shed light on the full atomistic mechanisms for sliding—especially those difficult in DFT such as edge effects. Elsa Vazquez in our own Strubbe Ab Initio Laboratory is pursuing two-dimensional grids analogous to our 1D-sliding potentials in Ch. 6. The simplistic registry index model has been successfully applied on pristine MoS_2 to compute the sliding full, 2D potential with only three computations [18]. This is, however, highly dependent on the system's symmetry which is broken when doped. We could use this method, paired with the methodologies in Ch. 6 to quantify the effects of the pristine contributions to the sliding potential as compared to the dopants' contribution.

With Re in Chapter 9, the size-limitations of DFT make capturing puckering effects difficult, as they may involve a large area. Combining DFT with findings in Ch. 6 could lead to accurate, large, and fast DFT-based computations of AFM tip, though exploratory studies would need to be pursued.

Bibliography

[1] O. Acikgoz, E. Guerrero, A. Yanilmaz, O. E. Dagdeviren, C. Çelebi, and M. Z. Strubbe, David A. Baykara. Intercalation leads to inverse layer dependence of friction on chemically doped MoS_2. *arXiv:2007.05805*, 2020.

[2] N. Al-Dulaimi, E. A. Lewis, N. Savjani, P. D. McNaughter, S. J. Haigh, M. A. Malik, D. J. Lewis, and P. O'Brien. The influence of precursor and rhenium incorporation into Re-doped MoS_2 ($Mo_{1-x}Re_xS_2$) thin films by aerosol-assisted chemical vapour deposition (AACVD). *J. Mater. Chem. C*, 5:9044–9052, 2017. doi: 10.1039/C7TC01903C.

[3] M. P. Andersson. Density functional theory with modified dispersion correction for metals applied to self-assembled monolayers of thiols on Au(111). *J. Theor. Chem.*, 2013:327839, 2013. doi: 10.1155/2013/327839.

[4] N. H. Attanayake, A. C. Thenuwara, A. Patra, Y. V. Aulin, T. M. Tran, H. Chakraborty, E. Borguet, M. L. Klein, J. P. Perdew, and D. R. Strongin. Effect of intercalated metals and the electrocatalytic activity of 1T-MoS_2 for the hydrogen evolution reaction. *ACS Energy Lett.*, 3:7–13, 2018. doi: 10.1021/acsenergylett.7b00865.

[5] G. T. Barkema and N. Mousseau. High-quality continuous random networks. *Phys. Rev. B*, 62:4985–4990, 2000. doi: 10.1103/PhysRevB.62.4985.

[6] S. Baroni, S. de Gironcoli, and A. Dal Corso. Phonons and related crystal properties from density-functional perturbation theory. *Rev. Mod. Phys.*, 73: 515–562, 2001. doi: 10.1103/RevModPhys.73.515.

[7] J. Baum, K. K. Gleason, A. Pines, A. N. Garroway, and J. A. Reimer. Multiple-quantum NMR study of clustering in hydrogenated amorphous silicon. *Phys. Rev. Lett.*, 56:1377–1380, 1986. doi: 10.1103/PhysRevLett.56.1377.

[8] D. Beeman, R. Tsu, and M. F. Thorpe. Structural information from the Raman spectrum of amorphous silicon. *Phys. Rev. B*, 32:874–878, 1985. doi: 10.1103/PhysRevB.32.874.

[9] R. Bellisent, A. Menelle, W. S. Howells, A. C. Wright, T. M. Brunier, R. N. Sinclair, and F. Jansen. The structure of amorphous Si:H using steady state and pulsed neutron sources. *Physica B: Condens. Matter*, 156-157:217–219, 1989. doi: 10.1016/0921-4526(89)90635-2.

[10] M. Bernardi, M. Palummo, and J. C. Grossman. Extraordinary sunlight absorption and one nanometer thick photovoltaics using two-dimensional monolayer materials. *Nano Lett.*, 13:3664–3670, 2013. doi: 10.1021/nl401544y.

[11] M. Bernardi, C. Ataca, M. Palummo, and J. C. Grossman. Optical and electronic properties of two-dimensional layered materials. *Nanophotonics*, 6 (2):479–493, 2017. doi: 10.1515/nanoph-2015-0030.

[12] W. Beyer, W. Hilgers, P. Prunici, and D. Lennartz. Voids in hydrogenated amorphous silicon materials. *J. Non. Cryst. Solids*, 358(17):2023–2026, 2012. doi: 10.1016/j.jnoncrysol.2011.09.030. Proceedings of the 24th International Conference on Amorphous and Nanocrystalline Semiconductors (ICANS 24) Nara, Japan August 21-26, 2011.

[13] P. Biswas and S. R. Elliott. Nanoscale structure of microvoids in *a*-Si:H: A first-principles study. *J. Condens. Matter Phys.*, 27:435201, 2015. doi: 10.1088/0953-8984/27/43/435201.

[14] P. Biswas, R. Atta-Fynn, S. Chakraborty, and D. A. Drabold. Real space information from fluctuation electron microscopy: Applications to amorphous

silicon. *J. Condens. Matter Phys.*, 19:455202, 2007. doi: 10.1088/0953-8984/19/45/455202.

[15] P. Biswas, R. Atta-Fynn, and S. R. Elliott. Metadynamical approach to the generation of amorphous structures: The case of *a*-Si:H. *Phys. Rev. B*, 93: 184202, 2016. doi: 10.1103/PhysRevB.93.184202.

[16] P. Biswas, D. Paudel, R. Atta-Fynn, D. A. Drabold, and S. R. Elliott. Morphology and number density of voids in hydrogenated amorphous silicon: An ab initio study. *Phys. Rev. Appl.*, 7:024013, 2017. doi: 10.1103/PhysRevApplied.7.024013.

[17] M. Blander and J. Katz. Bubble nucleation in liquids. *AIChE Journal*, 21: 833–848, 1979. doi: 10.1002/aic.690210502.

[18] A. Blumberg, U. Keshet, I. Zaltsman, and O. Hod. Interlayer registry to determine the sliding potential of layered metal dichalcogenides: The case of *2h*-mos$_2$. *J. Phys. Chem. Lett.*, 3:1936–1940, 2012. doi: doi.org/10.1021/jz300735v.

[19] F. D. Brandão, G. M. Ribeiro, P. H. Vaz, J. C. González, and K. Krambrock. Identification of rhenium donors and sulfur vacancy acceptors in layered mos$_2$ bulk samples. *J. Appl. Phys.*, 119(23):235701, 2016. doi: 10.1063/1.4954017.

[20] G. Brunin, F. Ricci, V.-A. Ha, G.-M. Rignanese, and G. Hautier. Transparent conducting materials discovery using high-throughput computing. *npj Comput. Mater.*, 5:63, 2019. doi: 10.1038/s41524-019-0200-5.

[21] K. A. Bush, A. F. Palmstrom, Z. J. Yu, M. Boccard, R. Cheacharoen, J. P. Mailoa, D. P. McMeekin, R. L. Z. Hoye, C. D. Bailie, T. Leijtens, I. M. Peters, M. C. Minichetti, N. Rolston, R. Prasanna, S. Sofia, D. Harwood, W. Ma, F. Moghadam, H. J. Snaith, T. Buonassisi, Z. C. Holman, S. F. Bent, and M. D. McGehee. 23.6%-efficient monolithic perovskite/silicon tandem solar cells with improved stability. *Nat. Energy*, 2:17009, 2017. doi: 10.1038/nenergy.2017.9.

[22] W. Cai, O. Hod, and M. Urbakh. Interlayer registry index of layered transition metal dichalcogenides. *J. Phys. Chem. Lett.*, 13:3353–3359, 2022. doi: doi.org/10.1021/acs.jpclett.1c04202.

[23] D. E. Carlson. Hydrogenated microvoids and light-induced degradation of amorphous-silicon solar cells. *Appl. Phys. A*, 41(305), 1986. doi: 10.1007/BF00616053.

[24] S. Chakraborty and D. A. Drabold. Static and dynamic properties of hydrogenated amorphous silicon with voids. *Phys. Rev. B*, 79:115214, Mar 2009. doi: 10.1103/PhysRevB.79.115214.

[25] P. Charbonneau, J. Kurchan, G. Parisi, P. Urbani, and F. Zamponi. Fractal free energy landscapes in structural glasses. *Nat. Commun.*, 5:3725, 2014. doi: 10.1038/ncomms4725.

[26] M. F. Chen and D. L. Douglass. Effect of some ternary additions on the sulfidation of Ni-Mo alloys. *Oxid. Met.*, 33:103–133, 1990. doi: 10.1007/BF00665672.

[27] R. Chen, A. Jusufi, A. Schilowitz, and A. Martini. Formation of MoS_2 from elemental Mo and S using reactive molecular dynamics simulations. *J. Vac. Sci. Technol. A*, 38(2):022201, 2020. doi: 10.1116/1.5128377.

[28] X. Chen, Z. Chen, and L. Jun. Critical electronic structures controlling phase transitions induced by lithium ion intercalation in molybdenum disulphide. *Chin. Sci. Bull.*, 58:1632–1641, 2013. doi: 10.1007/s11434-013-5834-y.

[29] Y. C. Cheng, Z. Y. Zhu, W. B. Mi, Z. B. Guo, and U. Schwingenschlögl. Prediction of two-dimensional diluted magnetic semiconductors: Doped monolayer MoS_2 systems. *Phys. Rev. B*, 87:100401(R), 2013. doi: 10.1103/PhysRevB.87.100401.

[30] Z. Cheng, G. Zhang, B. Zhang, F. Ma, and Z. Lu. Tuning the electronic structure of hexagonal boron nitride by carbon atom modification: A feasible

strategy to reduce sliding friction. *Mater. Res. Express*, 6:036306, 2019. doi: doi.org/10.1088/2053-1591/aaf705.

[31] M. Cohen and S. Louie. *Fundamentals of Condensed Matter Physics*. Cambridge University Press, 2016. ISBN 9780521513319.

[32] S. S. Coutinho, M. S. Tavares, C. A. Barboza, N. Frazão, E. Moreira, and D. L. Azevedo. 3R and 2H polytypes of MoS_2: DFT and DFPT calculations of structural, optoelectronic, vibrational and thermodynamic properties. *J. Phys. Chem. Solids*, 111:25–33, 2017. doi: 10.1016/j.jpcs.2017.07.010.

[33] M. Denk, E. Speiser, J. Plaickner, S. Chandola, S. Sanna, P. Zeppenfeld, and N. Esser. Surface resonant raman scattering from cu(110). *Phys. Rev. Lett.*, 128:216101, 2022. doi: 10.1103/PhysRevLett.128.216101.

[34] V. L. Deringer, N. Bernstein, A. P. Bartók, M. J. Cliffe, R. N. Kerber, L. E. Marbella, C. P. Grey, S. R. Elliott, and G. Csányi. Realistic atomistic structure of amorphous silicon from machine-learning-driven molecular dynamics. *J. Phys. Chem. Lett.*, 9(11):2879–2885, 2018. doi: 10.1021/acs.jpclett.8b00902.

[35] X.-Z. Ding, X. T. Zeng, X. Y. He, and Z. Chen. Tribological properties of Cr- and Ti-doped MoS_2 composite coatings under different humidity atmosphere. *Surf. Coat. Tech.*, 205(1):224–231, 2010. doi: 10.1016/j.surfcoat.2010.06.041.

[36] K. Dolui, I. Rungger, C. D. Pemmaraju, and S. Sanvito. Possible doping strategies for MoS_2 monolayers: An *ab initio* study. *Phys. Rev. B*, 88:075420, 2013. doi: 10.1103/PhysRevB.88.075420.

[37] D. A. Drabold. Silicon: the gulf between crystalline and amorphous. *pss (RRL)*, 5(10-11):359–360, 2011. doi: 10.1002/pssr.201105444.

[38] A. N. Enyashin and G. Seifert. Density-functional study of Li_xMoS_2 intercalates ($0 \leq x \leq 1$). *Comput. Theor. Chem.*, 999:13–20, 2012. doi: 10.1016/j.comptc.2012.08.005.

[39] A. N. Enyashin, L. Yadgarov, L. Houben, I. Popov, M. Weidenbach, R. Tenne, M. Bar-Sadan, and G. Seifert. New route for stabilization of 1T-WS_2 and MoS_2 phases. *J. Phys. Chem. C*, 115:24586–24591, 2011. doi: 10.1021/jp2076325.

[40] M. Fehr, A. Schnegg, B. Rech, O. Astakhov, F. Finger, R. Bittl, C. Teutloff, and K. Lips. Metastable defect formation at microvoids identified as a source of light-induced degradation in $a-\mathrm{Si}:\mathrm{H}$. *Phys. Rev. Lett.*, 112:066403, 2014. doi: 10.1103/PhysRevLett.112.066403.

[41] D. W. Feldman, J. H. Parker, and M. Ashkin. Raman scattering by optical modes of metals. *Phys. Rev. Lett.*, 21:607–608, 1968. doi: 10.1103/PhysRevLett.21.607.

[42] J. L. Feldman. Elastic constants of 2H-MoS_2 and 2H-$NbSe_2$ extracted from measured dispersion curves and linear compressibilities. *J. Phys. Chem. Solids*, 37(12):1141–1144, 1976. doi: 10.1016/0022-3697(76)90143-8.

[43] T. Filleter, J. L. McChesney, A. Bostwick, E. Rotenberg, K. V. Emtsev, T. Seyller, K. Horn, and R. Bennewitz. Friction and dissipation in epitaxial graphene films. *Phys. Rev. Lett.*, 102:086102, 2009. doi: 10.1103/PhysRevLett.102.086102.

[44] R. Fletcher. *Newton-Like Methods*, chapter 3, pages 44–79. John Wiley & Sons, Ltd, 2000. ISBN 9781118723203. doi: 10.1002/9781118723203.ch3.

[45] J. Fortner and J. S. Lannin. Radial distribution functions of amorphous silicon. *Phys. Rev. B*, 39:5527–5530, 1989. doi: 10.1103/PhysRevB.39.5527.

[46] A. S. Foster, A. L. Shluger, and R. M. Nieminen. Realistic model tips in simulation of nc-AFM. *Nanotechnology*, 15:S60–S64, 2004. doi: 10.1088/0957-4484/15/2/013.

[47] J. Gao, Y. D. Kim, L. Liang, J. C. Idrobo, P. Chow, J. Tan, B. Li, L. Li, B. G. Sumpter, T.-M. Lu, V. Meunier, J. Hone, and N. Koratkar. Transition-

metal substitution doping in synthetic atomically thin semiconductors. *Adv. Mater.*, 28:9735–9743, 2016. doi: 10.1002/adma.201601104.

[48] D. Ghoshal, R. Kumar, and N. Koratkar. Controlled Re doping in MoS_2 by chemical vapor deposition. *Inorg. Chem. Commun.*, 123:108329, 2021. doi: 10.1016/j.inoche.2020.108329.

[49] P. Giannozzi, S. Baroni, N. Bonini, M. Calandra, R. Car, C. Cavazzoni, D. Ceresoli, G. L. Chiarotti, M. Cococcioni, I. Dabo, and et al. `QUANTUM` espresso: a modular and open-source software project for quantum simulations of materials. *J. Phys.: Condens. Matter*, 21:395502, 2009. doi: 10.1088/0953-8984/21/39/395502.

[50] P. Giannozzi, O. Andreussi, T. Brumme, O. Bunau, M. Buongiorno Nardelli, M. Calandra, R. Car, C. Cavazzoni, D. Ceresoli, M. Cococcioni, and et al. Advanced capabilities for materials modelling with `QUANTUM ESPRESSO`. *J. Phys.: Condens. Matter*, 29:465901, 2017. doi: 10.1088/1361-648X/aa8f79.

[51] K. K. Gleason, M. A. Petrich, and J. A. Reimer. Hydrogen microstructure in amorphous hydrogenated silicon. *Phys. Rev. B*, 36:3259–3267, 1987. doi: 10.1103/PhysRevB.36.3259.

[52] R. Gómez-Balderas, J. M. Martínez-Magadán, R. Santamaria, and C. Amador. Promotional effect of Co or Ni impurity in the catalytic activity of MoS_2: An electronic structure study. *Int. J. Quantum Chem.*, 80:406–415, 2000. doi: 10.1002/1097-461X(2000)80:3⟨406::AID-QUA10⟩3.0.CO;2-B.

[53] S. Grimme. Semiempirical GGA-type density functional constructed with a long-range dispersion correction. *J. Comput. Chem.*, 27(15):1787–1799, 2006. doi: 10.1002/jcc.20495.

[54] S. Grimme, J. Antony, S. Ehrlich, and H. Krieg. A consistent and accurate *ab initio* parametrization of density functional dispersion correction (DFT-D) for the 94 elements H-Pu. *J. Chem. Phys.*, 132:154104, 2010. doi: 10.1063/1.3382344.

[55] E. Guerrero and D. A. Strubbe. Computational generation of voids in *a*-Si and *a*-Si:H by cavitation at low density. *Phys. Rev. Mater.*, 4:025601, 2020. doi: 10.1103/PhysRevMaterials.4.025601.

[56] E. Guerrero and D. A. Strubbe. Atomistic mechanisms of sliding in few-layer and bulk doped MoS_2. *in preparation*, 2022.

[57] E. Guerrero and D. A. Strubbe. Structure, friction, and Raman spectroscopy of rhenium-doped bulk MoS_2 from first principles. *in preparation*, 2022.

[58] E. Guerrero, R. Karkee, and D. A. Strubbe. Phase stability and Raman/IR signatures of Ni-doped MoS_2 from density functional theory studies. *J. Phys. Chem. C*, 125:13401–13412, 2021. doi: doi.org/10.1021/acs.jpcc.1c02974.

[59] J. Guillevic, M. O. Bars, and D. Grandjean. Etude structurale de combinaisons sulfurées et séleniées du molybdène: Iii. Structure cristalline de $NiMo_3S_4$. *J. Solid State Chem.*, 7:158–162, 1973. doi: 10.1016/0022-4596(73)90149-7.

[60] M. Hakala, R. Kronberg, and K. Laasonen. Hydrogen adsorption on doped MoS_2 nanostructures. *Sci. Rep.*, 7:15243, 2017. doi: 10.1038/s41598-017-15622-z.

[61] T. Hallam, S. Monaghan, F. Gity, L. Ansari, M. Schmidt, C. Downing, C. P. Cullen, V. Nicolosi, P. K. Hurley, and G. S. Duesberg. Rhenium-doped MoS_2 films. *Appl. Phys. Lett.*, 111:203101, 2017. doi: 10.1063/1.4995220.

[62] D. R. Hamann. Optimized norm-conserving Vanderbilt pseudopotentials. *Phys. Rev. B*, 88:085117, 2013. doi: 10.1103/PhysRevB.88.085117.

[63] A. Hashemi, A. V. Krasheninnikov, Puska, Martti, and H. Komsa. Efficient method for calculating Raman spectra of solids with impurities and alloys and its application to two-dimensional transition metal dichalcogenides. *Phys. Rev. Mater.*, 3:023806, 2019. doi: 10.1103/PhysRevMaterials.3.023806.

[64] M. A. Hopcroft, W. D. Nix, and T. W. Kenny. What is the Young's Modulus of silicon? *J. Microelectromech. Syst.*, 19(2):229–238, 2010. doi: 10.1109/JMEMS.2009.2039697.

[65] C. Hu, C. Yi, M. Bai, J. Lv, and D. Tang. Molecular dynamics study of the frictional properties of multilayer $\mathrm{MoS_2}$. *RSC Adv.*, 10:17418, 2020. doi: 10.1039/d0ra00995d.

[66] G. Hu, V. Fung, X. Sang, R. R. Unocic, and P. Ganesh. Predicting synthesizable multi-functional edge reconstructions in two-dimensional transition metal dichalcogenides. *Npj Comput. Mater.*, 6(1):1–9, 2020.

[67] R. Hu, S. Y. Krylov, and J. W. M. Frenken. On the origin of frictional energy dissipation. *Tribol. Lett.*, 68:8, 2020. doi: 10.1007/s11249-019-1247-7.

[68] M. W. Iqbal, K. Shahzad, R. Akbar, and G. Hussain. A review on Raman finger prints of doping and strain effect in TMDCs. *Microelectron. Eng.*, 219: 111152, 2020. doi: 10.1016/j.mee.2019.111152.

[69] T. Ishii and A. Masuda. Annual degradation rates of recent crystalline silicon photovoltaic modules. *Prog. Photovolt: Res. Appl.*, 25:953–967, 2017. doi: 10.1002/pip.2903.

[70] V. V. Ivanovskaya, A. Zobelli, A. Gloter, N. Brun, V. Serin, and C. Colliex. *Ab initio* study of bilateral doping within the $\mathrm{MoS_2}$-$\mathrm{NbS_2}$ system. *Phys. Rev. B*, 78:134104, 2008. doi: 10.1103/PhysRevB.78.134104.

[71] H. C. Jacks. *Identifying Structures Responsible for Two-Level Systems in Amorphous Silicon.* PhD thesis, University of California, Berkeley, 2018.

[72] A. Jain, G. Hautier, S. P. Ong, C. J. Moore, C. C. Fischer, K. A. Persson, and G. Ceder. Formation enthalpies by mixing GGA and GGA + U calculations. *Phys. Rev. B*, 84:045115, 2011. doi: 10.1103/PhysRevB.84.045115.

[73] A. Jain, S. P. Ong, G. Hautier, W. Chen, W. D. Richards, S. Dacek, S. Cholia, D. Gunter, D. Skinner, G. Ceder, and et al. Commentary: The Mate-

rials Project: A materials genome approach to accelerating materials innovation. *APL Mater.*, 1:011002, 2013. doi: 10.1063/1.4812323. URL `https://materialsproject.org/`.

[74] X. Jiang, B. Goranchev, K. Schmidt, P. Grünberg, and K. Reichelt. Mechanical properties of a-Si:H films studied by Brillouin scattering and nanoindenter. *J. Appl. Phys.*, 67(11):6772–6778, 1990. doi: 10.1063/1.345064.

[75] E. Johlin, N. Tabet, S. Castro-Galnares, A. Abdallah, M. I. Bertoni, T. Asafa, J. C. Grossman, S. Said, and T. Buonassisi. Structural origins of intrinsic stress in amorphous silicon thin films. *Phys. Rev. B*, 85:075202, 2012. doi: 10.1103/PhysRevB.85.075202.

[76] E. Johlin, L. K. Wagner, T. Buonassisi, and J. C. Grossman. Origins of structural hole traps in hydrogenated amorphous silicon. *Phys. Rev. Lett.*, 110:146805, Apr 2013. doi: 10.1103/PhysRevLett.110.146805.

[77] E. Johlin, C. B. Simmons, T. Buonassisi, and J. C. Grossman. Hole-mobility-limiting atomic structures in hydrogenated amorphous silicon. *Phys. Rev. B*, 90:104103, 2014. doi: 10.1103/PhysRevB.90.104103.

[78] D. C. Jordan, C. Deline, S. Johnston, S. R. Rummel, B. Sekulic, P. Hacke, S. R. Kurtz, K. O. Davis, E. J. Schneller, X. Sun, M. A. Alam, and R. A. Sinton. Silicon heterojunctio system field performance. *IEEE J. Photovolt.*, 8(1):177–182, 2018. doi: 10.1109/JPHOTOV.2017.2765680.

[79] C. Julien, T. Sekine, and M. Balkanski. Lattice dynamics of lithium intercalated MoS_2. *Solid State Ion.*, 48(3):225–229, 1991. doi: 10.1016/0167-2738(91)90036-B.

[80] R. Karkee and D. A. Strubbe. Panoply of doping-induced reconstructions and electronic phases in Ni-doped 1T-MoS_2. *arXiv*, page 2107.07541, 2022.

[81] R. Karkee, E. Guerrero, and D. A. Strubbe. Enhanced interlayer interactions in Ni-doped MoS_2, and structural and electronic signatures of doping

site. *Phys. Rev. Mater.*, 5:074006, 2021. doi: 10.1103/PhysRevMaterials.5.074006.

[82] P. N. Keating. Effect of invariance requirements on the elastic strain energy of crystals with application to the diamond structure. *Phys. Rev.*, 145:637–645, 1966. doi: 10.1103/PhysRev.145.637.

[83] E. Kim, Y. H. Lee, C. Chen, and T. Pang. Vacancies in amorphous silicon: A tight-binding molecular-dynamics simulation. *Phys. Rev. B*, 59:2713–2721, 1999. doi: 10.1103/PhysRevB.59.2713.

[84] J. Kim, J.-U. Lee, and H. Cheong. Polarized Raman spectroscopy for studying two-dimensional materials. *J. Phys. Condens. Matter*, 32:343001, 2020. doi: 10.1088/1361-648X/ab8848.

[85] S. V. King. Ring configurations in a random network model of vitreous silica. *Nature*, 213(5081):1112–1113, 1967. doi: 10.1038/2131112a0.

[86] M. D. Kluge, J. R. Ray, and A. Rahman. Amorphous-silicon formation by rapid quenching: A molecular-dynamics study. *Phys. Rev. B*, 36:4234–4237, 1987. doi: 10.1103/PhysRevB.36.4234.

[87] W. Kohn and L. J. Sham. Self-consistent equations including exchange and correlation effects. *Phys. Rev.*, 140:A1133–A1138, 1965. doi: 10.1103/PhysRev.140.A1133.

[88] A. Kokalj. XCrySDen—A new program for displaying crystalline structures and electron densities. *J. Mol. Graph. Model.*, 17:176–179, 1999. doi: 10.1016/S1093-3263(99)00028-5.

[89] H.-P. Komsa and A. V. Krasheninnikov. Native defects in bulk and monolayer MoS_2 from first principles. *Phys. Rev. B*, 91:125304, 2015. doi: 10.1103/PhysRevB.91.125304.

[90] N. Kondekar, M. G. Boebinger, M. Tian, M. H. Kirmani, and M. T. McDowell. The effect of nickel on MoS_2 growth revealed with *in situ*

transmission electron microscopy. *ACS Nano*, 13:7117–7126, 2019. doi: 10.1021/acsnano.9b02528.

[91] Z. Kou, A. Hashemi, M. J. Puska, A. V. Krasheninnikov, and H.-P. Komsa. Simulating Raman spectra by combining first-principles and empirical potential approaches with application to defective MoS_2. *Comput. Mater.*, 6: 59, 2020. doi: 10.1038/s41524-020-0320-y.

[92] O. Krause, F. Müller, S. Birkmann, A. Böhm, M. Ebert, U. Grözinger, T. Henning, R. Hofferbert, A. Huber, D. Lemke, R. R.-R., S. Scheithauer, T. Gross, T. Fischer, G. Luichtel, H. Merkle, M. Übele, H.-U. Wieland, J. Amiaux, R. Jager, A. Glauser, Parr-Burmanm P., and J. Sykes. High-precision cryogenic wheel mechanisms of the JWST/MIRI instrument: Performance of the flight models. In *Proc. SPIE 7739, Modern Technologies in Space- and Ground-based Telescopes and Instrumentation*, page 773918, 2010. doi: 10.1117/12.856887.

[93] R. Kuschnereit, H. Fath, A. Kolomenskii, M. Szabadi, and P. Hess. Mechanical and elastic properties of amorphous hydrogenated silicon films studied by broadband surface acoustic wave spectroscopy. *Appl. Phys. A*, 61:269–276, 1995. doi: 10.1007/BF01538192.

[94] A. Kutana, E. S. Penev, and B. I. Yakobson. Engineering electronic properties of layered transition-metal dichalcogenide compounds through alloying. *Nanoscale*, 6:5820, 2014. doi: 10.1039/c4nr00177j.

[95] D. W. Latzke, W. Zhang, A. Suslu, T.-R. Chang, H. Lin, H.-T. Jeng, S. Tongay, J. Wu, A. Bansil, and A. Lanzara. Electronic structure, spin-orbit coupling, and interlayer interaction in bulk MoS_2 and WS_2. *Phys. Rev. B*, 91: 235202, 2015. doi: 10.1103/PhysRevB.91.235202.

[96] J. V. Lauritsen, J. Kibsgaard, G. H. Olesen, P. G. Moses, B. Hinnemann, S. Helveg, J. K. Nørskov, B. S. Clausen, H. Topsøe, E. Lægsgaard, and et al. Location and coordination of promoter atoms in Co- and Ni-promoted

MoS_2-based hydrotreating catalysis. *J. Catal.*, 249:220–233, 2007. doi: 10.1016/j.jcat.2007.04.013.

[97] M. Lazzeri and F. Mauri. First-principles calculation of vibrational Raman spectra in large systems: Signature of small rings in crystalline SiO_2. *Phys. Rev. Lett.*, 90:036401, 2003. doi: 10.1103/PhysRevLett.90.036401.

[98] S. Le Roux and P. Jund. Ring statistics analysis of topological networks: New approach and application to amorphous GeS_2 and SiO_2 systems. *Computational Materials Science*, 49(1):70–83, 2010. doi: 10.1016/j.commatsci.2010.04.023.

[99] C. Lee, Q. Li, W. Kalb, X.-Z. Liu, H. Berger, R. W. Carpick, and J. Hone. Frictional characteristics of atomically thin sheets. *Science*, 328:76–80, 2010. doi: 10.1126/science.1184167.

[100] J. Lee, Z. Wang, K. He, R. Yang, J. Shan, and P. X.-L. Feng. Electrically tunable single- and few-layer MoS_2 nanoelectromechanical systems with broad dynamic range. *Sci. Adv.*, 4:eaao6653, 2018. doi: 10.1126/sciadv.aao6653.

[101] G. Levita, A. Cavaleiro, E. Molinari, T. Polcar, and M. C. Righi. Sliding properties of MoS_2 layers: Load and interlayer orientation effects. *J. Phys. Chem. C*, 118:13809–13816, 2014. doi: doi.org/10.1021/jp4098099.

[102] P. Li, K. Yuan, D.-Y. Lin, X. Xu, Y. Wang, Y. Wan, H. Yu, K. Zhang, Y. Ye, and L. Dai. A mixed-dimensional light-emitting diode based on a p-MoS_2 nanosheet and an n-CdSe nanowire. *Nanoscale*, 46:18175–18179, 2017. doi: 10.1039/c7nr05706g.

[103] S. Li, J. Hong, B. Gao, Y. Lin, H. E. Lim, X. Lu, J. Wu, S. Liu, Y. Tateyama, Y. Sakuma, K. Tsukagoshi, K. Suenaga, and T. Taniguchi. Tunable doping of rhenium and vanadium into transition metal dichalcogenides for two-dimensional electronics. *Adv. Sci.*, 8:2004438, 2021. doi: 10.1002/advs.202004438.

[104] M. Lia, Z. Wei, L. Du, Q. Wang, J. Tang, H. Yu, F. Wu, Z. Jiaojiao, X. Xu, B. Han, K. Liu, P. Gai, T. Polcar, Z. Sun, D. Shi, R. Yang, and G. Zhang. Precise control of the interlayer twist angle in large scale $\mathrm{MoS_2}$, homostructures. *Nat. Commun.*, 11:2153, 2020. doi: 10.1038/s41467-020-16056-4.

[105] T. Liang, W. G. Sawyer, S. S. Perry, S. B. Sinnott, and S. R. Phillpot. First-principles determination of static potential energy surfaces for atomic friction in $\mathrm{MoS_2}$ and $\mathrm{MoO_3}$. *Phys. Rev. B*, 77:104105, 2008. doi: 10.1103/PhysRevB.77.104105.

[106] M.-L. Lin, Y. Zhou, J.-B. Wu, X. Cong, X.-L. Liu, J. Zhang, H. Li, W. Yao, and P.-H. Tan. Cross-dimensional electron-phonon coupling in van der Waals heterostructures. *Nat. Commun.*, 10:2419, 2019. doi: 10.1038/s41467-019-10400-z.

[107] Y. Lin, D. . Dumcenco, H. Komza, Y. Niimi, A. V. Krasheninnikov, Y. Huang, and K. Suenaga. Properties of individual dopant atoms in single-layer $\mathrm{MoS_2}$: Atomic structure, migration, and enhanced reactivity. *Adv. Mater.*, 26:2857–2861, 2014. doi: 10.1002/adma.201304985.

[108] T. Livneh and J. E. Spanier. A comprehensive multiphonon spectral analysis in $\mathrm{MoS_2}$. *2D Mater.*, 2:035003, 2015. doi: 10.1088/2053-1583/2/3/035003.

[109] A. H. Mahan, D. L. Williamson, B. P. Nelson, and R. S. Crandall. Small-angle x-ray scattering studies of microvoids in a-SiC:H and a-Si:H. *Solar Cells*, 27(1):465 – 476, 1989. doi: 10.1016/0379-6787(89)90056-2.

[110] A. H. Mahan, M. S. Dabney, D. Molina Piper, and W. Nemeth. The effect of film tensile stress on crystallite nucleation and growth in thermally annealed a-Si:H. *J. Appl. Phys.*, 115(8):083502, 2014. doi: 10.1063/1.4865943.

[111] J. Mao, Y. Wang, Z. Zheng, and D. Deng. The rise of two-dimensional $\mathrm{MoS_2}$ for catalysis. *Front. Phys.*, 13:138118, 2018. doi: 10.1007/s11467-018-0812-0.

[112] N. Marom, J. Bernstein, J. Garel, A. Tkatchenko, E. Joselevich, L. Kronik, and O. Hod. Stacking and registry effects in layered materials: The case of

hexagonal boron nitride. *Phys. Rev. Lett.*, 105:046801, 2010. doi: 10.1103/PhysRevLett.105.046801.

[113] J.-M. Martin. Superlubricity of molybdenum disulfide. In A. Erdemir and J.-M. Martin, editors, *Superlubricity*, pages 207–225. Elsevier Science B.V., 2007. doi: 10.1016/B978-044452772-1/50044-5.

[114] N. Metropolis, A. W. Rosenbluth, M. N. Rosenbluth, and A. H. Teller. Equation of state calculations by fast computing machines. *J. Chem. Phys.*, 21: 1087–1092, 1953. doi: 10.1063/1.1699114.

[115] S. Mignuzzi, A. J. Pollard, N. Bonini, B. Brennan, I. S. Gilmore, M. A. Pimenta, D. Richards, and D. Roy. Effects of disorder on Raman scattering of single-layer MoS_2. *Phys. Rev. B*, 91:195411, 2015. doi: 10.1103/PhysRevB.91.195411.

[116] K. Mohammadtabar, E. Guerrero, D. A. Strubbe, and A. Martini. Development and validation of ReaxFF reactive force field for Ni-doped MoS_2. *in preparation.*, 2022.

[117] M. Molina-Ruiz, H. C. Jacks, D. R. Queen, Q. Wang, R. S. Crandall, and F. Hellman. Two-level systems and growth-induced metastability in hydrogenated amorphous silicon. *Mater. Res. Express*, 7:095201, 2020. doi: 10.1088/2053-1591/abb498.

[118] A. Molina-Sánchez and L. Wirtz. Phonons in single-layer and few-layer MoS_2 and WS_2. *Phys. Rev. B*, 84:155413, 2011. doi: 10.1103/PhysRevB.84.155413.

[119] A. Molina-Sánchez, K. Hummer, and L. Wirtz. Vibrational and optical properties of MoS_2: From monolayer to bulk. *Surf. Sci. Rep.*, 70:554–586, 2015. doi: 10.1016/j.surfrep.2015.10.001.

[120] D. Mosconi, P. Till, L. Calvillo, T. Kosmala, D. Garoli, D. Debellis, A. Martucci, S. Agnoli, and G. Granozzi. Effect of Ni doping on the MoS_2 structure and its hydrogen evolution activity in acid and alkaline electrolytes. *Surfaces*, 2(4):531–545, 2019. doi: 10.3390/surfaces2040039.

[121] S. C. Moss and J. F. Graczyk. Evidence of voids within the as-deposited structure of glassy silicon. *Phys. Rev. Lett.*, 23:1167–1171, 1969. doi: 10.1103/PhysRevLett.23.1167.

[122] T. Mueller, E. Johlin, and J. C. Grossman. Origins of hole traps in hydrogenated nanocrystalline and amorphous silicon revealed through machine learning. *Phys. Rev. B*, 89:115202, 2014. doi: 10.1103/PhysRevB.89.115202.

[123] S. Mundotiya, S. Rupesh, S. Saha, R. Kakkar, S. Pal, D. Kunzru, R. G. S. Pala, and S. Sivakumar. Effect of sodium on Ni-promoted MoS_2 catalyst for hydrodesulfurization reaction: Combined experimental and simulation study. *Energy Fuels*, 35:2368–2378, 2021. doi: 10.1021/acs.energyfuels.0c02879.

[124] S. M. Nakhmanson and D. A. Drabold. Low-temperature anomalous specific heat without tunneling modes: A simulation for $a-\mathrm{Si}$ with voids. *Phys. Rev. B*, 61:5376–5380, 2000. doi: 10.1103/PhysRevB.61.5376.

[125] A. Nathan, A. Kumar, K. Sakariya, P. Servati, S. Sambandan, and D. Striakhilev. Amorphous silicon thin film transistor circuit integration for organic led displays on glass and plastic. *IEEE J. Solid-State Circuits*, 39:1477–1486, 2004. doi: 10.1109/JSSC.2004.829373.

[126] S. P. Ong, L. Wang, B. Kang, and G. Ceder. Li—Fe—P—O_2 phase diagram from first principles calculations. *Chem. Mater.*, 20:1798–1807, 2008. doi: 10.1021/cm702327g.

[127] A. Ostadhossein, A. Rahnamoun, Y. Wang, P. Zhao, S. Zhang, V. H. Crespi, and A. C. T. van Duin. ReaxFF reactive force-field study of molybdenum disulfide (MoS_2). *J. Phys. Chem. Lett.*, 8:631–640, 2017. doi: 10.1021/acs.jpclett.6b02902.

[128] J. D. Ouwens and R. E. I. Schropp. Hydrogen microstructure in hydrogenated amorphous silicon. *Phys. Rev. B*, 54:17759–17762, 1996. doi: 10.1103/PhysRevB.54.17759.

[129] Z. Pang, J. Wan, A. Lu, J. Dai, L. Hu, and T. Li. Giant tunability of interlayer friction in graphite via ion intercalation. *Extreme Mech. Lett.*, 35: 100616, 2020. doi: 10.1016/j.eml.2019.100616.

[130] M. Park, I.-H. Lee, and Y.-S. Kim. Lattice thermal conductivity of crystalline and amorphous silicon with and without isotopic effects from the ballistic to diffusive thermal transport regime. *J. Appl. Phys.*, 116(4):043514, 2014. doi: 10.1063/1.4891500.

[131] S. Park, J. Park, H. Abroshan, L. Zhang, J. K. Kim, J. Zhang, J. Guo, S. Siahrostami, and X. Zheng. Enhancing catalytic activity of MoS_2 basal plane S-vacancy by Co cluster addition. *ACS Energy Lett.*, 3:2685–2693, 2018. doi: 10.1021/acsenergylett.8b01567.

[132] D. Paudel, R. Atta-Fynn, D. A. Drabold, S. R. Elliott, and P. Biswas. Small-angle x-ray scattering in amorphous silicon: A computational study. *Phys. Rev. B*, 97:184202, 2018. doi: 10.1103/PhysRevB.97.184202.

[133] M. C. Payne, M. P. Teter, D. C. Allan, T. A. Arias, and J. D. Joannopoulos. Iterative minimization techniques for ab initio total-energy calculations: molecular dynamics and conjugate gradients. *Rev. Mod. Phys.*, 64:1045–1097, 1992. doi: 10.1103/RevModPhys.64.1045.

[134] T. Peña, S. A. Chowdhury, A. Azizimanesh, A. Sewaket, H. Askari, and S. M. Wu. Strain engineering 2D MoS_2 with thin film stress capping layers. *2D Mater.*, 8:045001, 2021. doi: 10.1088/2053-1583/ac08f2.

[135] A. Pedersen, L. Pizzagalli, and H. Jónsson. Optimal atomic structure of amorphous silicon obtained from density functional theory calculations. *New J. Phys.*, 19:063018, 2017. doi: 10.1088/1367-2630/aa732e.

[136] H. Peelaers and C. G. Van de Walle. Elastic constants and pressure-induced effects in MoS_2. *J. Phys. Chem. C*, 118:12073–12076, 2014. doi: 10.1021/jp503683h.

[137] H. Peelaers and C. G. Van de Walle. First-principles study of van der Waals interactions in MoS_2 and MoO_3. *J. Phys. Condens. Matter*, 26:305502, 2014. doi: 10.1088/0953-8984/26/30/305502.

[138] J. P. Perdew and Y. Wang. Accurate and simple analytic representation of the electron-gas correlation energy. *Phys. Rev. B*, 45:13244, 1992. doi: 10.1103/PhysRevB.45.13244.

[139] J. P. Perdew, K. Burke, and M. Ernzerhof. Generalized Gradient Approximation made simple. *Phys. Rev. Lett.*, 77:3865–3868, 1996. doi: 10.1103/PhysRevLett.77.3865.

[140] M. Pinheiro, R. L. Martin, C. H. Rycroft, A. Jones, E. Iglesia, and M. Haranczyk. Characterization and comparison of pore landscapes in crystalline porous materials. *Journal of Molecular Graphics and Modelling*, 44:208–219, 2013. doi: 10.1016/j.jmgm.2013.05.007.

[141] D. R Queen, X. Liu, J. Karel, T. Metcalf, and F. Hellman. Excess specific heat in evaporated amorphous silicon. *Phys. Rev. Lett.*, 110:135901, 03 2013. doi: 10.1103/PhysRevLett.110.135901.

[142] R. Raghunathan, E. Johlin, and J. C. Grossman. Grain boundary engineering for improved thin silicon photovoltaics. *Nano Lett.*, 14:4943–4950, 2014. doi: 10.1021/nl501020q.

[143] S. Rangarajan and M. Mavrikakis. Adsorption of nitrogen- and sulfur-containing compounds for NiMoS for hydrotreating reactions: A DFT and vdW-corrected study. *AIChE J*, 61:4036–4050, 2015. doi: 10.1002/aic.15025.

[144] L. Rapoport, A. Moshkovich, V. Perfilyev, A. Laikhtman, I. Lapsker, L. Yadgarov, R. Rosentsveig, and R. Tenne. High lubricity of Re-doped fullerene-like MoS_2 nanoparticles. *Tribol. Lett.*, 45:257–264, 2012. doi: 10.1007/s11249-011-9881-8.

[145] F. A. Rasmussen and K. S. Thygesen. Computational 2D materials database:

Electronic structure of transition-metal dichalcogenides and oxides. *J. Phys. Chem. C*, 119:13169–13183, 2015. doi: 10.1021/acs.jpcc.5b02950.

[146] M. Reguzzoni, A. Fasolino, E. Molinari, and M. C. Righi. Friction by shear deformations in multilayer graphene. *J. Phys. Chem. C*, 116:39:21104–21108, 2012. doi: 10.1021/jp306929g.

[147] Z. Remeš, M. Vaněček, A. H. Mahan, and R. S. Crandall. Silicon network relaxation in amorphous hydrogenated silicon. *Phys. Rev. B*, 56:R12710–R12713, 1997. doi: 10.1103/PhysRevB.56.R12710.

[148] P. Robustelli, S. Piana, and D. E. Shaw. Developing a molecular dynamics force field for both folded and disordered protein states. *Proc. Natl. Acad. Sci.*, 115(21):E4758–E4766, 2018. doi: 10.1073/pnas.1800690115.

[149] S. Roorda, W. C. Sinke, J. M. Poate, D. C. Jacobson, S. Dierker, B. S. Dennis, D. J. Eaglesham, F. Spaepen, and P. Fuoss. Structural relaxation and defect annihilation in pure amorphous silicon. *Phys. Rev. B*, 44:3702–3725, 1991. doi: 10.1103/PhysRevB.44.3702.

[150] P. Roura, J. Farjas, and P. Roca i Cabarrocas. Quantification of the bond-angle dispersion by Raman spectroscopy and the strain energy of amorphous silicon. *J. Appl. Phys.*, 104(7):073521, 2008. doi: 10.1063/1.2990767.

[151] R. Sanikop and C. Sudakar. Tailoring magnetically active defect sites in MoS_2 nanosheets for spintronics applications. *ACS Appl. Nano Mater.*, 3: 576–587, 2020. doi: 10.1021/acsanm.9b02121.

[152] J. R. Schaibley, H. Yu, G. Clark, P. Rivera, J. S. Ross, K. L. Seyler, W. Yao, and X. Xu. Valleytronics in 2D materials. *Nat. Rev. Mater.*, 1:16055, 2016. doi: 10.1038/natrevmats.2016.55.

[153] M. Schlipf and F. Gygi. Optimization algorithm for the generation of ONCV pseudopotentials. *Comput. Phys. Commun.*, 196:36–44, 2015. doi: 10.1016/j.cpc.2015.05.011.

[154] W. Schülke. Structural investigation of hydrogenated amorphous silicon by x-ray diffraction. *Philos. mag., B*, 43(3):451–468, 1981. doi: 10.1080/01418638108222109.

[155] T. Sekine, J. C., I. Samaras, M. Jouanne, and M. Balkanski. Vibrational modifications on lithium intercalation in MoS_2. *Mat. Sci. Eng. B*, 3:153–158, 1989. doi: 10.1016/0921-5107(89)90195-5.

[156] T. P. Senftle, S. Hong, M. M. Islam, S. B. Kylasa, Y. Zheng, Y. K. Shin, C. Junkermeier, R. Engel-Herbert, M. J. Janki, H. M. Aktulga, T. Verstraelen, A. Grama, and A. C. van Duin. The ReaxFF reactive force-field: Development, applications and future directions. *Npj Comput. Mater.*, 2: 15011, 2016. doi: 10.1038/npjcompumats.2015.11.

[157] W.-L. Shao, J. Shinar, B. C. Gerstein, F. Li, and J. S. Lannin. Magic-angle spinning ^{29}Si NMR study of short-range order in *a*-Si. *Phys. Rev. B*, 41: 9491–9494, 1990. doi: 10.1103/PhysRevB.41.9491.

[158] N. Sheremetyeva, D. Niedzielski, D. Tristant, L. Liang, L. E. Kerstetter, S. E. Mohney, and V. Meunier. Low-frequency Raman signature of Ag-intercalated few-layer MoS_2. *2D Mater.*, 8:025031, 2021. doi: 10.1088/2053-1583/abdbcc.

[159] Y. Shi, J.-K. Huang, L. Jin, Y.-T. Hsu, S. F. Yu, L.-J. Li, and H. Y. Yang. Selective decoration of Au nanoparticles on monolayer MoS_2 single crystals. *Sci. Rep.*, 3:1839, 2013. doi: 10.1038/srep01839.

[160] Y. Shi, Z. Cai, J. Pu, L. Wang, and Q. Xue. Interfacial molecular deformation mechanism for low friction of MoS_2 determined using ReaxFF-MD simulation. *Ceram. Int.*, 45(2):2258–2265, 2019.

[161] A. H. M. Smets, W. M. M. Kessels, and M. C. M. van de Sanden. Vacancies and voids in hydrogenated amorphous silicon. *Appl. Phys. Lett.*, 82:1547–1549, 2003. doi: 10.1063/1.1559657.

[162] I. Song, C. Park, and H. C. Choi. Synthesis and properties of molybdenum

disulphide: from bulk to atomic layers. *RSC Adv.*, 5:7495–7514, 2015. doi: 10.1039/c4ra11852a.

[163] D. L. Staebler and C. R. Wronski. Reversible conductivity changes in discharge-produced amorphous Si. *Appl. Phys. Lett.*, 31:292–294, 1977. doi: 10.1063/1.89674.

[164] J. Steinlechner, I. W. Martin, A. S. Bell, J. Hough, M. Fletcher, P. G. Murray, R. Robie, S. Rowan, and R. Schnabel. Silicon-based optical mirror coatings for ultrahigh precision metrology and sensing. *Phys. Rev. Lett.*, 120:263602, 2018. doi: 10.1103/PhysRevLett.120.263602.

[165] F. H. Stillinger and T. A. Weber. Packing structures and transitions in liquids and solids. *Science*, 225 (4666):983–989, 1984. doi: 10.1126/science.225.4666.983.

[166] F. H. Stillinger and T. A. Weber. Computer simulation of local order in condensed phases of silicon. *Phys. Rev. B*, 31:5262–5271, 1985. doi: 10.1103/PhysRevB.31.5262.

[167] R. A. Street. *Hydrogenated Amorphous Silicon.* Cambridge Solid State Science Series. Cambridge University Press, 1991. doi: 10.1017/CBO9780511525247.

[168] D. A. Strubbe, E. C. Johlin, T. R. Kirkpatrick, T. Buonassisi, and J. C. Grossman. Stress effects on the raman spectrum of an amorphous material: Theory and experiment on *a*-Si:H. *Phys. Rev. B*, 92:241202(R), 2015. doi: 10.1103/PhysRevB.92.241202.

[169] D. A. Strubbe, L. K. Wagner, E. C. Johlin, E. Guerrero, and J. C. Grossman. Computational Hydrogenated Amorphous Semiconductor Structure Maker (CHASSM), 2022. in preparation.

[170] B. C. Stupp. Synergistic effects of metals co-sputtered with MoS_2. *Thin Solid Films*, 84(3):257–266, 1981. doi: 10.1016/0040-6090(81)90023-7.

[171] J. Suh, T.-E. Park, D.-Y. Lin, D. Fu, J. Park, H. J. Jung, Y. Chen, C. Ko, C. Jang, Y. Sun, and et al. Doping against the native propensity of MoS_2: Degenerate hole doping by cation substitution. *Nano Lett.*, 14(12):6976–6982, 2014. doi: 10.1021/nl503251h.

[172] M. Sun, A. E. Nelson, and J. Adjaye. On the incorporation of nickel and cobalt into MoS_2-edge structures. *J. Catal.*, 226:32–40, 2004. doi: 10.1016/j.jcat.2004.05.005.

[173] H. T. T. Ta, A. K. Tieu, H. Zhu, H. Yu, and N. V. Tran. A first-principles study of impurity-enhanced adhesion and lubricity of graphene on iron oxide surface. *J. Phys. Chem. C*, 125:4310–4321, 2021. doi: 10.1021/acs.jpcc.1c00046.

[174] K. Tanaka. Elastic properties of covalent glasses. *Solid State Commun.*, 60 (3):295–297, 1986. doi: 10.1016/0038-1098(86)90469-2.

[175] P. Tangney, M. L. Cohen, and S. G. Louie. Giant wave-drag enhancement of friction in sliding carbon nanotubes. *Phys. Rev. Lett.*, 97:195901, 2006. doi: 10.1103/PhysRevLett.97.195901.

[176] A. A. Tedstone, D. J. Lewis, and P. O'Brien. Synthesis, properties, and applications of transition metal-doped layered transition metal dichalcogenides. *Chem. Mater.*, 28:1965–1974, 2016. doi: 10.1021/acs.chemmater.6b00430.

[177] J. Tersoff. New empirical approach for the structure and energy of covalent systems. *Phys. Rev. B*, 37:6991–7000, 1988. doi: doi.org/10.1103/PhysRevB.37.6991.

[178] A. P. Thompson, S. J. Plimpton, and W. Mattson. General formulation of pressure and stress tensor for arbitrary many-body interaction potentials under periodic boundary conditions. *J. Chem. Phys.*, 131(15):154107, 2009. doi: 10.1063/1.3245303.

[179] X. Tian, D. S. Kim, S. Yang, C. J. Ciccarino, Y. Gong, Y. Yang, Y. Yang, B. Duschatko, Y. Yuan, P. M. Ajayan, J. C. Idrobo, P. Narang, and J. Miao.

Correlating the three-dimensional atomic defects and electronic properties of two-dimensional transition metal dichalcogenides. *Nat. Mater.*, 19:867–873, 2020. doi: 10.1038/s41563-020-0636-5.

[180] K. K. Tiong, T. S. Shou, and C. H. Ho. Temperature dependence piezoreflectance study of the effect of doping MoS_2 with rhenium. *J. Phys. Condens. Matter*, 12:3441–3449, 2000. doi: 10.1088/0953-8984/12/14/319.

[181] A. Tkatchenko and M. Scheffler. Accurate molecular van der Waals interactions from ground-state electron density and free-atom reference data. *Phys. Rev. Lett.*, 102:073005, 2009. doi: 10.1103/PhysRevLett.102.073005.

[182] T. Todorova, V. Alexiev, R. Prins, and T. Weber. *Ab Initio* study of 2H-MoS_2 using hay and wadt effective core pseudo-potentials for modelling the $(10\bar{1}0)$ surface structure. *Phys. Chem. Chem. Phys.*, 6:3023–3030, 2004. doi: 10.1039/b402993n.

[183] M.-L. Tsai, S.-H. Su, J.-K. Chang, D.-S. Tsai, C. Chang-Hsiao, C.-I. Wu, L.-J. Li, L.-J. Chen, and J.-H. He. Monolayer MoS_2 heterojunction solar cells. *ACS Nano*, 8(8):8317–8322, 2014. doi: 10.1021/nn502776h.

[184] D. Turcotte and G. Schubert. *Geodynamics*. Cambridge University Press., 2002.

[185] H. Ustunel and D. Toffoli. Tribology at the atomistic scale with density functional theory. *Electron. Struct.*, 4:023002, 2022. doi: 10.1088/2516-1075/ac7188.

[186] A. C. T. van Duin, S. Dasgupta, F. Lorant, and W. A. Goddard III. ReaxFF: A reactive force field for hydrocarbons. *J. Phys. Chem. A*, 105:9396–9409, 2001. doi: 10.1021/jp004368u.

[187] M. J. van Setten, M. Giantomassi, E. Bousquet, M. J. Verstraete, D. R. Hamann, X. Gonze, and G.-M. Rignanese. The `PseudoDojo`: Training and grading a 85 element optimized norm-conserving pseudopotential table.

Comput. Phys. Commun., 226:39–54, 2018. doi: 10.1016/j.cpc.2018.01.012. http://www.pseudo-dojo.org/.

[188] V. Vandalon, M. A. Verheijen, W. M. M. Kessels, and A. A. Bol. Atomic layer deposition of Al-doped MoS_2: Synthesizing a p-type 2D semiconductor with tunable carrier density. *ACS Appl. Nano Mater.*, 3:10200–10208, 2020. doi: 10.1021/acsanm.0c02167.

[189] D. Vanderbilt. Soft self-consistent pseudopotentials in a generalized eigenvalue formalism. *Phys. Rev. B*, 41:7892–7895, 1990. doi: 10.1103/PhysRevB.41.7892.

[190] M. Vanecek, J. Holoubek, and A. Shah. Optical study of microvoids, voids, and local inhomogeneities in amorphous silicon. *Appl. Phys. Lett.*, 59(18): 2237–2239, 1991. doi: 10.1063/1.106081.

[191] M. R. Vazirisereshk, A. Martini, D. A. Strubbe, and M. Z. Baykara. Solid lubrication with MoS_2: A review. *Lubricants*, 7:57, 2019. doi: doi.org/10.3390/lubricants7070057.

[192] A. Vellore, S. R. Garcia, N. Walters, D. A. Johnson, A. Kennett, M. Heverly, and A. Martini. Ni-doped MoS_2 dry lubricant life. *Adv. Mater. Interfaces*, 7:2001109, 2020. doi: 10.1002/admi.202001109.

[193] S. von Alfthan, A. Kuronen, and K. Kaski. Realistic models of amorphous silica: A comparative study of different potentials. *Phys. Rev. B*, 68:073203, 2003. doi: 10.1103/PhysRevB.68.073203.

[194] L. K. Wagner and J. C. Grossman. Microscopic description of light induced defects in amorphous silicon solar cells. *Phys. Rev. Lett.*, 101:265501, 2008. doi: 10.1103/PhysRevLett.101.265501.

[195] A. Wambeke, L. Jalowiecki, S. Kasztelan, G. J., and J. P. Bonnelle. The active site for isoprene hydrogenation on $MoS_2/\gamma\text{-}Al_2O_3$ catalysts. *J. Catal.*, 109:320–328, 1988. doi: 10.1016/0021-9517(88)90215-1.

[196] D. Wang, X. Zhang, Y. Shen, and Z. Wu. Ni-doped MoS_2 nanoparticles as highly active hydrogen evolution electrocatalysts. *RSC Adv.*, 6:16656–16661, 2016. doi: 10.1039/c6ra02610a.

[197] J. Wang and A. M. Dongare. Density functional theory study of electronic structure of defects and the role on the strain relaxation behavior of MoS_2 bilayer structures. *J. Mater. Sci.*, 53:9064–9075, 2018. doi: 10.1007/s10853-018-2220-9.

[198] L. Wang, X. Zhou, T. Ma, D. Liu, L. Gao, X. Li, J. Zhang, Y. Hu, H. Wang, Y. Dai, and J. Luo. Superlubricity of a graphene/MoS_2 heterostructure: a combined experimental and DFT study. *Nanoscale*, 9:10846, 2017. doi: 10.1039/c7nr01451a.

[199] P. Wang, W. Gao, J. Wilkerson, K. M. Liechti, and R. Huang. Cavitation of water by volume-controlled stretching. *Extreme Mech. Lett.*, 11:59–67, 2017. doi: 10.1016/j.eml.2016.12.004.

[200] Y. Wang, B. R. Carvalho, and V. H. Crespi. Strong exciton regulation of Raman scattering in monolayer MoS_2. *Phys. Rev. B*, 98:161405(R), 2018. doi: 10.1103/PhysRevB.98.161405.

[201] T. F. Willems, C. H. Rycroft, M. Kazi, J. C. Meza, and M. Haranczyk. Algorithms and tools for high-throughput geometry-based analysis of crystalline porous materials. *Microporous and Mesoporous Mater.*, 149(1):134–141, 2012. doi: 10.1016/j.micromeso.2011.08.020.

[202] D. L. Williamson, S. Roorda, M. Chicoine, R. Tabti, P. A. Stolk, S. Acco, and F. W. Saris. On the nanostructure of pure amorphous silicon. *Appl. Phys. Lett.*, 67(2):226–228, 1995. doi: 10.1063/1.114675.

[203] J. A. Wilson and A. D. Yoffe. The transition metal dichalcogenides: Discussion and interpretation of the observed optical, electrical and structural properties. *Adv. Phys.*, 18(73):193–335, 1969. doi: 10.1080/00018736900101307.

[204] L. Wirtz, M. Lazzeri, F. Mauri, and A. Rubio. Raman spectra of BN nanotubes: *Ab initio* and bond-polarizability model calculations. *Phys. Rev. B*, 71:241402, 2005. doi: 10.1103/PhysRevB.71.241402.

[205] A. Witvrouw and F. Spaepen. Viscosity and elastic constants of amorphous Si and Ge. *J. Appl. Phys.*, 74(12):7154–7161, 1993. doi: 10.1063/1.355031.

[206] Wolfram Research Inc. *Mathematica version 12.1*, 2020. URL `http://www.wolfram.com`. Champaign, Illinois. 2020.

[207] F. Wooten, K. Winer, and D. Weaire. Computer generation of structural models of amorphous Si and Ge. *Phys. Rev. Lett.*, 54:1392–1395, 1985. doi: 10.1103/PhysRevLett.54.1392.

[208] A. C. Wright, A. C. Hannon, R. N. Sinclair, T. M. Brunier, C. A. Guy, R. J. Stewart, M. B. Strobel, and F. Jansen. Neutron scattering studies of hydrogenated, deuterated and fluorinated amorphous silicon. *J. Phys. Condens. Matter*, 19(41):415109, 2007. doi: 10.1088/0953-8984/19/41/415109.

[209] M. Wu and J. Li. Sliding ferroelectricity in 2D van der Waals materials: Related physics and future opportunities. *Proc. Natl. Acad. Sci.*, 118(50): e2115703118, 2021. doi: 10.1073/pnas.2115703118.

[210] B. Xia, P. Liu, Y. Liu, D. Gao, X. Desheng, and J. Ding. Re doping induced 2H-1T phase transformation and ferromagnetism in $\mathrm{MoS_2}$ nanosheets. *Appl. Phys. Lett.*, 113:013101, 2018. doi: 10.1063/1.5027535.

[211] L. Yadgarov, R. Rosentsveig, G. Leitus, A. Albu-Yaron, A. Moshkovich, V. Perfilyev, R. Vasic, A. I. Frenkel, A. N. Enyashin, G. Seifert, L. Rapoport, and R. Tenne. Controlled doping of $\mathrm{MS_2}$ (M=W, Mo) nanotubes and fullerene-like nanoparticles. *Angew. Chem. Int. Ed.*, 51:1148–1151, 2012. doi: 10.1002/anie.201105324.

[212] Z. Yang, S. Bhowmick, F. G. Sen, and A. T. Alpas. Microscopic and atomistic mechanisms of sliding friction of $\mathrm{MoS_2}$: Effects of undissociated and

dissociated H_2O. *Appl. Surf. Sci.*, 563:150270, 2021. doi: 10.1016/j.apsusc.2021.150270.

[213] Z. Yang, S. Bhowmick, F. G. Sen, and A. T. Alpas. Microscopic and atomistic mechanisms of sliding friction of MoS_2: Effects of undissociated and dissociated H_2O. *Appl. Surf. Sci.*, 563:150270, 2021. doi: 10.1016/j.apsusc.2021.150270.

[214] Z. Ye, A. Otero-de-la-Rosa, E. R. Johnson, and A. Martini. Oscillatory motion in layered materials: Graphene, boron nitride, and molybdenum disulfide. *Nanotech.*, 26:165701, 2015. doi: 10.1088/0957-4484/26/16/165701.

[215] S. I. Yengejeh, L. Junxian, S. A. Kazemi, W. Wen, and Y. Wang. Effect of structural phases on mechanical properties of molybdenum disulfide. *ACS Omega*, 5:5994–6002, 2020. doi: 10.1021/acsomega.9b04360.

[216] D. E. Yilmaz, R. Lotfi, C. Ashraf, S. Hong, and A. C. van Duin. Defect design of two-dimensional MoS_2 structures by using a graphene layer and potato stamp concept. *J. Phys. Chem. C*, 122(22):11911–11917, 2018. doi: 10.1021/acs.jpcc.8b02991.

[217] M. T. Yin and M. L. Cohen. Structural theory of graphite and graphitic silicon. *Phys. Rev. B*, 29:6996–6998, 1984. doi: 10.1103/PhysRevB.29.6996.

[218] A. Yoshimura, N. Koratkar, and V. Meunier. Substitutional transition metal doping in MoS_2: A first-principles study. *Nano Express*, 1(1):010008, 2020. doi: 10.1088/2632-959x/ab7cb3.

[219] Z. G. Yu, Y.-W. Zhang, and B. I. Yakobson. An anomalous formation pathway for dislocation-sulfur vacancy complexes in polycrystalline monolayer MoS_2. *Nano Lett.*, 15:6855–6861, 2015. doi: 10.1021/acs.nanolett.5b02769.

[220] H. Yuan, X. Zhou, Y. Cao, Q. Bian, Z. Zhang, H. Sun, S. Li, Z. Shao, J. Hu, Y. Zhu, and et al. Raman detection of hidden phonons assisted by atomic point defects in a two-dimensional semimetal. *npj 2D Mater. Appl.*, 3:12, 2019. doi: 10.1038/s41699-019-0093-7.

[221] N. A. Zarkevich and D. D. Johnson. Nudged-elastic band method with two climbing images: Finding transition states in complex energy landscapes. *J. Chem. Phys.*, 142:024106, 2015. doi: 10.1063/1.4905209.

[222] F. Zhang, Y. Lu, D. S. Schulman, T. Zhang, K. Fujisawa, Z. Lin, Y. Lei, A. L. Elias, S. Das, S. B. Sinnott, and et al. Carbon doping of WS_2 monolayers: Bandgap reduction and p-type doping transport. *Sci. Adv.*, 5:5, 2019. doi: 10.1126/sciadv.aav5003.

[223] J.-J. Zhang, B. Gao, and S. Dong. Strain-enhanced superconductivity of $\mathrm{Mo}X_2$ (X=S or Se) bilayers with Na intercalation. *Phys. Rev. B*, 93:155430, 2016. doi: 10.1103/PhysRevB.93.155430.

[224] R. Zhang, I.-L. Tsai, J. Chapman, E. Khestanova, J. Waters, and I. V. Grigorieva. Superconductivity in potassium-doped metallic polymorphs of MoS_2. *Nano Lett.*, 16:629–636, 2016. doi: 10.1021/acs.nanolett.5b04361.

[225] S. B. Zhang, S.-H. Wei, A. Zunger, and H. Katayama-Yoshida. Defect physics of the $CuInSe_2$ chalcopyrite semiconductor. *Phys. Rev. B*, 57:9642–9656, 1998. doi: 10.1103/PhysRevB.57.9642.

[226] P. Zhao, J. Zheng, P. Guo, Z. Jiang, L. Cao, and Y. Wan. Electronic and magnetic properties of Re-doped single-layer MoS_2: A DFT study. *Comput. Mater. Sci.*, 128:287–293, 2017. doi: 10.1016/j.commatsci.2016.11.030.

[227] X. Zhao, P. Song, C. Wang, A. C. Riis-Jensen, W. Fu, D. Wan, L. Kang, S. Ning, J. Dan, T. Venkatesan, and et al. Engineering covalently bonded 2D layered materials by self-intercalation. *Nature*, 581:171–177, 2020. doi: 10.1038/s41586-020-2241-9.

[228] X. Zheng, M. Liu, E. R. Johnson, J. Contreras-García, and W. Yang. Delocalization error of density-functional approximations: A distinct manifestation in hydrogen molecular chains. *J. Chem. Phys.*, 137:214106, 2012. doi: 10.1063/1.4768673.

[229] M. Zhong, C. Shen, L. Huang, H.-X. Deng, G. Shen, H. Zheng, Z. Wei, and J. Li. Electronic structure and exciton shifts in Sb-doped MoS_2 monolayer. *npj 2D Mater. Appl.*, 3:1, 2019. doi: 10.1038/s41699-018-0083-1.

[230] J. Zhu, H. Zhang, Y. Tong, L. Zhao, Y. Zhang, Y. Qiu, and X. Lin. First-principles investigations of metal (V, Nb, Ta)-doped monolayer MoS_2: Structural stability, electronic properties and adsorption of gas molecules. *Appl. Surf. Sci.*, 419:522–530, 2017. doi: 10.1016/j.apsusc.2017.04.157.

[231] G. T. Zimanyi, C. Hansen, and D. A. Strubbe. Performance degradation in aSi/cSi heterojunction solar cells by glassy dynamics. In *Proceedings of the 46th IEEE Photovoltaic Specialists Conference*, 2019.

[232] J. Zou, F. Li, M. A. Bissett, F. Kim, and L. J. Hardwick. Intercalation behaviour of Li and Na into 3-layer and multilayer MoS_2 flakes. *Electrochim. Acta*, 331:135284, 2020. doi: 10.1016/j.electacta.2019.135284.